PhD Thesis

Student Acknowledgement
I acknowledge that: • This PhD thesis is my own work and that no part of this submission has been copied from any other student's work or from any source except where due acknowledgement has been made. • I am aware that penalties exist for plagiarism and any unauthorised collusion with other students or external consultants.

Thesis Title	Analysis and Mitigation of the Adverse Effects of Voltage Sags and Swells on Wind Farms
Faculty	Faculty of Science, Engineering and Technology
University	Swinburne University of Technology, Hawthorn, Victoria, Australia

Student Name	Tapash Kumar Das	**ID Number**	4930991
Email	tdas@swin.edu.au	**Phone**	0425569248
Starting Date	01/09/2013		
Principal Supervisor	Dr. Jingxin Zhang	**Associate Supervisor**	Dr. Hemanshu Roy Pota
Date of Submission	27/09/2018		

Analysis and Mitigation of the Adverse Effects of Voltage Sags and Swells on Wind Farms

By

Tapash Kumar Das

A thesis submitted in fulfilment of the requirements for the degree of

Doctor of Philosophy

Faculty of Engineering & Industrial Sciences
Swinburne University of Technology
Hawthorn, Victoria, Australia

January, 2019

Abstract

Due to the depletion of natural resources and the adverse effects of climate change, renewable energy sources are receiving great attention from researchers and industry leaders more than ever before. Wind power has already established itself to be a reliable and sustainable energy source. However, the ever increasing penetration of wind power in the electricity grid has resulted in some protection and stability issues during grid voltage transient states. Grid codes around the world have been updated to reflect the changing nature of grid energy sources. It is now required that wind farms stay connected to the grid during voltage sags and swells, and simultaneously support grid voltage stability by regulating the flow of reactive power between the wind farm and the grid. This thesis focuses on the impact of symmetrical and asymmetrical grid voltage sags and swells on variable-speed wind generator systems. Grid faults result in voltage sags at the Point of Common Coupling (PCC), whereas a sudden loss of a huge amount load leads to voltage swells. The effect of voltage sags and swells on wind turbine generators like Type 3 Doubly-Fed Induction Generators (DFIG) and Type 4 Full-scale converter wind generators is qualitatively analysed. The main protection issue for DFIG wind systems during voltage transients are excessive currents flowing in the Rotor-Side Converter (RSC) and over-voltage in the dc-link capacitor of the partial-scale back-to-back converter, while it is the over-voltage and under-voltage of the dc-link capacitor in the full-scale converter of Type 4 wind systems. A comparative study is also performed to investigate the relative degree of risk posed by different grid voltage conditions to these two wind generator systems. It is found that asymmetrical voltage sags are more harmful to DFIGs, while symmetrical sags pose a greater danger to Type 4 wind generators. A detailed quantitative investigation is conducted to provide a theoretical framework to explain the issues arising from voltage sags and swells.

Novel ride-through strategies are designed for Type 3 and Type 4 wind generator-based wind farms to improve their grid compliance. The strategies include a protection scheme and a power management scheme. The purpose of the protection scheme is to limit the RSC overcurrent in Type 3 wind generators and keep the dc-link voltage within an acceptable range in Type 3 and Type 4 wind generators. This is done with the help of some hardware modification in the wind system using additional three-phase transformers, capacitors and Nickel-Metal Hydride battery. The power management scheme supports the grid voltage by controlling the flow of reactive power to and from the grid. During voltage sags, the required reactive current is calculated and injected into the grid from the power-electronic converter of

the wind generators. The converters absorb reactive current from the grid when a voltage swell occurs. This helps in maintaining the voltage magnitude at PCC at a reasonable level. A switching algorithm is implemented to regulate inclusion of the protection hardware during transients; it also activates the power management scheme. A neural network predictive controller (NNPC) is designed for speed regulation of the wind system by replacing the traditional PI controller. The NNPC shows superior performance in terms of dc-link voltage regulation and output disturbance rejection. Finally, it is observed that both the ride-through strategies enhance the performance of Type 3 DFIGs and Type 4 wind generators significantly during voltage transients at the PCC. MathWorks® Simscape Power Systems is used as a simulation platform in this thesis. This research makes the high grid penetration of wind power a more viable and dependable option.

Acknowledgement

I would like to thank my principal supervisor Dr. Jingxin Zhang and external supervisor Dr. Hemanshu Roy Pota for their guidance and emotional support to conduct this research. Both of them helped me out with their valuable advice and motivated me to work during stressful situations. This research would not have been possible without their help and encouragement. I owe them a lot for the quality and content of this research work and look forward to collaborate with them in any future research I undertake.

I would also like to thank my parents, Dr. Hirendra Kumar Das and Mrs. Rina Rani Das, and my wife, Mrs. Nilanjana Rumu, for their love and support during the highs and lows of this PhD experience. Lastly, I want to thank Swinburne University of Technology for providing me with the Australian Postgraduate Award (APA) to be able to support myself financially throughout my PhD tenure.

Declaration

I hereby declare that this PhD thesis is my own original work to the best of my knowledge; it contains no previously published material by other authors except where proper references have been made. This thesis has not been submitted to any other institution for a degree or diploma. I understand that Swinburne University may make this thesis available to others electronically.

[redacted]

Tapash Kumar Das

September, 2018

List of Publications

Refereed Journal Papers:

1. T. K. Das, J. Zhang and H. R. Pota, "A Novel Performance Enhancement Scheme for Doubly-Fed Induction Generator-Based Wind Power Systems under Voltage Sags and Swells," Published in International Journal of Emerging Electric Power, July 2017, online doi: https://doi.org/10.1515/ijeeps-2016-0270.
2. T. K. Das, J. Zhang and H. R. Pota, "A Novel Performance Augmentation Strategy for Type IV Wind Generator Systems Under Voltage Sags and Swells," submitted to International Journal of Power and Energy Conversion, 2017.
3. T. K. Das and J. Zhang, "A review on the ride-through strategies on type 3 DFIG wind turbine generators under voltage sags and swells," submitted to Journal of Modern Power Systems and Clean Energy, 2017.

Refereed Conference Papers:

1. T. Das, J. Zhang and H. R. Pota, " Enhancing Grid Compliance of DFIG Wind Turbine Generators to Voltage Sags and Swells," Australasian Universities Power Engineering Conference , The University of Queensland, St. Lucia Campus, Brisbane, Australia, 25-28 September 2016, Article No. 7749293.
2. T. Das, J. Zhang and H. R. Pota, "Comparative Study of the Response of Wind Turbine Generators to Voltage Sags and Swells," Australian Universities Power Engineering Conference, The University of Queensland, St. Lucia Campus, Brisbane, Australia, 25-28 September 2016, Article No. 7749281.
3. T. Das and J. Zhang, "Counteracting the Effects of Symmetrical and Asymmetrical Voltage Sags on DFIG-Based Wind Power Systems," International Conference on Advanced Mechatronic Systems , Swinburne University of Technology, Hawthorn Campus, Melbourne, Australia, Nov. 30- Dec. 3, 2016.
4. T. Das and J. Zhang, "Mitigating the Impact of Voltage Sags and Swells on Type IV Wind Generator Systems," Australian Universities Power Engineering Conference, Victoria University, Melbourne, Australia, 19-22 November 2017.

Table of Contents

List of Figures

List of Symbols

Symbols

$\boldsymbol{P_{wind}}$	power present in wind
$P_{extracted}$	power absorbed from wind
P_f	power transferred to the grid filter
P_r	rotor active power
P_s	stator active power
P_g	grid filter power
Q_s	stator reactive power
ρ	density of air
A	cross-sectional area of wind
v	velocity of wind
C_p	power coefficient
λ	tip-speed ratio
r	radius of the wind turbine
β	pitch angle/blade angle
p	number of poles
H_t	inertia of wind turbine
H_g	inertia of generator rotor
ω_t	mechanical torque
ω_r	rotor speed
ω_s	synchronous speed
T_e	electrical torque
T_t	mechanical torque
D_t	turbine damping coefficient

D_g	generator damping coefficient
D_m	mutual damping
K_s	stiffness coefficient
θ_t	turbine rotor angle
θ_r	generator rotor angle
V_{ds}	d-axis stator voltage
V_{qs}	q-axis stator voltage
V_{dr}	d-axis rotor voltage
V_{qr}	q-axis rotor voltage
V_{fd}	field excitation voltage
V_{kd}	d-axis damping voltage
V_{kq1}	q-axis damping voltage 1
V_{kq2}	q-axis damping voltage 2
V_g	grid voltage
V_c	dc-link voltage
$V_{\alpha s}$	α-axis stator voltage
$V_{\beta s}$	β-axis stator voltage
V_1	positive sequence voltage
V_2	negative sequence voltage
V_0	zero sequence voltage
R_s	stator resistance
R_r	rotor resistance
R_{fd}	field resistance
R_{kd}	d-axis damping resistance
R_{kq1}	q-axis damping resistance 1

R_{kq2}	q-axis damping resistance 2
R_f	filter resistance
$R_{crow,max}$	maximum resistance of crowbar circuit
R_{chop}	resistance of dc-chopper circuit
I_{ds}	d-axis stator current
I_{qs}	q-axis stator current
I_{dr}	d-axis rotor current
I_{qr}	q-axis rotor current
I_{fd}	field current
I_{kd}	d-axis damping current
I_{kq1}	q-axis damping current 1
I_{kq2}	q-axis damping current 2
$I_{\alpha s}$	α-axis stator current
$I_{\beta s}$	β-axis stator current
ψ_{ds}	d-axis stator magnetic flux
ψ_{qs}	q-axis stator magnetic flux
ψ_{dr}	d-axis rotor magnetic flux
ψ_{qr}	q-axis rotor magnetic flux
ψ_{fd}	field magnetic flux
ψ_{kd}	d-axis damping magnetic flux
ψ_{kq1}	q-axis damping magnetic flux 1
ψ_{kq2}	q-axis damping magnetic flux 2
ψ_{dc}	magnetic flux dc component
L_{ls}	stator leakage inductance
L_{lr}	rotor leakage inductance

L_m	mutual inductance
L_s	stator inductance
L_r	rotor inductance
L_f	filter inductance
C	dc-link capacitance
σ	leakage factor
τ	time constant
E_c	energy delivered to capacitor
y_r	desired model response
y_m	network model response
J	performance criterion

Chapter 1

Introduction

1.1. Background

Traditional sources of electricity generation using coal, natural gas etc. contributes significantly to climate change. These sources are also depleting as time goes on. As a result, there is a relook at how we generate electricity globally and more attention is being paid to renewable energy resources. Renewable resources like solar, wind, hydro etc. are environmentally friendly and they can serve humanity indefinitely. In Fig. 1, it is seen that the total amount of electricity generated from renewable sources globally has risen from 934 GW to 1,848 GW between 2005 and 2015. In 2015, renewable sources constituted 29.5% of total installed global electricity capacity and 24.2% of total generation. Wind and solar energy technologies are the fastest growing in the world as seen in Fig. 2. The top countries in 2015 for installed renewable electricity capacity are China, United States, Germany, Japan and India [1].

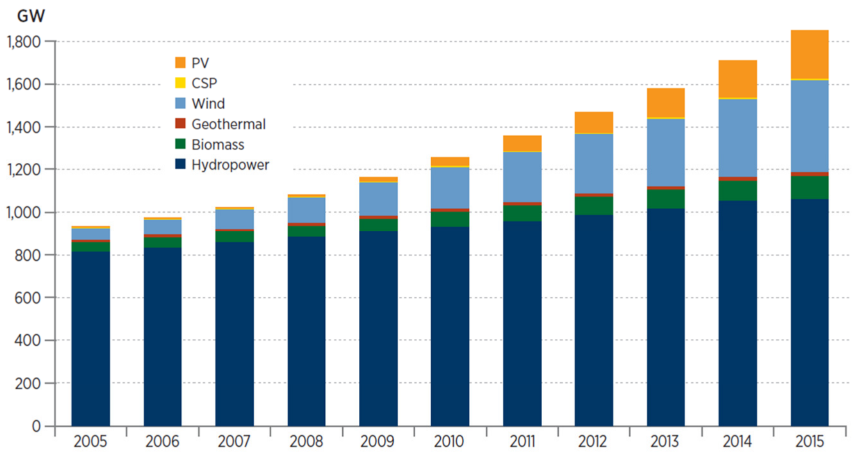

Figure 1: Global renewable electricity capacity [1]

Wind turbine generators are a big player in the global energy sector. Wind power has risen substantially during the last decade and it will go up even more going into the future. The worldwide capacity of wind power has reached 456 GW in the first half of 2016 and it is projected to cross 500 GW by the year end (see Fig. 3). India, Germany and Brazil are leading the market in terms of wind capacity growth; while five countries, India, USA, China, Germany and Spain represent 67% of worldwide wind capacity. By region, Asia has overtaken Europe in its global share of wind capacity. In 2000, Europe had 73% of global share, while Asia accounted for only 10%. In 2015, Asia's share was 42%, whereas Europe's share fell to 33% (see Fig. 4) [2].

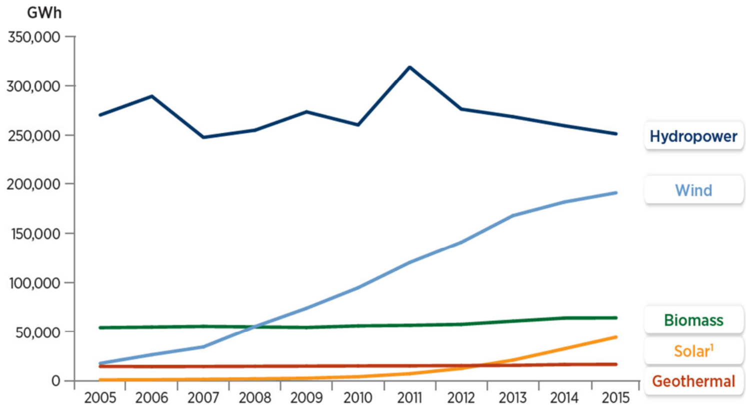

Figure 2: Global electricity generation by technology [1]

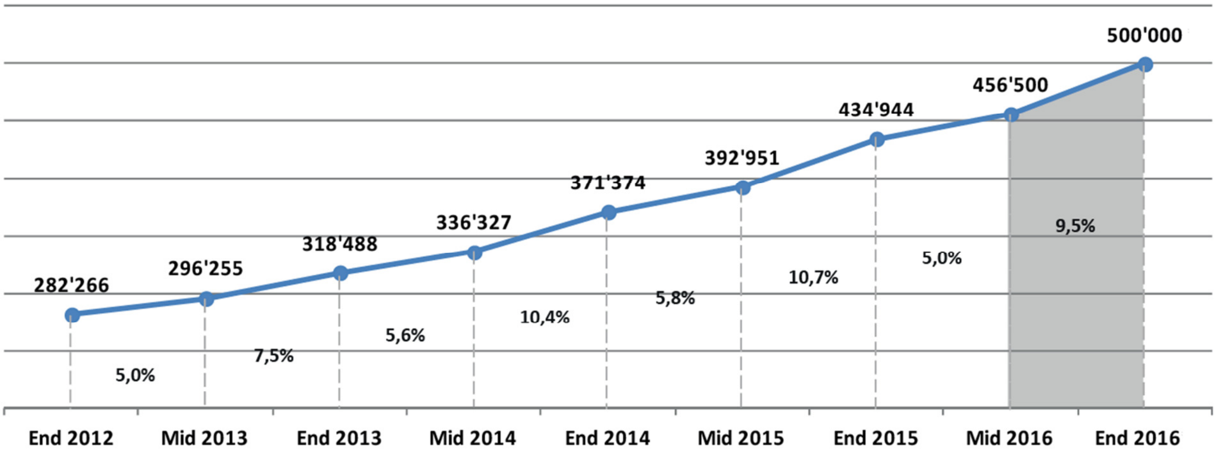

Figure 3: Total installed wind capacity worldwide [2]

Nonetheless, a large participation of wind energy in the grid has its technical challenges. Providing steady power can be a problem because of the intermittent nature of wind. This affects grid reliability. Studying wind data to predict wind patterns in a given geographical area is one way to solve the problem. It is found that physics-based forecasting models, real-time data of wind or computational learning algorithms provide more accurate predictions than forecasts based on climatology. Also, dispersion of wind power over a large geographical area can reduce unpredictability and bring down instances of near-zero or zero power output. Wind power has a negative impact on the operating cost of electric power systems. A constant balance has to be maintained between the total demand of electricity and the total power generation. Traditionally, this complicated task is being performed by operators using well-known power plant characteristics, control algorithms and operating experience. With wind in the picture, conventional power plants have to compensate for wind power variations to maintain a good balance between demand and supply. This causes the conventional power plants to diverge away from optimal operating costs thereby increasing the overall operating cost [3].

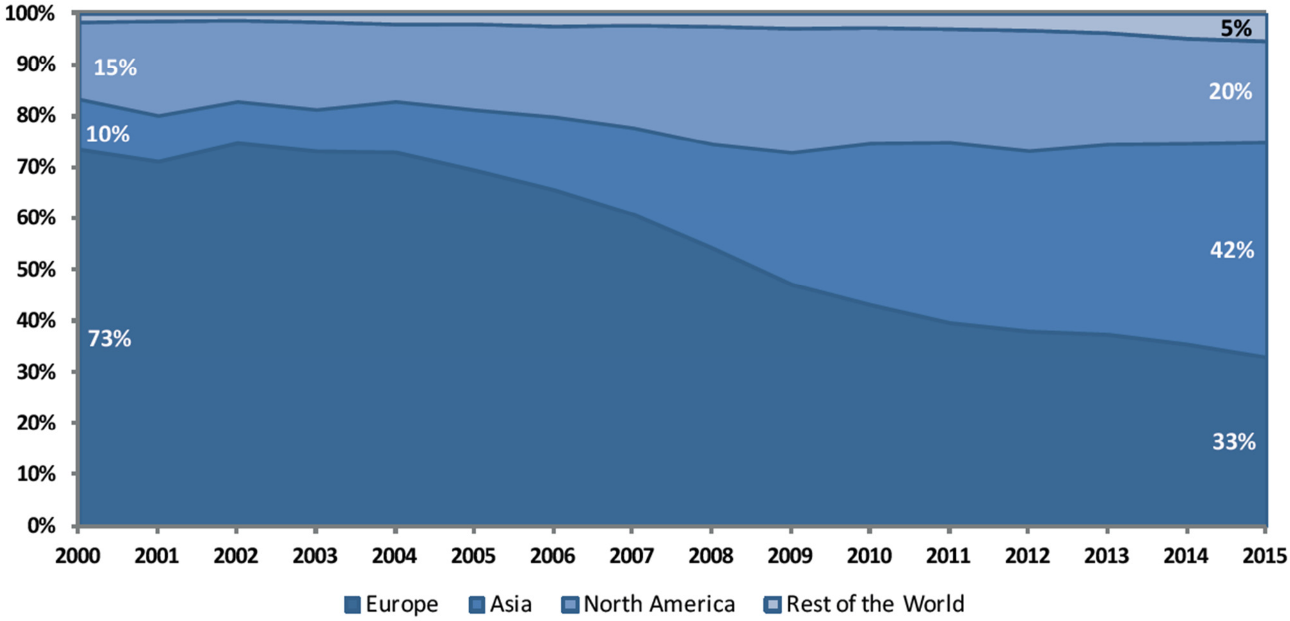

Figure 4: Global share of installed wind capacity [2]

Power quality is another major challenge of wind power integration. Wind variability can lead to voltage sags, frequency deviations and low power factor. The problem of low power factor is mainly with induction generators which tend to absorb reactive current from the grid. Wind power can also result in power flow imbalances in the grid. There may be too much wind power when the load demand is low; this will cause excessive power to flow on the utility's system. Likewise, there may not be sufficient wind power available when the load demand is high. The study of power system dynamics looks at how a power system reacts to an external disturbance that changes its optimal operating point. Such disturbances include frequency deviations, generator tripping, grid faults, power changes in the prime mover etc. The power system is considered stable if it reaches a new steady state after a disturbance, where all the generators and loads remain connected to the system. However, any disconnection of generators or loads in the new steady state would render the power system unstable. Traditionally, these dynamics are regulated by conventional generators. The introduction of wind generators can affect the transient stability and small-signal stability of a power system. Therefore, sufficient measures have to be taken to ensure the stability of the entire system. Transmission planners and operators have to install a strong transmission grid for wind power. Wind turbines are usually concentrated in areas where good wind resources are available. However, the local consumption of wind power may be low and, so, the surplus power needs to be transmitted to where the demand of power is high [3].

1.2. Motivations of the proposed research

The motivations of the proposed research are:

- Grid voltage disturbances lead to destruction of wind generators and they have to be dealt with by implementing a comprehensive ride-through strategy that can counter the adverse impact of all types of grid voltage fluctuations, namely, symmetrical and asymmetrical sags, and symmetrical and asymmetrical swells. Currently, there is a lack of a regulation strategy that takes into account all the different types of voltage fluctuations in their design and execution.
- There is also requirement for a smart reactive power management strategy that can support the grid according to the type of voltage disturbance. The proper regulation of reactive power will ensure that grid condition remains stable even during disturbances. Consequently, this will have a positive impact on grid reliability.
- There needs to be a comparative study of the harmful effects of the different types of voltage disturbances. This will give us an insight into the relative degree of danger that various types of voltage disturbances presents to the wind generator. Hence, a more advanced ride-through strategy can be developed based on the study.
- Conventional PI controllers are unable to provide accurate control of wind generator variables during grid disturbances. Intelligent control like neural-network control can provide more reliable control. This will increase efficiency of wind generator operation.

1.3. Problem statement of the proposed thesis

Inspired by the motivations mentioned above, the aim of this thesis is to provide novel solutions to enhance the ride-through of wind generators during grid voltage disturbances.

- It is vital to design a novel ride-through strategy to facilitate uninterrupted operation of wind generators during grid disturbance. The novel strategy should be able to comprehensively counter all types of voltage fluctuations to protect the wind generator.

- The novel ride-through strategy should also simultaneously regulate the flow of reactive power according to the grid voltage situation to maintain grid stability.
- Intelligent control needs to be incorporated into the novel ride-through strategy to provide more accurate regulation of the wind generator variables during disturbances.

1.4. Contributions of the thesis

The key contributions of this research are:

- An extensive study of the current trends in research regarding ride-through solutions for Type 3 and Type 4 wind generators is conducted. The solutions are classified into three types and described sufficiently to understand the methods used to improve wind generator performance.
- A study of the adverse effects of voltage sags and swells at PCC on grid-connected onshore wind generators is carried out to identify key performance issues. Symmetrical and asymmetrical voltage fluctuations are both taken into account for analysis. Wind generator transient performance is analysed thoroughly and technical issues are ascertained based on the study.
- A comparative investigation into the relative degree of risk posed by symmetrical and asymmetrical voltage sags and swells is performed for Type 3 and Type 4 wind generator systems. This study helps devise advanced protection mechanism for the wind systems for superior grid stability.
- A novel protection and reactive power management strategy is proposed to improve the ride-through capability of Type 3 wind generators during voltage sags and swells. This strategy leads to considerable performance improvement in Type 3 wind generators.
- A new protection and reactive power management scheme is developed to enhance the ride-through performance of Type 4 wind generators during voltage sags and swells. It is seen that there is significant enhancement of wind generator performance.

1.5. Thesis outline

- **Chapter 1** provides brief background of the research topic, main motivations of the research and its problem statements, and the key contributions of the thesis.
- **Chapter 2** provides discussion of the wind generator technology and modern grid code requirements, extensive literature review of ride-through strategies for Type 3 and Type 4 wind generator systems.
- **Chapter 3** describes the electrical and mechanical modelling of Type 3 and Type 4 wind generators, the aerodynamic model, the types of power-electronic converters utilised, and their control structures.
- **Chapter 4** presents an in-depth analysis of the impact of voltage fluctuations on wind generators. It also provides a comparative study of the response of Type 3 and Type 4 wind generators to voltage sags and swells. It includes simulation results and discusses the relative degree of risk posed by different grid voltage conditions to wind generators.
- **Chapter 5** presents a novel integrated ride-through strategy for Type 3 wind generators to improve their performance during voltage sags and swells. Simulation results are included and discussed.
- **Chapter 6** presents a novel integrated ride-through strategy for Type 4 wind generators to augment their operation during voltage sags and swells. Simulation results are provided and discussed.
- **Chapter 7** provides conclusion of the research work and possible future work to expand the current accomplishments in this thesis.

Chapter 2

Wind Generator Ride Through Strategies

2.1 Introduction

In order to understand the technical issues related to wind farm performance during grid voltage fluctuations, it is important to comprehend the grid code requirements in various countries with significant levels of wind power penetration. The grid code requirements give us the benchmark against which wind farm performance can be ascertained. Moreover, thorough analysis of existing literature relating to ride-through schemes of Type 3 and Type 4 wind generators is required to identify gaps in the existing solutions and propose more advanced solutions. This chapter provides an overview of the grid code requirements regarding wind farm performance during disturbance as stipulated by different countries. An extensive, in-depth literature review is conducted for Type 3 and Type 4 WGs to identify current research trends regarding ride-through performance.

2.2 Grid codes and wind generator types

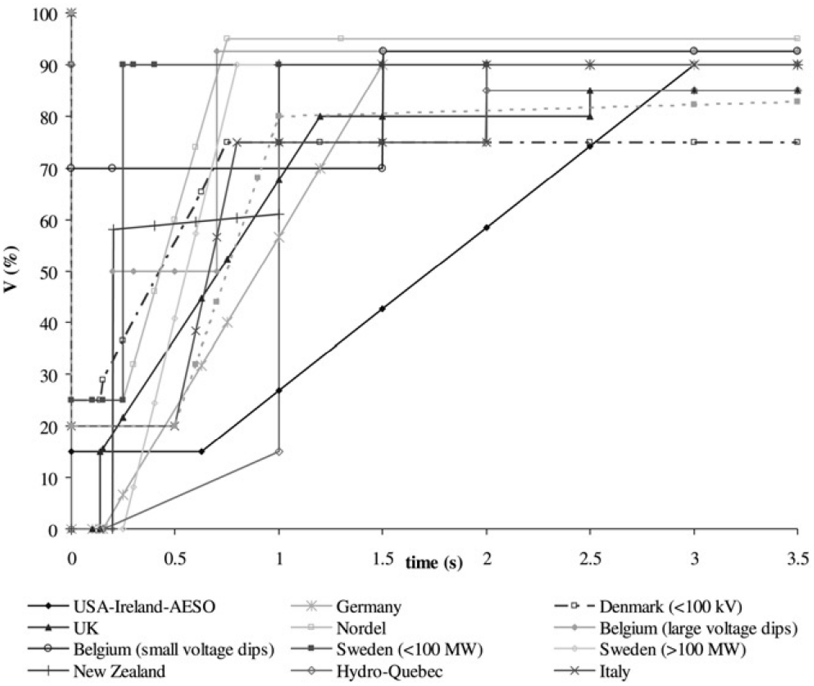

Figure 5: LVRT requirements of different grid codes [4]

Due to the large penetration of wind power, wind farms are required by different grid codes to stay connected to the grid even during grid disturbances and simultaneously maintain grid stability. This is because any disconnection of wind farms during grid disturbances would cause further weakening of grid stability. Many countries have prepared their own modern grid codes for wind farm performance regarding voltage sags and swells at the PCC. The capability of wind generators to tolerate low and high voltages at the PCC is known as Low-Voltage Ride Through (LVRT) and High-Voltage Ride Through (HVRT) respectively. Modern grid codes stipulate that wind farms should have sufficient LVRT and HVRT capabilities. This thesis focuses on the analysis of the impact of symmetrical and asymmetrical voltage sags and swells on wind generator systems and develops strategies to mitigate their adverse effects [4].

The German grid code from E.ON Netz is commonly used as a reference by other countries to develop their own grid codes. It is applicable to networks of 110, 220 and 380 kV voltage levels. The German grid code also includes additional requirements for offshore wind farms. 155 kV is the nominal voltage level stipulated for offshore grid connection. The British grid code is relevant for voltage levels of 132, 275 and 400 kV, while the Irish grid code deals with voltage levels of 110, 220 and 400 kV. There is an interconnected power system for four Nordic countries, namely, Denmark, Sweden, Norway and Finland. This is known as the Nordic grid and it follows the Nordic grid code issued by Nordel. However, Denmark is the only country which has separate technical prerequisites for grid-connected wind farms with voltages below and above 100 kV [4].

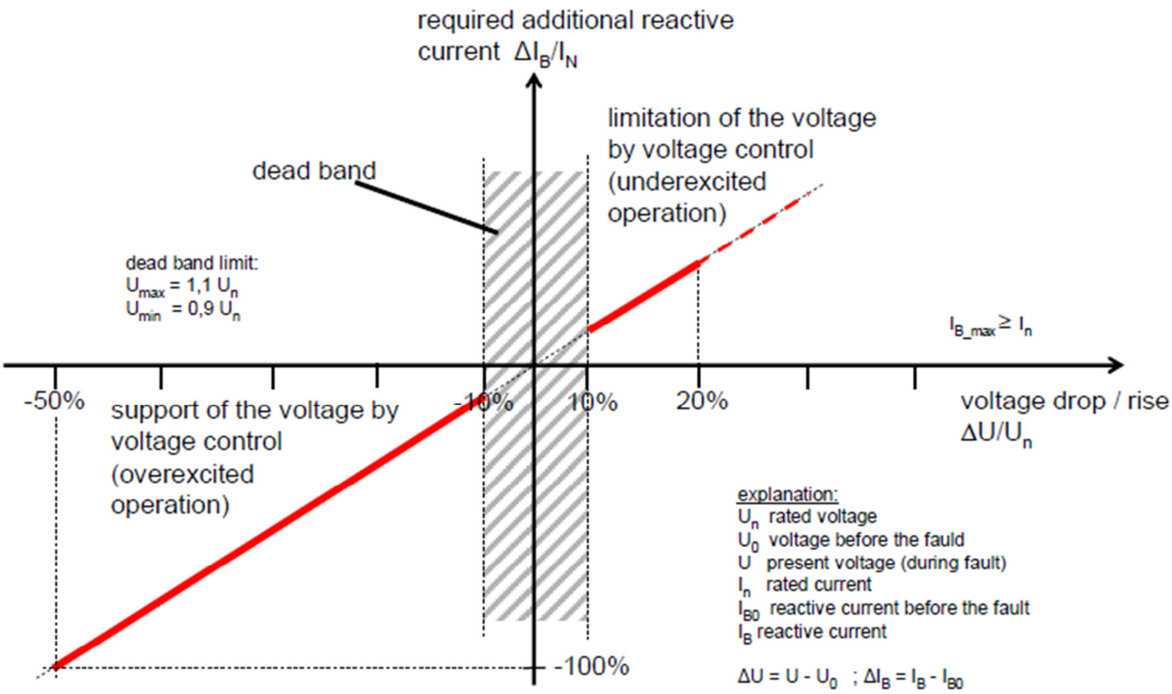

Figure 6: Reactive current requirements during voltage disturbance [5]

The Belgian grid code applies to networks at 30-70 kV and 150-380 kV. Canada has issued two grid codes- one issued by Hydro-Quebec and another by Alberta Electric System Operator (AESO). The former deals with 44 kV networks and higher, while the latter specifically applies to 5 MW or higher capacity wind farms connected to 69-240 kV networks. The USA has rules published by the Federal Energy Regulatory Commission (FERC) to take care of 20 MW or higher capacity wind farms. Some other countries which have grid codes regarding wind farms integration are Spain, Italy and New Zealand and Australia. In Australia, regulations for wind farms in Victoria and South Australia are set by the Australian Energy Market Operator (AEMO), while those for the Western Australian Network are issued by Western Power (WP). It is important to note that the list of countries is not exhaustive as grid code development is an ongoing process. In Fig. 5, the various grid codes regarding LVRT of different countries are shown on the graph for comparison, whereas Fig. 6 and Fig. 7 show the reactive current and HVRT requirements respectively [4], [6], [7].

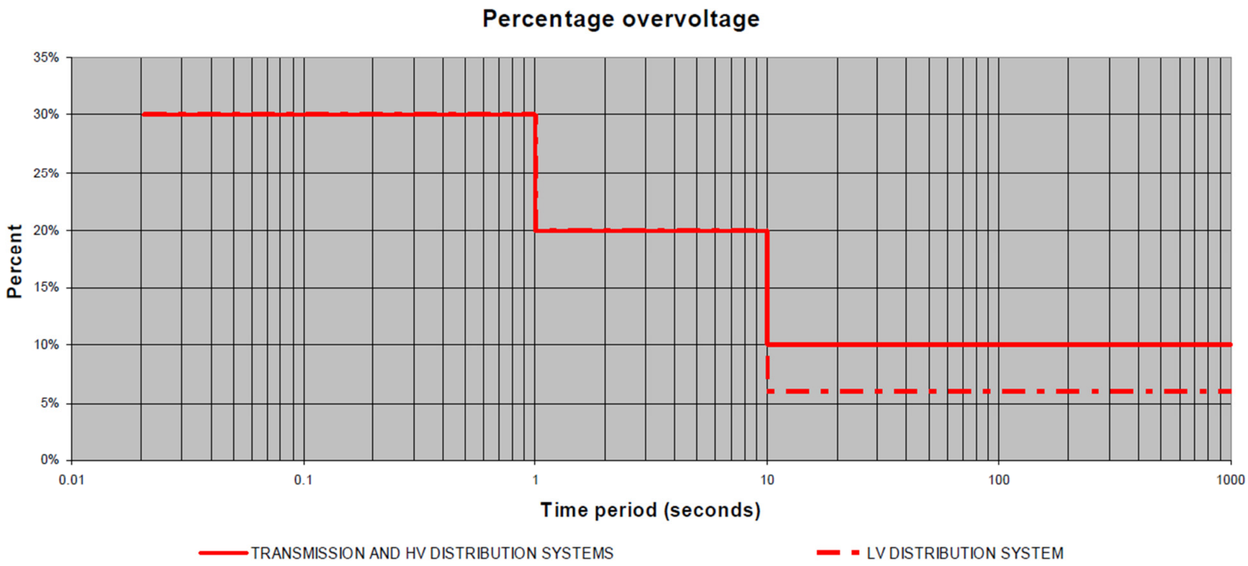

Figure 7: HVRT requirements by Western Power [7]

At present, there are four types of wind generator systems [8].

- Type 1: SCIG - Squirrel Cage Induction Generator *(Fixed Speed)*
- Type 2: WRIG - Wound Rotor Induction Generator *(Limited Variable Speed)*
- Type 3: DFIG - Doubly-Fed Induction Generator *(Variable Speed, Partial-scale converter)*

- Type 4: WRSG - Wound Rotor Synchronous Generator/ WRIG - Wound Rotor Induction Generator/ PMSG - Permanent Magnet Synchronous Generator *(Variable Speed, Full-scale converter)*

Type 1 wind systems are designed using a squirrel cage induction generator to operate efficiently at a fixed speed irrespective of wind speed variations. Its constant speed depends on the grid frequency, the gear ratio and design of the generator. A capacitor bank needs to be used for reactive power compensation, whereas a soft-starter ensures smooth grid connection by reducing inrush current. The main advantages of a fixed-speed wind generator are its low cost and robust operation. However, power quality, mechanical stress and unregulated reactive power absorption are its main challenges. Wind speed variations are transferred to the mechanical torque of the generator which, in turn, leads to electric power fluctuations. Type 2 wind system employs a wound rotor induction generator where the rotor resistance is variable. This technology is known as OptiSlip® and it offers limited speed variation. The usual range is 0-10% above the synchronous speed. Nevertheless, such wind generators are not suitable for maximum energy extraction from wind. Therefore, they are gradually becoming less dominant in the industry [8].

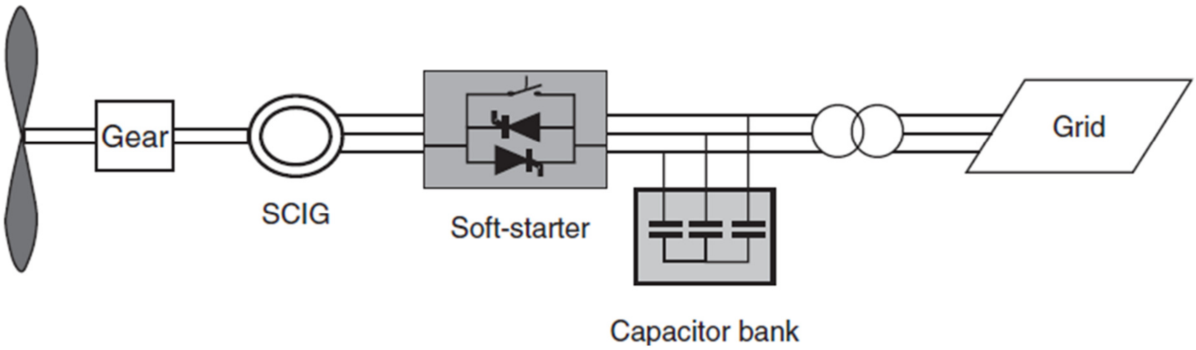

Figure 8: Type 1 wind system [8]

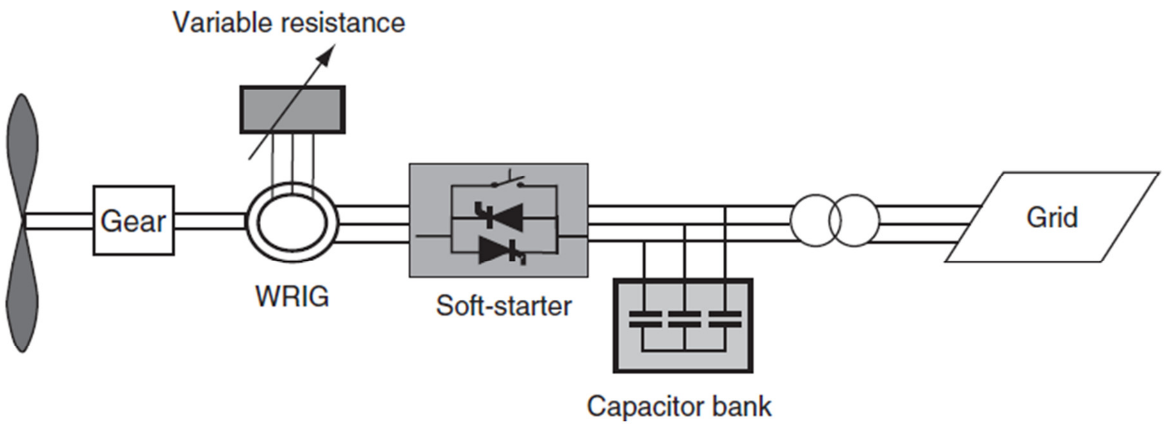

Figure 9: Type 2 wind system [8]

Type 3 and Type 4 wind systems can operate in a range of wind speeds and are perfect candidates for optimal energy extraction. The wind generators can continuously accelerate or decelerate to match the turbine rotational speed with the wind speed. Hence, maximum energy extraction is achieved by maintaining a constant tip-speed ratio. Furthermore, the mechanical torque stays more or less steady and thus wind speed variations cannot affect the power quality. The drawbacks of such systems are their increased cost and energy loss in the power converters. Type 3 and Type 4 systems are connected to the grid via power electronic converters which regulate the generator speed [8].

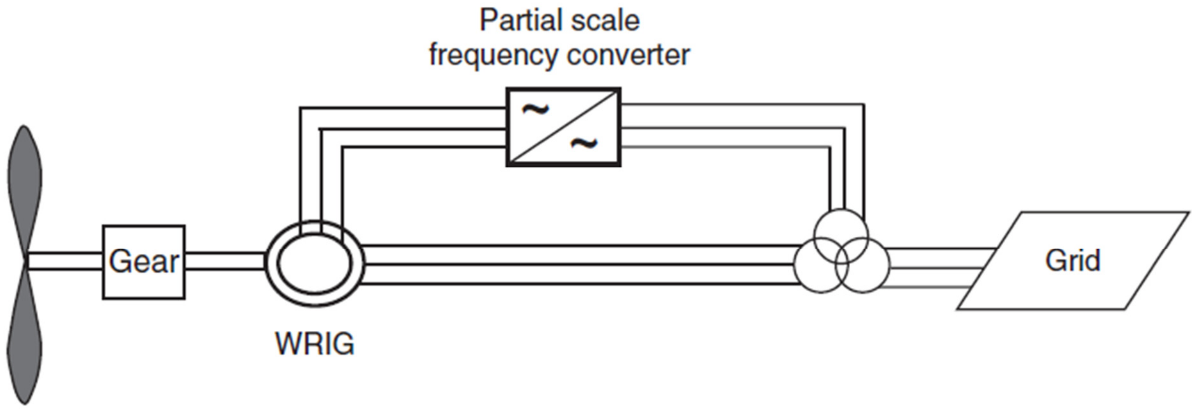

Figure 10: Type 3 wind system [8]

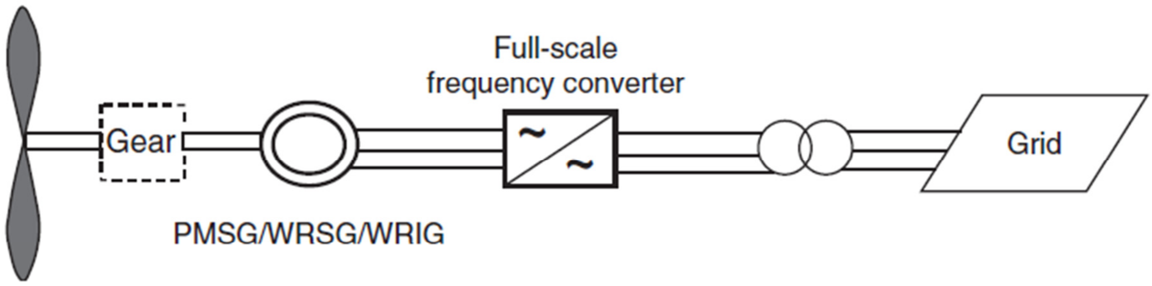

Figure 11: Type 4 wind system [8]

This thesis focuses on Type 3 and Type 4 wind system configurations. Type 3 uses a doubly-fed induction generator (DFIG) connected to a back-to-back partial-scale frequency converter. The converter manages only 30% of the generated power and its controllable speed range is -40% to +30% of synchronous speed. Type 4 utilizes either a PMSG, WRSG or WRIG connected to a full-scale frequency converter controlling 100% of the generated power. A Type 4 WRSG configuration has been considered in this thesis. The smaller converter size makes Type 3 cheaper than Type 4. [8]

2.3. Literature review

2.3.1. LVRT and HVRT strategies of Type 3 wind systems

There are some protection issues during grid voltage fluctuations for Type 3 wind generators. The first issue is overcurrents in the RSC of the converter. Excessive currents can damage the power electronic switches of the converter and negatively impact on wind generator operation. The second issue is overvoltages in the dc-link of the converter which can destroy the dc-link capacitor. It is essential to keep the dc-link capacitor intact because it acts as an energy buffer between the RSC and GSC and the dc source for their operation. Wind generators are also required to maintain grid voltage stability through appropriate regulation of reactive power.In the literature, it is seen that most researchers deal only with LVRT; i.e., voltage sags, while only a few take into account voltage swell impact on Type 3 wind systems. The solutions proposed can be broadly classified into three categories: (1) The use of advanced controllers instead of or in addition to conventional PI controllers to enhance ride-though performance, (2) Novel reorientation of existing vector control to counter the impact of voltage sags and (3) Implementation of specialized hardware for improved LVRT performance.

The first category of solutions is described henceforth. In [9], IMC (Internal Model Control) controller is implemented to improve Type 3 wind generator (WG) performance in the event of symmetrical voltage sags. The high current arising in the rotor-side converter (RSC) is bypassed via a crowbar circuit for protection of the converter. A crowbar circuit connected to the RSC is a set of resistors where thyristor-based switching is utilized to insert the resistors during voltage sags. The generator maintains connection with the grid during the disturbance and the synchronism of operation is kept unchanged. Grid voltage restoration is also performed by injecting reactive power from the grid-side converter (GSC) to the grid. A control scheme is designed to manage the transition of the system from the transient state to the steady state. The IMC controllers are designed for RSC current control and speed control using (1) and (2) where α represents the control bandwidth and $G(s)$ is the first order plant transfer function. The subscripts 'I' and 'ω' represent current and speed quantities. Equations (3) and (4) provide transfer functions of $G_I(s)$ and $G_\omega(s)$. L_r and R_r are rotor inductance and resistance respectively; J and B_a are inertia and active damping torque respectively.

$$C_I(s) = \frac{\alpha_I}{s} G_I(s)^{-1} \quad (1)$$

$$C_{\omega}(s) = \frac{\alpha_{\omega}}{s} G_{\omega}(s)^{-1} \tag{2}$$

$$G(s) = \frac{1}{L_r s + R_r} \tag{3}$$

$$G(s) = \frac{1}{Js + B_a} \tag{4}$$

IMC control is again implemented on the RSC and GSC in [10] for unbalanced voltage sags. A sequence decomposition method is utilized for current reference calculation in separate positive and negative sequences. The rotor-side current is decomposed into I_{rd}^{p}, I_{rq}^{p}, I_{rd}^{n} and I_{rq}^{n}, whereas the grid-side currents are I_{gd}^{p}, I_{gq}^{p}, I_{gd}^{n} and I_{gq}^{n}. The superscripts 'p' and 'n' denote positive and negative sequences respectively; the subscripts 'r'and 'g' represent rotor-side and grid-side components respectively; and 'd' and 'q' are d and q-axis components respectively. As a result, there are eight degrees of freedom available for current control. The impact of crowbar action is also incorporated in the control scheme. The authors use two-degree-of-freedom IMC control in [11] to improve ride-through performance during symmetrical voltage sags. For the design of the controller, the power and voltage limitations of the Type 3 WG converter are taken into account. A crowbar is turned on upon detection of either rotor overcurrent or dc-link overvoltage; the duration of the tripping signal is 20 ms. Equation (5) shows the conditions for crowbar action where V_{dc} and I_r are dc-link voltage and rotor converter current respectively.

$$\begin{gathered} V_{dc} > 1.3V_{dc} \text{ or,} \\ |I_r| > 1.2 \end{gathered} \tag{5}$$

PR (Proportional Resonant) control tuned at the grid frequency is developed for unbalanced voltage sags in [12]. No sequence decomposition is required for controlling positive and negative sequence currents. The RSC controller manages the double grid frequency electromagnetic oscillations, while there are three different control objectives for the GSC. Pulsations in the active or reactive power, and current output unbalances are reduced by the GSC. The authors emphasize more on restricting electromagnetic oscillations at double grid frequency rather than limiting RSC overcurrent and dc-link overvoltage. Vector-based hysteresis control is utilized on the RSC along with traditional PI control in [13]. Under steady grid condition, the Type 3 WG is operated with PI control, while hysteresis controllers are used during grid symmetrical or asymmetrical voltage sags. A supervisory control scheme is implemented to detect the voltage sags and swells, and it also implements a switching mechanism to transition between these two modes of operation. For the design of the hysteresis controller, all possible combinations of RSC gating signals (S_a, S_b and S_c) and eight switching states are considered. Hence, six non-zero (V_1 to V_6) and two zero (V_0 and V_7) voltage vectors are obtained at the output of the RSC. In Fig. 12, four-level and three-level hysteresis comparators are used to find the x and y tracking errors. Then the comparator outputs (D_x and D_y) are sent to a switching table which decides the RSC output voltage vector. Nevertheless, hysteresis control cannot be used on a long-term basis due to its variable frequency and low-order harmonic distortions. Hysteresis control is again implemented in [14] for current control to alleviate symmetrical voltage sags and swells. The design is focused to comply with requirements of the Australian grid code. Different P-Q capability curves for Type 3 WGs are extensively investigated to develop new strategies for the outer-loop power control. Reactive power support is also supplied to the grid during grid transients.

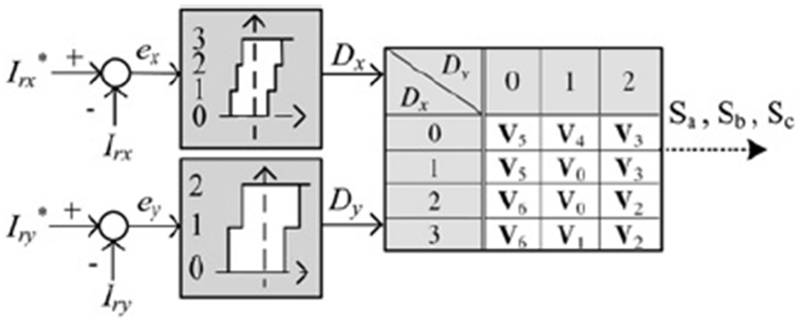

D_x \ D_y	0	1	2
0	V_5	V_4	V_3
1	V_5	V_0	V_3
2	V_6	V_0	V_2
3	V_6	V_1	V_2

Figure 12: Implementation of vector-based hysteresis control [13]

A robust sliding mode controller is designed in [15] where intrinsic grid uncertainties and disturbances are considered as perturbation and added to the nominal plant model. A sliding surface e is defined by (6) where $I_{\alpha r}$ and $I_{\beta r}$ are rotor currents in the $\alpha\beta$ coordinates; the superscript '*' represents reference values. The idea is to maintain the state trajectories on the surface $e = 0$ so that rotor currents track their respective reference values. A suitable Lyapunov function V given in (7) is chosen for the control signal u to keep the rotor current error on the sliding surface. Novel current reference values are generated for the controller in normal and faul-operation modes. The authors take into account both symmetrical and asymmetrical sags. A crowbar circuit is also employed.

$$e = \left[\begin{bmatrix} I_{\alpha r}^* \\ I_{\beta r}^* \end{bmatrix} - \begin{bmatrix} I_{\alpha r} \\ I_{I\beta r} \end{bmatrix}\right] = 0 \quad (6)$$

$$V(e) = \frac{1}{2} e^T e \tag{7}$$

In [16], an LQ (Linear Quadratic) control is proposed for the RSC and GSC to deal with symmetrical and asymmetrical voltage sags as shown in Fig. 13. The control scheme also incorporates usual post-fault conditions but the crowbar circuit is not fired. The nonlinearity in the power system is represented by an uncertain term derived from the Cauchy remainder of a Taylor expansion of the power system model. The limit on the uncertainty is calculated using genetic algorithm.

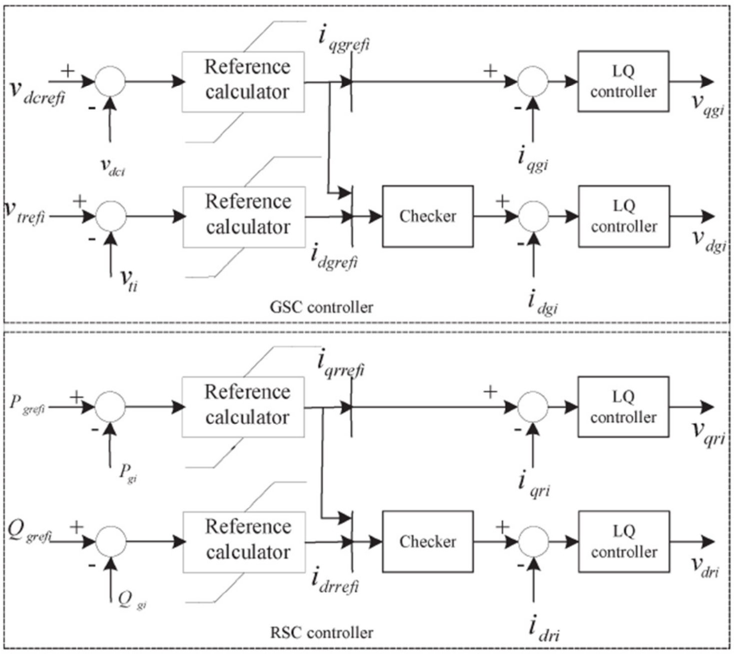

Figure 13: LQ controller [16]

A PIR (Proportional Integral Resonant) controller is presented in [17] for balanced and unbalanced faults. The paper utilizes traditional protection hardware like crowbar and dc-link chopper. The vector control scheme is re-configured by adding additional feed-forward terms to the current control inner-loop and power control outer-loop. 60 Hz and 120 Hz rotor current components are supplied during asymmetrical voltage sags and this reduces torque ripple and improves transient current control without any sequence decomposition. A three-phase phase locker loop (PLL) based on the synchronous reference frame is designed to focus on negative-sequence components rejection. A fuzzy controller is engaged in [18] for symmetrical voltage sags and swells where the Danish grid code is considered. The back-to-back converter is used as a reactive power source to regulate the voltage magnitude at the PCC. Power capability limits of the converter are investigated for efficient control of the wind system as given in (8)–(9). V_s, I_s, P_s and Q_s are voltage, current, active and reactive power of the stator in that order; P_t, P_r and s are total active power, rotor active power and slip respectively. The impact of load variation is also included in the study.

$$\begin{gathered} P_t = P_s + P_r \ where, \\ P_r = -sP_s \ and \ P_t = (1-s)P_s \end{gathered} \tag{8}$$

$$P_s^2 + Q_s^2 = (3V_s^2 I_s^2) \tag{9}$$

The authors implement a genetic algorithm-based fuzzy logic controller in [19] to coordinate between the RSC and GSC converters to improve LVRT performance. The optimization problem is changed to a *fitness function* which is a representation of the performance of the solution to the LVRT problem. All sets of variables of the problem are encoded into *chromosomes* which can be sub-divided into *genes.* Different solutions are represented by different chromosomes which form the *population*. The genetic algorithm assesses the fitness of the chromosomes and facilitates repopulation until a termination condition is satisfied. Lastly, no additional hardware is used here and only symmetrical voltage sags are considered. A nonlinear MPC (Model Predictive Control) controller is presented by the authors in [20] for unbalanced grid conditions. The prediction is calculated using the designed input-output feedback linearization scheme. The scheme calculates the d and q-axis rotor current components in the synchronous reference frame. On the other hand, the control law is established by optimizing an objective function which takes into account control tracking and economic index.

A resonant controller together with PI control is implemented in [21] to deal with asymmetrical voltage sags. There are two terms in the controller. One regulates the negative sequence component which has an angular frequency of $2\omega_s$, while the other regulates the natural component with angular frequency ω_s. The controller transfer function $G_c(s)$ is given in (10) where K_p and K_i are PI controller constants and K_{r1} and K_{r2} are resonant controller constants. However, some modifications on the converter current and voltage limits are required to counter deep voltage sags. A resonant feedback compensator is proposed in conjunction with PI control in [22] for unbalanced grid voltage conditions. There are four achievable control targets for the RSC, namely, balanced stator current, sinusoidal rotor current, smooth stator active and reactive powers and constant electromagnetic torque. On the other hand, the GSC has only one control target i.e., constant dc-link voltage. No sequence decomposition is required. The authors present an ADR (Active Disturbance Rejection) controller in [23] for symmetrical voltage sags. Load and wind speed variations are also studied in this paper. Reduced order generalized integrators are designed in [24] together with PI control to manage network unbalance. The integrators are tuned at twice the grid frequency 2ω and their transfer function is given in (11). K_r and ω_c are resonant gain and cut-off frequency respectively. The RSC is regulated to reduce torque ripples, while the GSC has three control targets, namely, suppression of current unbalance, and oscillations in the active and reactive power.

$$G_c(s) = K_p + \frac{K_i}{s} + \frac{K_{r1}s}{s^2 + (\omega_s)^2} + \frac{K_{r2}s}{s^2 + (2\omega_s)^2} \tag{10}$$

$$G_R(s) = \frac{K_r\omega_c}{s + j2\omega + \omega_c} \tag{11}$$

The second type of ride-through solutions for Type 3 WGs comprises unique reorientation of traditional vector control to mitigate the impact of voltage sags and swells. The most common reorientation method is to design new current reference generation strategies for the Type 3 WG controllers. Other reorientation methods consist of flux manipulation, additional feed-forward terms, demagnetizing current, virtual resistance and storage of kinetic energy. In [25], a current reference generation is designed in the positive and negative synchronous reference frame to deal with unbalanced network. The d-q axis rotor currents are separated into positive and negative sequence components $(I^{+}{}_{rd+}, I^{+}{}_{rq+}, I^{-}{}_{rd-}\ and\ I^{-}{}_{rq-})$ and fed into two PI controllers. There are four control targets: balanced stator current, constant active power, constant electromagnetic torque and elimination of rotor current oscillation. The authors present a coordinated control strategy for the RSC and GSC in [26]. There are two controllers: a main controller in the positive d-q reference frame and an auxiliary controller in the negative d-q reference frame. However, no sequence decomposition is required.

In [27], separate controllers are proposed in the positive and negative sequence for unbalanced grid voltage condition. Two methods are implemented and compared for the real-time separation of positive and negative components. It is found that the 'signal delay cancellation' method is much faster than the 'low-pass filter' method. The reference currents for the RSC and GSC are calculated according to the instantaneous reactive power theory. The paper emphasizes on limiting torque and dc voltage ripple. A new control strategy is designed for the RSC in [28] where the feedback of measured stator currents is used as reference for the RSC controller during voltage sags. This generates current waveforms in the stator in counter phase but with the same shape as the voltage sag. Consequently, stator overcurrents get reduced which, in turn, decreases rotor ovecurrents. Nevertheless, the controller tracks P-Q references in steady state. A switch is utilized to control the transition between transient and steady states. In [29], the effect of asymmetrical faults on Type 3 WG control is analyzed. A control scheme is designed for asymmetrical grid faults by using unique current reference in the positive and negative sequences obtained from DFIG electrical equations. Multiple control objectives such as regulation of positive-sequence active power (P_{s0+}), positive-sequence stator reactive power (Q_{s0+}), positive-sequence GSC active power (P_{l0+}) and reactive power (Q_{l0+}), dc-link voltage and torque oscillations can be chosen.

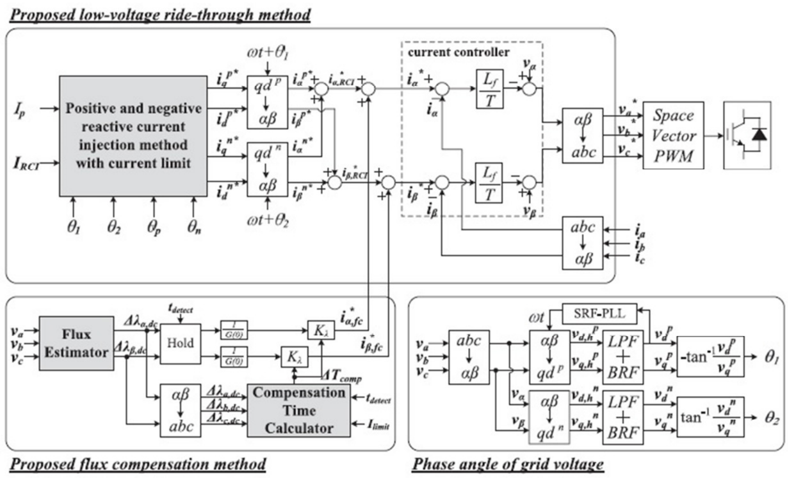

Figure 14: RCI-flux compensation based control scheme [30]

An LVRT strategy is developed in [30] which is based on reactive current injection (RCI) and flux compensation presented in Fig. 14. Flux compensation mitigates the flux offset induced by voltage sags and thereby limits the RSC inrush current. Positive sequence capacitive current is supplied to support the PCC voltage and negative sequence inductive current is injected to alleviate the voltage unbalance. The phase currents are connected to the positive and negative sequence currents as shown in (12)-(14), where α is calculated using voltage phase angles θ_1 and θ_2.

$$I_{a,peak} = \sqrt{I_p^2 + I_n^2 + 2I_pI_n \cos\alpha} \tag{12}$$

$$I_{b,peak} = \sqrt{I_p^2 + I_n^2 + 2I_pI_n \cos\left(\alpha + \frac{4\lambda}{3}\right)} \tag{13}$$

$$I_{c,peak} = \sqrt{I_p^2 + I_n^2 + 2I_pI_n\cos\left(\alpha - \frac{4\lambda}{3}\right)} \quad (14)$$

A reference calculation strategy based on stator flux-oriented vector control is proposed in [31] to improve the dynamic performance of a Type 3 WG in the event of grid voltage unbalance. Additional compensation terms are included to current references to mitigate active power, reactive power, torque oscillations. The RSC controls torque, active and reactive powers, while the GSC regulates dc-link voltage oscillations and maintains unity power factor. All the control objectives can be met simultaneously in this strategy. The scheme also eliminates the requirement for dual vector control and hence only four PI controllers are sufficient instead of eight. The Indian Electricity Grid Code (IEGC) has been taken into account for performance evaluation. A flux weakening control is presented in [32] for grid fault ride-through without the need of any additional hardware. The control scheme is divided into three segments: (a) stator-flux linkage estimation and decomposition into positive, negative and zero sequence components; (b) rotor reference current generation; and (c) application of rotor current control. In this method, control action happens before the rotor current reaches an undesirable level. Therefore, fast observation of stator flux is key to the success of this method. An LVRT control strategy based on flux linkage tracking is designed in [33]. The tracking mechanism regulates the rotor flux linkage to track a fraction of the stator flux linkage according to (15), and this decreases the short-circuit rotor current. The limiting of rotor current is done with minimal torque oscillation. k_T is the tracking gain and it should satisfy (16). L_{ls} and L_{lr} are leakage stator and rotor inductances respectively, and I_{rotor_max} is the maximum allowable rotor current. A proportional controller (P) instead of a proportional-integral (PI) is used because the rotor flux linkage needs to be close to the stator flux linkage. Therefore, a steady-state error is acceptable in this case as the controller is not required to maintain a certain fixed value.

$$\vec{\psi}_{rotor} = k_T\vec{\psi}_{stator} \quad (15)$$

$$\frac{1 - k_T}{L_{ls} + L_{lr}}\psi_s(0) \le I_{rotor\_max} \quad (16)$$

A virtual damping flux-based control scheme is proposed in [34]. The virtual damping counters the stator transient flux, thereby, decreasing its effect on the rotor internal voltage. As shown in Fig. 15, the rotor current reference calculation is dependent on two constants k_1

and k_2, which link the stator and rotor currents to the virtual flux φ_v. A negative sequence current compensation scheme is utilized to deal with asymmetrical faults, while traditional vector control is adopted for symmetrical faults. The authors have developed an innovative control scheme in [35] to ride through recurrent grid faults. The control scheme speeds up the decay of the stator natural flux, ψ_{sn}, after voltage recovery. In order to accomplish this, the RSC generates rotor currents with two different frequencies, namely, the rotor natural current ($\vec{\iota}_{rn}$) and the rotor forced current ($\vec{\iota}_{rf}$). $\vec{\iota}_{rn}$ is generated in the opposite direction ψ_{sn}, while $\vec{\iota}_{rf}$ is generated in the opposite direction of stator forced flux, ψ_{sf}. A crowbar circuit is also utilized.

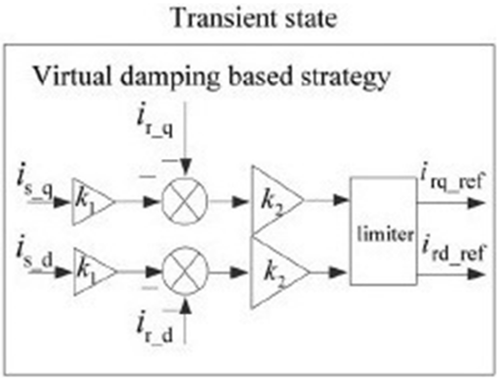

Figure 15: Virtual damping based control [34]

The authors consider symmetrical voltage dips in [36] by designing a scheme that reduces the crowbar circuit activation time and utilises demagnetizing current. The crowbar is activated only at the start of a fault and then the operation of the RSC is recommenced. A demagnetizing current is then injected in the opposite direction of the stator natural flux, $\vec{\psi}_{sn}$, to reduce its effect on the rotor. The current ($\vec{\iota}_{rn}$) needed to counter the stator natural flux is generated using (17), where L_s, L_r and L_m are stator, rotor and magnetizing inductances in that order; and σ is the leakage coefficient. The converter also progressively injects synchronous current for reactive power generation. Hence, it is ensured that the sum of demagnetizing current and synchronous current does not exceed the converter current ratings. A virtual resistance and demagnetizing current based control strategy is proposed in [37] to reduce rotor overcurrents during grid faults without using a crowbar. The inner loop current control consists of a partial feedback which is similar to series resistance with the DFIG rotor. Reactive power supply is also provided depending on the voltage dip. A fast fault detection algorithm is developed to switch smoothly between normal and LVRT modes.

$$\vec{\iota}_{rn} = \frac{-L_m}{L_s}\frac{1}{\sigma L_r}\vec{\psi}_{sn} \tag{17}$$

The machine magnetizing current control is presented in [38] to enhance system response for symmetrical dips. The strategy is to control the generator magnetizing current to raise stator flux damping. This reduces the stator flux linkage oscillations which, in turn, decreases torque and power fluctuations. Equation (18) provides the magnetizing current; where I_{rq} and I_{sq} are quadrature components of rotor and stator currents correspondingly. No voltage sag detection mechanism is required because the magnetizing control is always on. Reactive power compensation is also provided in this scheme. In [39], an improved demagnetization control is presented ride through balanced grid faults as shown in Fig. 16. The authors focus only on the control of the RSC and the GSC control is ignored. A demagnetizing rotor current as given in (19) is supplied under balanced grid faults to counter the natural stator current, thereby, accelerating the damping of the stator flux. The critical value of K is calculated using (20).

$$I_m = -\left(I_{rq} + I_{sq}\right) \tag{18}$$

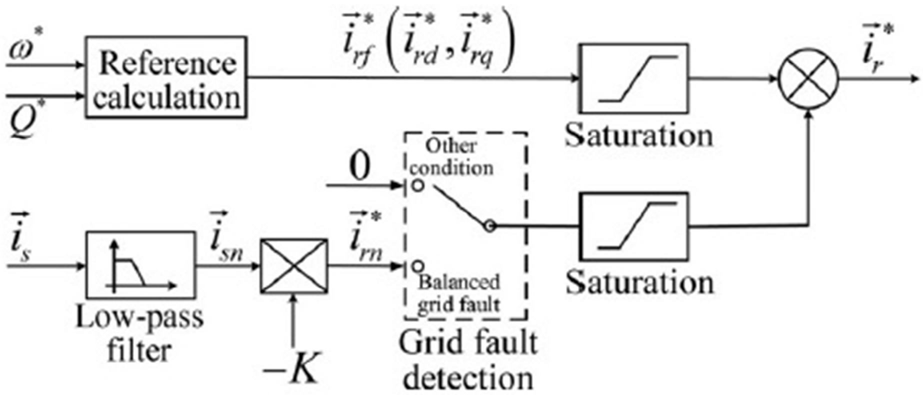

Figure 16: Improved demagnetization control [39]

$$\vec{\imath}_{rn} = -K\vec{\imath}_{sn} \tag{19}$$

$$K_{critical} = \frac{L_s}{L_m} \tag{20}$$

Feed-forward transient current control is developed in [40] for ride-though of Type 3 WGs during voltage sags. The traditional current control consists of additional feed-forward transient compensations shown in Fig. 17. In steady-state, $\omega_{\lambda s} = \omega_s$, $v_{ds}^e = 0$ and $v_{qs}^e = \omega_s \lambda_{ds}^e$, this makes the feed-forward transient control scheme same as the conventional control. A crowbar is also utilized in this scheme. An advanced control scheme is developed in [41] where the RSC controller transforms the power imbalance during voltage sags to kinetic energy of the wind turbines. This is accomplished by increasing the rotor speed by making the generator torque reference equal to zero in the event of a grid fault. In case there is overspeeding of the generator rotor, power extraction is reduced with the help of the pitch control. After the fault is cleared, the stored kinetic energy is slowly fed back to the grid. The GSC controller includes a compensation term to dampen dc-link voltage fluctuations. An LVRT scheme is proposed in [42] where a portion of the extracted wind energy is transferred to rotor inertia energy during faults. The stored energy is then fed back into the grid smoothly. The scheme comprises advanced reactive power regulation to augment the grid voltage. Multi-stage switching is utilized depending on the fault voltage development.

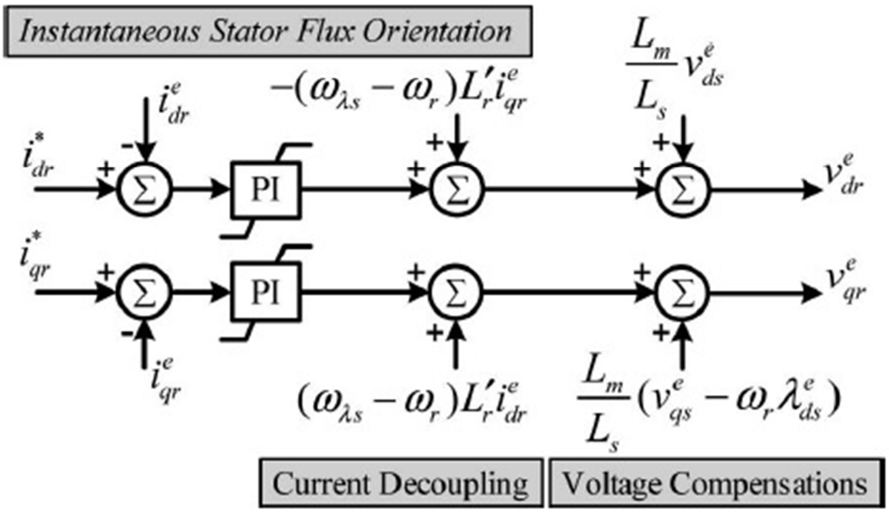

Figure 17: Feed-forward transient current control [40]

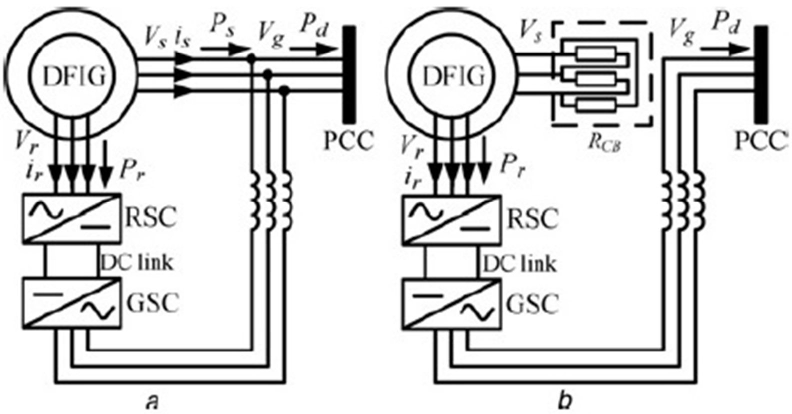

Figure 18: (a) DF mode; (b) IG mode [43]

A mode-switching LVRT strategy is presented in [43]. When a grid fault is detected, the generator changes from Doubly-Fed (DF) mode to Induction Generator (IG) mode as shown in Fig. 18. The stator windings are disengaged form the grid and short-circuited in the IG mode. A stator-connected crowbar is utilized to limit transient currents and a mechanism to re-engage the stator to the grid through re-synchronization is used. A coordinated control strategy with active and reactive power support is presented in [44]. The d and q axes current loops regulate desired reactive $\left(Q_{sf}^{ref}\right)$ and active (P_{sf}^{ref}) powers according to (21)-(22), where γ is the voltage drop coefficient. i_{rd}^{ref} and i_{rq}^{ref} have to satisfy (23) to stay within the maximum converter current capacity. A dc-chopper circuit is utilized to avoid dc-link overvoltage. The authors also focus power control in a post-fault scenario.

$$i_{rd}^{ref} = -\frac{Q_{sf}^{ref} L_s}{\gamma L_m} + \frac{\gamma}{L_m} \tag{21}$$

$$i_{rq}^{ref} = -\frac{P_{sf}^{ref} L_s}{\gamma L_m} \tag{22}$$

$$i_{rq}^{ref} = -\sqrt{4 - \left(i_{rd}^{ref}\right)^2} \tag{23}$$

A scaled stator current tracking based control for the RSC is designed in [45]. This is utilized so that flux observation errors and complexities resulting from sequence separation can be avoided. The rotor current tracks the stator current with a suitable tracking coefficient and in the opposite direction. By selecting the right value of the tracking coefficient, the rotor current and voltage are kept within the RSC's limit. Reactive current is also supplied to support the grid voltage. In [46], a novel rotor-side control scheme is presented to augment LVRT performance of DFIG's under severe voltage sags. No additional hardware is utilized in this scheme. The new scheme is able to mitigate voltage and current transients on the rotor side during abnormal grid conditions. This is done by accelerating the decay of the dc component of the stator flux during grid voltage fluctuations. According the (24), the decay of the flux is dependent on the stator resistance and dc-component of the stator winding current where ψ_{ds_sc} is the d-axis component of the stator dc flux, R_s is the stator resistance and i_{ds_dc} is the d-axis component of the stator dc current. Changing the stator resistance is not a good option because it can cause unnecessary transients. Therefore, the dc damping effect is increased by aligning the rotor current in the rotor frequency in the opposite direction of the stator dc flux. The authors also provide a detailed analysis of the dynamic behavior of DFIG's during voltage transients.

$$\frac{d\psi_{ds\_dc}}{dt} = -R_s i_{ds\_dc} \tag{24}$$

The third and final type of ride-through solutions involves utilization of specialized hardware for enhanced LVRT of Type 3 WGs. Conventionally, crowbar circuits have been used on the rotor windings to suppress the RSC overcurrent and dc-link chopper circuit across the dc-link capacitor to suppress the overvoltage during grid faults. Both hardware pieces have a shunt topology and are regulated using power-electronic switches. Crowbars are not appropriate for wind farms anymore because converter control is lost during grid disturbance. Furthermore, the DFIG acts like a squirrel-cage generator and absorbs reactive power from the grid resulting in further deterioration. DC-link chopper circuits are still suitable for use without violating the requirements of modern grid codes.

Recent works have emphasized on protective hardware utilizing a series topology. A Series Dynamic Resistor (SDR) connected to rotor terminals is implemented in [47] along with crowbar and dc-link chopper circuits. The authors try to enhance LVRT performance for both symmetrical and asymmetrical voltage sags. A coordinated switching scheme is used for the SDR, crowbar and dc-link chopper as shown in Fig. 19. The crowbar is engaged only for a short time at the beginning and end of the fault. This is done to keep the converter under control. In [48], a Series Dynamic Braking Resistor (SDBR) connected to the stator is engaged which works in coordination with a dc-link chopper. The SDBR is bypassed in normal operation by turning on a switch; whereas, the switch is turned off during a fault to insert the SDBR in series with the stator.

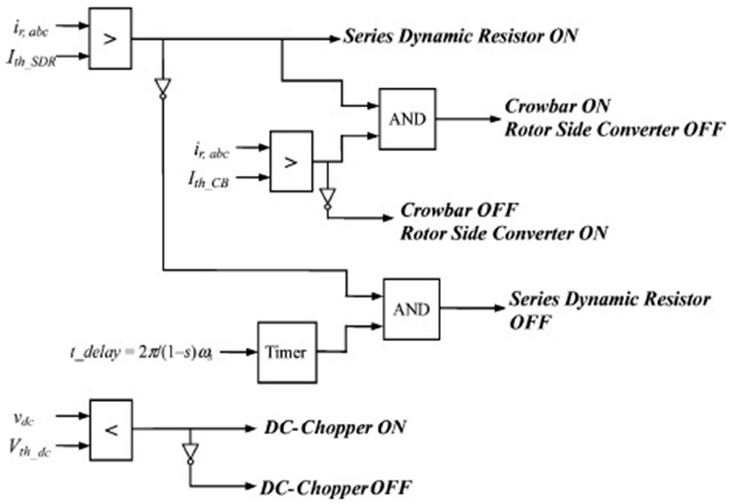

Figure 19: Switching strategy [48]

A Modulated Series Dynamic Braking Resistor (MSDBR) connected to the stator windings is proposed in [49] for improved Type 3 WG performance during symmetrical and asymmetrical voltage sags. The protection scheme comprises a voltage booster to provide series voltage compensation and power evacuation during grid faults. The paper also offers reactive power support with a new voltage reference calculation algorithm. A novel fault detection algorithm is designed by the authors and load variation is also included in the study. A protection strategy is proposed in [50] using parallel capacitors or super-capacitors across the dc-link capacitor for symmetrical and asymmetrical voltage sags. A resistor is also connected in parallel with the additional capacitors/super-capacitors for power evacuation. The charging and discharging of the additional capacitors/super-capacitors is regulated using power-electronic switches. In [51], a series capacitor regulated by power-electronic switches is connected to the rotor windings for enhanced LVRT performance. The series capacitor is bypassed in normal operation, and it is introduced as soon as a fault is detected.

A nine-switch converter is implemented for the GSC in [52] for superior LVRT operation. There is no requirement for an additional series transformer connected to the GSC in this strategy. A dynamic braking resistor (DBR) is connected in parallel with the dc-link capacitor for power evacuation during grid transients. The nine-switch converter control consists of two controllers: GSC controller and series voltage compensation controller, which regulate the lower and upper outputs of the nine-switch converter in that order. Parallel interleaved converters are deployed in [53] to improve DFIG performance during three-phase faults. A series dynamic braking resistor (SDBR) is also engaged at the stator side. The parallel configuration allows for greater flexibility in selecting appropriate voltage vector to enhance switching and commutation condition.

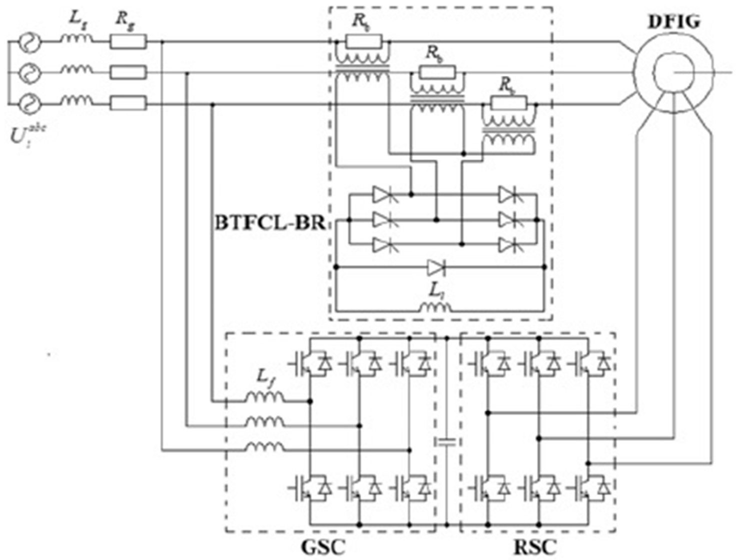

Figure 20: BTFCL-BR topology [54]

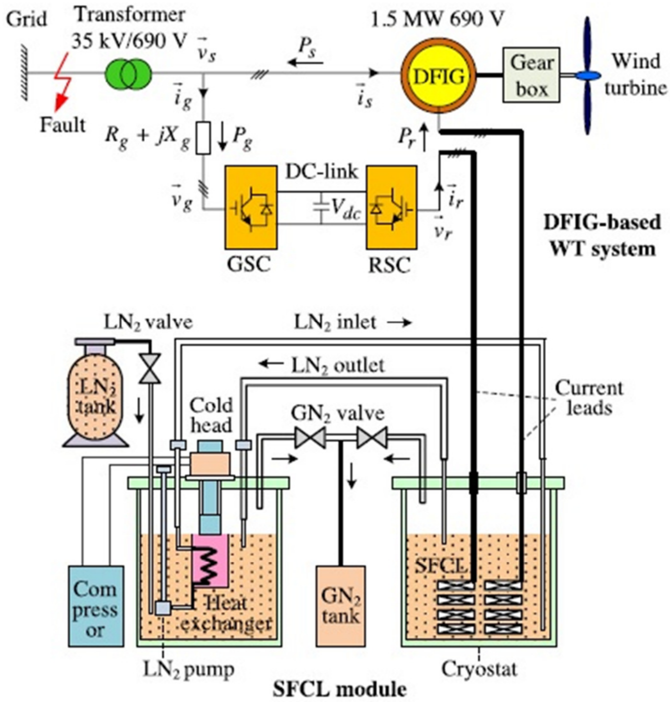

Figure 21: SFCL employed Type 3 WG system [55]

Bridge-type fault current limiters (BTFCL) are used for improving LVRT capability of Type 3 WGs in [54]. Three types of BTFCLs are studied in this paper, namely, BTFCL, BTFCL-CRC (current regulating circuit) and BTFCL-BR (bypass resistor). A common BTFCL comprised coupling transformers, a diode bridge and a fault current limiting inductor (FCLI). The diode bridge conducts fully during normal operation as long as the stator current is lower than the FCLI current. When the stator current is greater than the threshold value, the FCLI is inserted into the stator circuit. This restricts the rate of increase of the fault phase current. In the BTFCL-CRC topology, an additional chopper circuit is connected in series with the dc-link of the diode bridge and the FCLI. The CRC is regulated to maintain a constant reference value for the FCLI current. In the BTFCL-BR topology shown in Fig. 20, a bypass resistor is connected in parallel with the transformer's primary side. A thyristor bridge is used for activating and deactivating the bypass resistor. The main focus of this paper is the BTFCL-BR topology.

A switch-type fault current limiter (STFCL) is engaged in [55] to augment Type 3 WG LVRT capability. The STFCL can insert fault-current-limiting inductors in series with the stator circuit in the event of a grid fault. It also has energy absorption capability which can absorb excess energy stored in the stator. This avoids any overvoltage in semiconductor devices. A new superconducting fault current limiter (SFCL) connected in series with the rotor windings is developed in [56] to counter symmetrical and asymmetrical faults as shown in Fig. 21. The SFCL is of resistive type and its high resistance restricts the magnitude of the fault rotor current. There is also a large reduction in the time of the rotor flux linkage expressed as $\tau_r = \sigma L_r/(R_{SFCL} + R_r)$, where σ is the leakage factor. In [57], the authors emphasize on the optimization of a superconducting coil (SC) incorporated into the DFIG dc-link to improve LVRT capability. In normal operation, the SC behaves as energy storage to exchange energy with the system. Nevertheless, it behaves as a current limiting inductor during grid faults. The optimization algorithm tunes the SC inductance, the initial required stored energy in the SC and PI parameters simultaneously to achieve enhanced performance.

In [58], improved fault ride through is accomplished through active and passive compensators. The role of the active compensator is the regulation of the RSC and GSC by means of unique reference generation for the current controllers. The reference generation algorithm consists of sequence decomposition of the stator current and using the single components as reference for the rotor current. Whereas, the passive compensator is a three-phase rotor current limiter (RCL) resistor connected in series with the rotor windings. It comprises three resistors in parallel with three bypassing bidirectional static switches. The switches are closed when the rotor current is less than or equal to the threshold current value, $I_{abc} \leq I_{th\_RCL}$, so the rotor current bypasses the RCL resistors. When $I_{abc} > I_{th\_RCL}$, the switches are turned off and the rotor current flows through the series resistor.

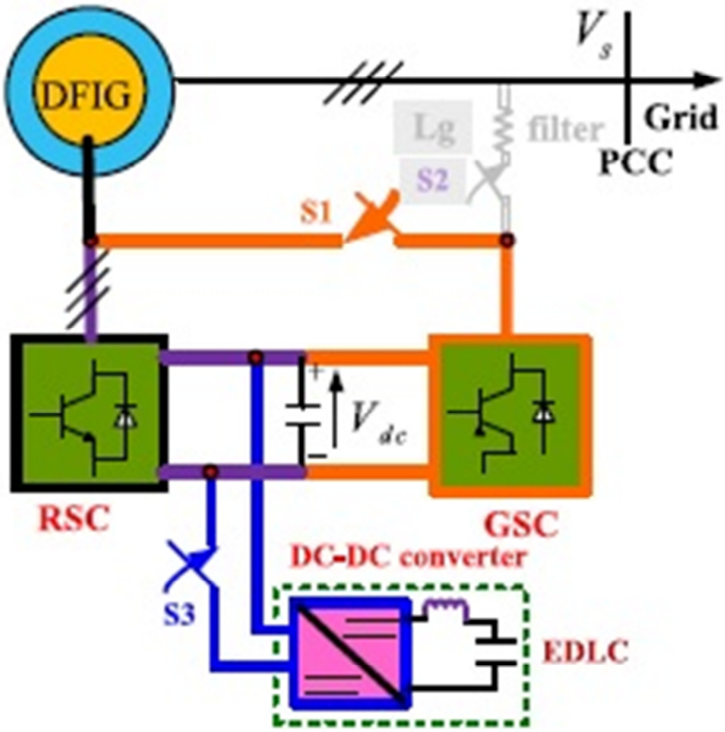

Figure 22: DFIG-ESD system [59]

The authors attempt to improve LVRT performance of Type 3 WGs with an energy storage device (ESD) in [59] as given in Fig. 22. The connection of the GSC is restructured so that it is connected in parallel with the RSC. This provides an additional path for the rotor current and the ESD controls the dc-link capacitor voltage. Electric double-layer capacitors are used as the ESD. Demagnetizing current is also injected to alleviate the effect of stator flux components. Reactive current is injected to support the grid voltage. Resonant controllers are added to conventional PI controllers during transients.The authors present a new dc-link controllable fault current limiter (C-FCL) in [60] to improve fault ride-through capability of DFIG’s. The C-FCL is placed between the RSC and the dc-link. An additional diode bridge is used in the dc-link to suppress ripples in dc-link current which could result in a voltage drop. There are four main parts in the C-FCL: a diode rectifier bridge, a copper coil, a semiconductor switch and a dc voltage source. A ZnO surge arrester is also employed to avoid any component damage due to voltage overshoot across the FCL. In normal operation, the C-FCl is bypassed and all the diodes of the diode bridge rectifier are ON. In a fault situation, the dc-link current reaches a certain predefined value which turns off the semiconductor switch. As a result, the copper coil resistance is inserted into the circuit which dissipates any excess energy. Excessive currents in the rotor are limited during balanced and unbalanced grid faults and DFIG’s can operate even at zero grid voltage. AC crowbar is not utilized in this scheme.

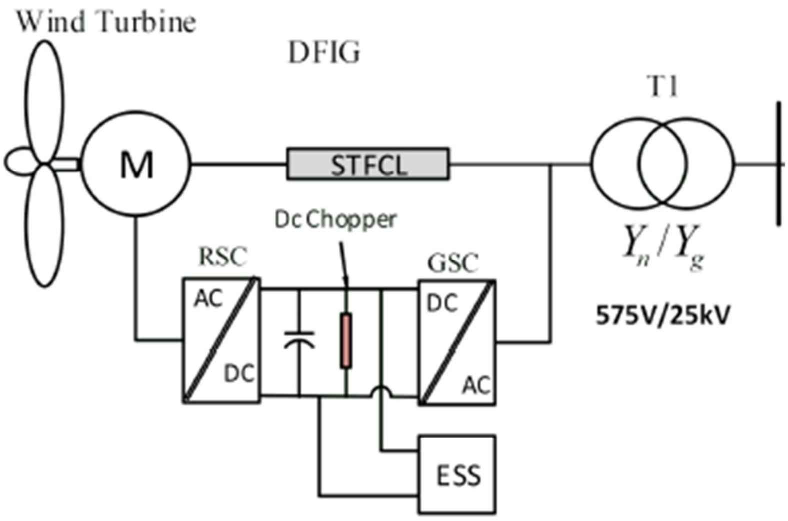

Figure 23: DFIG wind generator with hybrid scheme [61]

In [61], a hybrid scheme comprising switch type fault current limiter (STFCL), braking chopper and energy storage system (ESS) is employed to enhance ride through capability of DFIGs under symmetrical and asymmetrical grid faults as shown in Fig. 23. The scheme limits overcurrents in the RSC and dc-link. Mechanical stress is also reduced by the smoother electromagnetic torque achieved by the hybrid scheme. During a fault, the STFCl diverts the flow of current and absorbs excess fault energy thereby limiting the fault current. The braking chopper is used in parallel with the dc-link capacitor. An alternative path is provided for overcurrents during a fault to dissipate the excess energy. The ESS is a rechargeable battery which mitigates dc-link voltage fluctuation by continuously charging and discharging the battery. The authors propose the implementation of a series voltage compensator (SVC) for DFIG's to ride through grid disturbances in [62]. This technology consists of an independent energy storage system, a converter to charge the SVC dc-link (series charger converter – SCC) connected to the grid via a single turn primary transformer (STPT) and a converter to control the generator stator flux (control stator flux converter – CSFC) as in Fig. 24. During a voltage sag, the SVC controls the stator voltage so that that stator flux is properly controlled. The SVC absorbs power from the grid through a transformer with a single turn in the primary side and supplies power to the system via an LC filter.

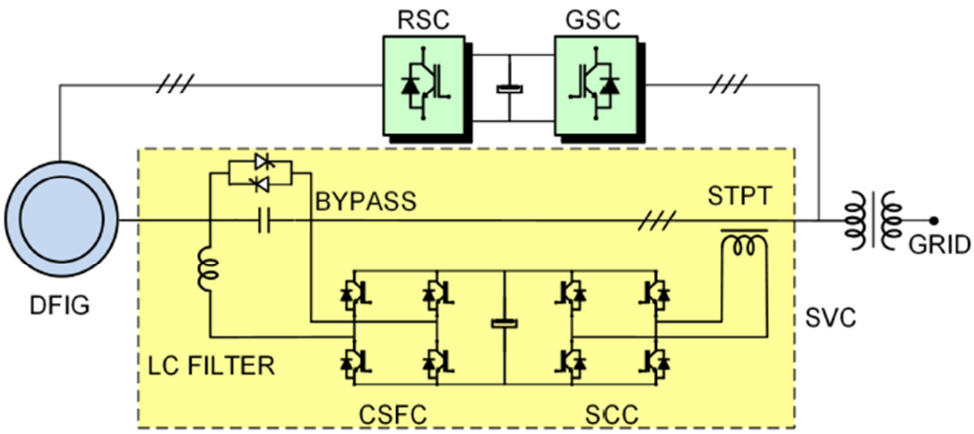

Figure 24: SVC-based scheme to enhance FRT [62]

In [63], a modified superconducting magnetic energy storage-fault current limiter (SMES-FCL) is proposed to improve DFIG ride-through performance. A superconducting coil (SC) is connected in parallel to the dc-link capacitor with the help of a current-voltage converter. During normal condition, the SC acts as an energy storage device. When a grid fault occurs, the SC behaves as a fault current limiter due to the rapid charging rate of the SC current. A large impedance in induced in the stator which restricts the fault current. Any excess energy from the dc-capacitor is absorbed by the SC thereby suppressing any overvoltage in the dc-link. The authors propose a capacitive bridge-type fault current limiter (CBFCL) to enhance LVRT of DFIGs in [64]. The CBFCL consists of a resistor in series with an AC capacitor connected in parallel with a full diode bridge circuit. During a fault condition, the DC reactor restricts the rise of the short circuit current and thus prevents an instantaneous voltage drop. The main objective of the CBFCL is to insert the capacitive limiting resistance in series with the faulted line. Therefore, DFIG rotor speed deceleration is avoided due to the fact that the resistor dissipates any surplus energy. Also, the capacitor provides reactive power which aids in fast voltage recovery.

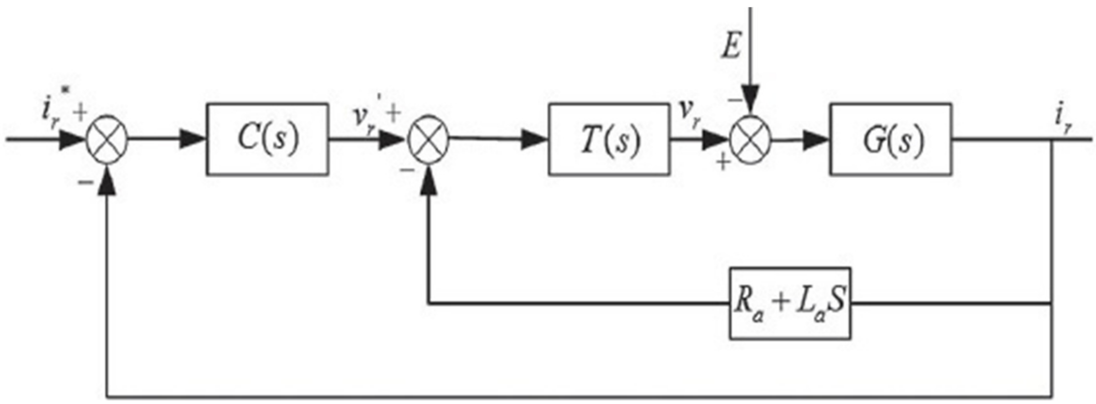

Figure 25: Current control loop [65]

It is important to note that many of the works mentioned so far use a combination of the three types of solutions. Only one paper focuses exclusively on HVRT or voltage swells by using virtual impedance [65]. Two feedback terms, R_a and $L_a s$ are added to the current control loop as shown in Fig. 25, which are equivalent to a series resistance and inductance respectively. One LVRT scheme for unbalanced grid voltage does not fall under any of the three types. This new control scheme is called the dynamic programming power control plus (DPPC+) which replaces the entire traditional vector control scheme [66]. DPCC+ regulates the RSC to control stator active and reactive power. The Bellman theory is used for DPCC+ for optimal control of discrete-time systems. A quadratic time-domain cost function is defined to determine the optimum policy at any given time.

2.3.2. LVRT and HVRT strategies of Type 4 wind systems

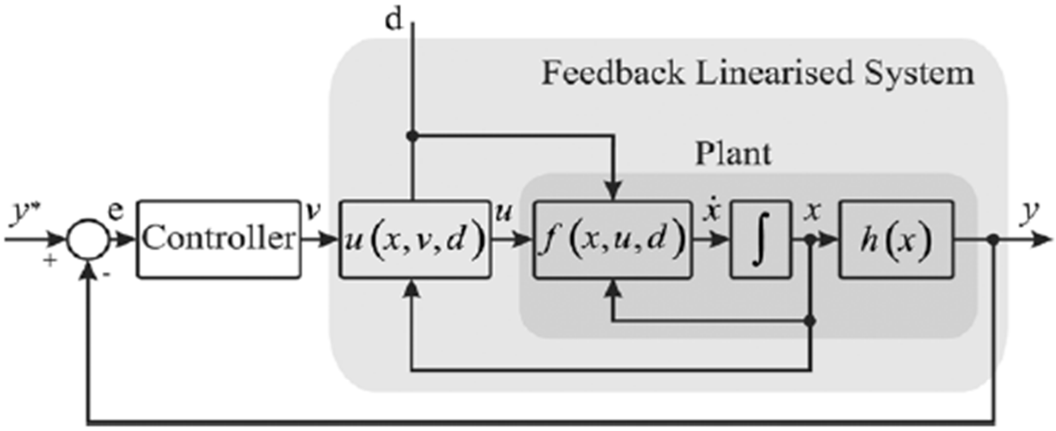

Figure 26: Feedback linearized system configuration

In the literature, most papers focus on ride-through strategies for Type 4 PMSG wind turbine generators; only a few papers deal with Type 4 WRSG and WRIG wind generator ride-through strategies. The ride-through strategies for all type 4 wind generators can also be largely classified into three types. The first type involves the utilization of advanced controller to improve ride-through capability. In [67], a nonlinear controller is developed using feedback linearization to augment network voltage during a fault. Feedback linearization changes the dynamics of a nonlinear system and facilitates the implementation of linear control techniques. Input-output feedback linearization is used to determine a linear relationship between a new input, v, and the plant output, y as shown in Fig. 26. Feedback linearization via a sliding mode method is implemented in [68]. The aim of the sliding mode controller is to design an equilibrium surface so that the state trajectories of the system follow a preferred behaviour when limited to the surface. The Lyapunov function in (25) is used to assess the stability of the controller where S is the sliding surface.

$$V = \frac{1}{2} S^T S \tag{25}$$

A ride-through strategy based on feedback linearization is presented in [69]. The generator-side converter regulates the dc-link voltage; while, the grid-side converter regulates the grid active power. A new power reference, P_g^*, is calculated for the grid-side converter using (26). P_t is the maximum power of the wind turbine; J is the turbine inertia and ω_m is the mechanical speed; C and V_{dc} are dc-link capacitance and voltage.

$$P_g^* = P_t - J\omega_m \frac{d\omega_m}{dt} - P_{loss} - CV_{dc}\frac{dV_{dc}}{dt} \tag{26}$$

In [70], a Multiple-Input-Multiple-Output (MIMO) sliding mode controller is presented to enhance LVRT capability for symmetrical voltage sags as shown in Fig. 27. The controller is developed through second-order sliding mode methods using two-stage cascade structure. A switching algorithm is also prepared to improve LVRT performance.

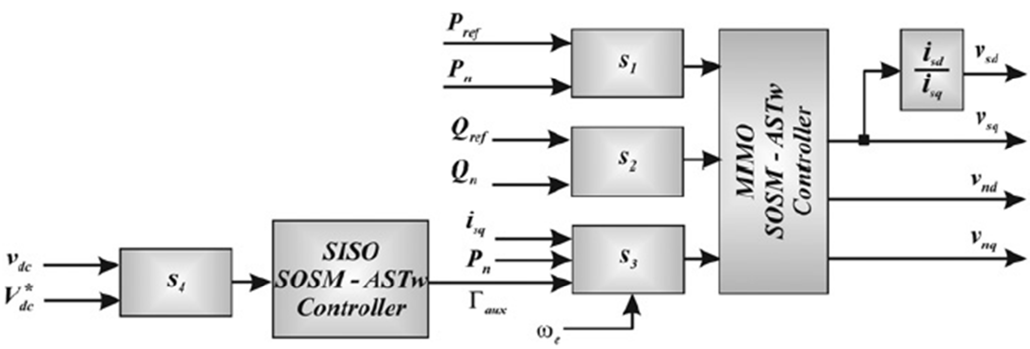

Figure 27: MIMO control scheme [70]

Three different Linear Quadratic Regulators (LQR) are designed in [71] for countering asymmetrical voltage sags. They are VCCF (vector current controller with feed-forward of negative-sequence grid voltage), DVCC1 (dual vector current controller) and DVCC2. VCCF is implemented in the positive reference frame, while the negative-sequence voltage is included in the reference voltage. DVCC consists of two steps. The first step comprises sequence separation, synchronization and current reference value calculation. In the next step, the current controller is then utilized in both the positive and negative reference frames. Two different current reference generation calculations are executed for DVCC1 and DVCC2. It is concluded that the selection of controllers is dependent on system constraints and

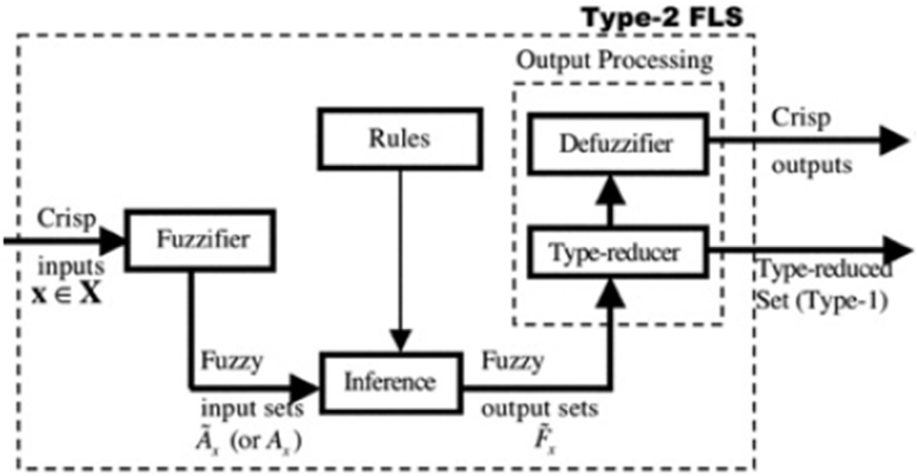

Figure 28: Type-2 fuzzy controller [72]

The authors design an interval type-2 fuzzy logic controller as shown in Fig. 28 in [72] for superior LVRT where both symmetrical and asymmetrical voltage sags are taken into account. The nonlinear relationship between the generator speed and dc-link voltage are incorporated into the controller design. Three scaling factors, K_e, K_{de} and K_i, are utilized to scale the inputs and output of the fuzzy controller. The coefficients can be either constants or variables, and they play a vital part in achieving the preferred behaviour in transient states. In [73], a hybrid valve switching and control scheme is presented to provide smooth operation of wind generators in the event of single line to ground faults. The scheme consists of two stages. In steady-state, sinusoidal pulse width modulation (SPWM) based valve switching is executed. Upon detection of a temporary fault, hysteresis space vector modulation (HSVM) is applied. SPWM valve switching control is utilized to operate the converter as a current-regulated voltage source; while HSVM runs the converter as a controlled current source. A supervisory controller controls the switching between SPWM and HSVM.

.

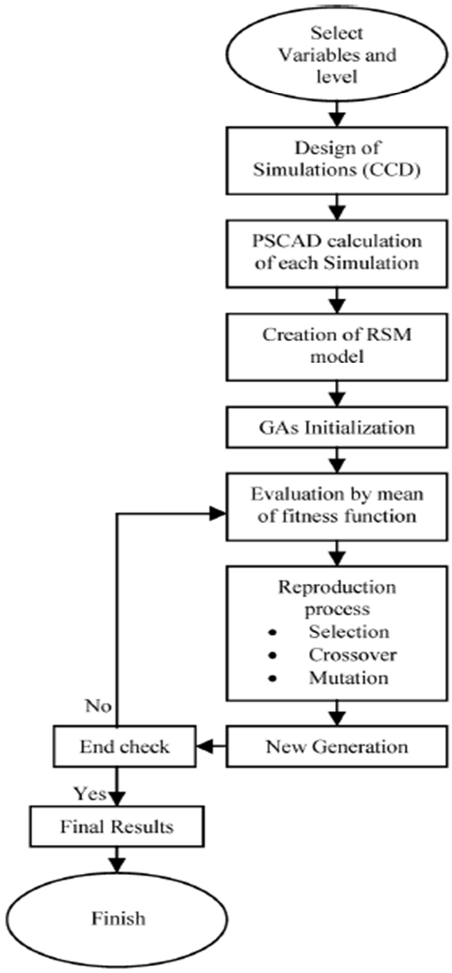

Figure 29: GA-RSM design optimization [73]

The authors propose a design optimization method for PI controller parameters in [74] to deal with symmetrical and asymmetrical faults. Genetic algorithm (GA) and response surface methodology (RSM) are used for this purpose. An evaluation is made between the effectiveness of the GA-RSM PI parameters and those acquired from generalized reduced gradient (GRG) algorithm.

Nonlinear adaptive control is presented in [75] for type 4 wind generators in order to improve fault ride-though performance. Perturbation observers are developed to denote unknown real-time dynamics and external disturbances. There is no requirement for a detailed system model or parameters because it is an output feedback controller. Reachability theory is applied in [76] to enhance ride-though capability. It is used to determine sets that incorporate all possible system state trajectories arising from a disturbance. On-the-fly linearization of nonlinear systems dynamics is implemented for the computation of the reachable sets. The dynamic system is defined in (27) and the corresponding exact reachability set is given in (28). $x(t)$, $u(t)$ and $d(t)$ are system state vector, input vector and disturbance vector respectively. In this paper, reachable sets are denoted as zonotopes for computational purposes.

$$\frac{dx(t)}{dt} = F(x(t), u(t), d(t)) \tag{27}$$

$$\mathcal{R}^e(t) \triangleq \{x(t): x\ is\ a\ solution\ of\ 23\} \tag{28}$$

Predictive control is proposed in [77] for a wind generator equipped with a neutral-point clamped (NPC) converter. Desired control objectives are attained by minimizing a specific quality function. The quality function for the generator side converter g_s is defined by (29). Reference tracking is managed by the first two terms; while, the last two terms take advantage of the redundant switching states of the NPC. n_S,λ_{0S} and λ_{cS} are the number of commutation, weighting factor for voltage imbalance and weighting factor for commutation reduction terms respectively. The quality function g_G of the grid side converter is shown in (30). An MPC controller is also engaged in [78] to store surplus energy in wind turbine inertia during voltage sags. The objectives of the controller are achieved by minimisation of certain cost functions.

$$\begin{aligned} g_S = {} & (i_{sd}^*(k+2) - i_{sd}(k+2))^2 + (i_{sq}^*(k+2) - \ i_{sq(k+2))}^{\ 2} \\ & + \lambda_{0S}(v_0(k+2))^2 + \lambda_{cS}.n_S^2 \end{aligned} \tag{29}$$

$$\begin{aligned} g_G = {} & (i_{gd}^*(k+2) - i_{gd}(k+2))^2 + (i_{gq}^*(k+2) - i_{gq(k+2))}^{\ 2} \\ & + \lambda_{0G}(v_0(k+2))^2 + \lambda_{cG}.n_G^2 \end{aligned} \tag{30}$$

In [79], a grey wolf optimizer (GWO) is used to improve LVRT performance of a permanent magnet-based Type 4 wind generator. Optimal tuning is implemented for the gain factors of PI controllers using GWO, simplex method and genetic algorithm (GA) and the obtained results are compared. GWO is a meta-heuristic algorithm that mimics the social manners of grey wolves. A better LVRT response is obtained using GWO as compared to GA and simplex method during symmetrical and asymmetrical faults.

The second type of solutions for Type 4 WGs involves the alteration of traditional vector control to provide efficient ride-through performance. In [80], LVRT control based on active damping and dc-link voltage bandwidth retuning is designed as shown in Fig. 30. The active damping is primarily a band-pass filter to damp the natural frequency response of the wind generator and it is characterized by D_v in (31). V_{nom} is the nominal dc-link voltage and ω_{ad} is the natural frequency response. Equation (32) is implemented for tuning the dc-link voltage control bandwidth.

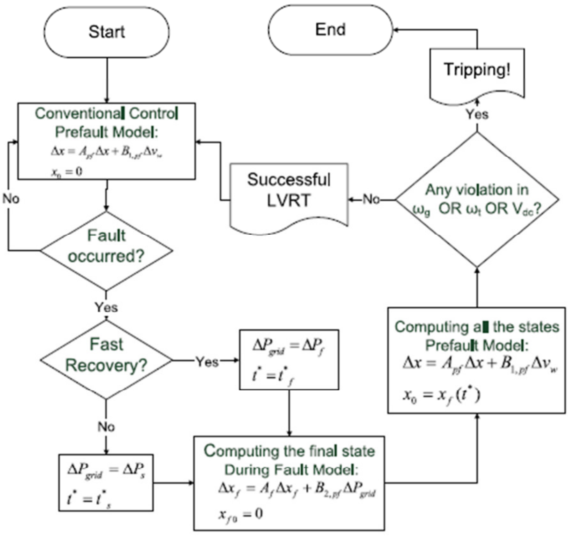

Figure 30: Retuning based LVRT control [80]

$$V_{ref}^2 = V_{nom}^2 + \frac{D_v}{\tau_{ad}s + 1} \cdot \frac{2\xi_{ad}\omega_{ad}}{s^2 + 2\xi_{ad}\omega_{ad}s + \omega_{ad}^2}\omega_g \tag{31}$$

$$f_{dc} = \frac{1}{2\pi}\sqrt{\frac{3P\lambda_m}{2}P_{nom}\omega_{r0}{}^{K_{ic}}/_{C}} \tag{32}$$

In [81], Fault-ride through improvement and grid support capabilities are presented by reorganizing traditional vector control. In traditional control, the generator-side converter controls the active power P_{grid} and stator voltage V_s, whereas the grid-side converter regulates reactive power Q_{grid} and dc-link voltage V_{dc}. In the proposed novel control strategy, the generator-side converter controls stator and dc-link voltages, while the grid-side converter regulates both active and reactive power flows. A unified dc-link current control is designed in [82] to harmonize the generator-side and grid-side converters for improved ride-through performance. Equation (33) is satisfied by the grid-side and generator-side converters. Separation of the dc-link regulator output, V_{Ldc}^*, into two quantities, V_{dcr}^* and V_{dci}^*, help in correlation of the two converters' control. V_{dcr}^* and V_{dci}^* are generator-side and grid-side converter dc-voltage references respectively. The paper also proposes reactive current injection for grid voltage stability as defined by (34). I_b and V_b are phase current and voltage respectively, whereas k is the ratio between the desired reactive current and the voltage drop magnitude.

$$V_{Ldc}^{*} = V_{dcr}^{*} - V_{dci}^{*} \tag{33}$$

$$I_{qs}^{*} = \begin{cases} kI_b(V_b - V_{ds})/V_b \\ I_b \end{cases} \tag{34}$$

In [83], a unified power control scheme is proposed where the dc-link voltage is regulated by the generator side converter; whereas the grid side converter controls the power flow between the grid and generator. Both symmetrical and asymmetrical grid voltage sags are taken into account in the investigation. An active damping loop is added in the generator-side control algorithm for damping torsional oscillations. A strategy is proposed in [84] to store additional active power in the inertia of the mechanical system of the wind turbine for efficient ride-through. A dc-link chopper circuit is also utilized for protection. Equation (35) shows the additional energy, P_G, stored in the inertia of the wind turbine in the event of a voltage dip. J is the inertial of the turbine; whereas ω_0 and ω_f are initial and final dc-link rotor speeds in that order.

$$\int P_G dt = \frac{1}{2} J\left(\omega_f^2 - \omega_0^2\right) \tag{35}$$

Only asymmetrical voltage sags are studied in [85] in which sequence decomposition is applied to develop LVRT control scheme. Three alternative schemes are investigated. The first scheme applies positive sequence voltage control with positive sequence reactive current injection and negative sequence current suppression. The second scheme is similar to the first one apart from that there is restriction of the positive sequence reactive current injection. Finally, the last scheme consists of both positive and negative sequence voltage regulation together with positive and negative sequence reactive current injection. The authors emphasize a mixed wind farm topology in [86]. The topology consists of fixed-speed (Type 1) wind generators connected in series or in parallel to Type 4 wind generators. Appropriate control scheme is developed for multilevel frequency converter to Type 4 generators.

The paper presents three different current controllers to alleviate the impact of voltage dips in [87]. The first vector current controller (VCC) is implemented in the positive sequence frame. The second controller is represented as VCCF (vector current controller feed-forward) where sequence decomposition of grid voltage is used. Here, the negative sequence grid voltage is included in the reference voltage vector directly. Lastly, the third controller, DVCC (dual vector current controller), comprises two current controllers in positive and negative synchronous reference frames.

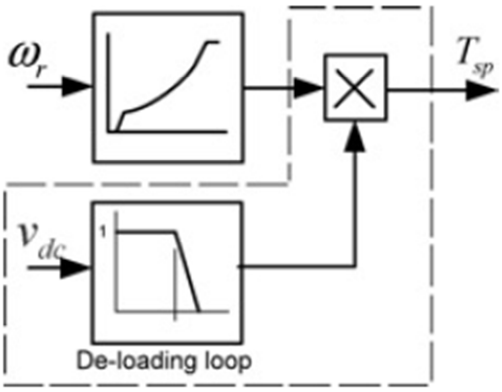

Figure 31: De-loading droop [88]

Fault ride through strategies for offshore wind farms connected to high voltage AC (HVAC) and DC (HVDC) transmission systems are defined in [88]. A de-loading method is applied for the HVAC-connected wind farm. In this strategy, the generator torque is decreased to cut down on generator power when the dc-link voltage rises. As a result, the rotor speed increases and the aerodynamic power is transformed into kinetic energy of the wind turbine. Three different strategies are investigated for the HVDC-connected wind farm: de-loading scheme, short-circuiting of the offshore HVDC converter and engaging a dc-chopper circuit. A ride-through scheme based on a new current control mechanism is proposed in [89] to deal with unbalanced grid voltage conditions. The reference currents are calculated in the positive and negative sequence as given in (36)-(39). P_{ref} is the inverter power reference and V is the voltage of the bus bar connected to the inverter. Subscripts d and q are used to represent axis of the dq reference frame, whereas the superscript n represents the negative sequence component.

$$I_{ref\_d} = \frac{2}{3} P_{ref} \frac{V_d}{\left(V_d^2 + V_q^2\right) + \left(V_d^{n2} + V_q^{n2}\right)} \tag{36}$$

$$I_{ref\_q} = \frac{2}{3} P_{ref} \frac{V_q}{\left(V_d^2 + V_q^2\right) + \left(V_d^{n2} + V_q^{n2}\right)} \tag{37}$$

$$I_{ref\_d}^n = \frac{2}{3} P_{ref} \frac{V_d^n}{\left(V_d^2 + V_q^2\right) - \left(V_d^{n2} + V_q^{n2}\right)} \tag{38}$$

$$I_{ref\_q}^{n} = \frac{2}{3} P_{ref} \frac{V_q^n}{\left(V_d^2 + V_q^2\right) - \left(V_d^{n2} + V_q^{n2}\right)} \tag{39}$$

Novel current reference generation methods are designed in [90] to limit dc-link overvoltage during unbalanced grid voltages. The q-axis current reference controls the dc-link voltage and it is calculated by comparing the dc-link voltage reference with the actual dc-link voltage. An active power limiter is also developed to restrict the peak current of the grid-side converter. The maximum limit of the active power, P_{lim}, is calculated using (40). I_{max} is the maximum current of each phase; V_{dqf}^{+} is the positive sequence PCC (point of common coupling) voltage; m is the voltage unbalance factor; k and α are power reference factor and reactive current to GSC current ratio per PCC voltage in that order. A transient management strategy is designed for voltage source converter based high voltage direct current (VSC-HVDC) connected to an offshore wind farm in [91]. Positive and negative sequence control strategies are developed for both offshore and onshore stations.

$$P_{lim} = \frac{3}{2} I_{max} \left| V_{dqf}^{+} \right| (1 - m^2) \sqrt{\frac{1}{(1+m)^2} - \frac{k^2 \alpha^2}{(1+m^2)}} \tag{40}$$

The authors present a composite control method in [92] to convert the excess energy during LVRT to kinetic energy of the rotor. A crowbar circuit is also used to prevent dc-link overvoltage. The relationship between surplus energy and rotor speed is given by (41) where ω is the rotor speed, ω_0 is the initial rotor speed, J is inertia and ΔE is excess energy during LVRT. Due to the time delay in the machine-side converter (MSC) response during a fault, the crowbar circuit is retained in this scheme. This scheme reduces the working time and the thermal amount of the crowbar circuit and also avoids continuous charging and discharging of the dc-link capacitor.

$$\Delta E = \frac{1}{2} J (\omega^2 - {\omega_0}^2) \tag{41}$$

A modified current control scheme is utilized in [93] for improved ride through performance of Type 4 wind generators. In the event of grid disturbances, active power is injected into the grid from the MSC proportional to the grid voltage drop. However, when the speed of the power reference scheme is greater than the rated speed, the active power injection is calculated based on rated speed, ω_r. A controller in the positive synchronous frame is implemented on the GSC to suppress oscillations in the dc-link, reactive and active power. Certain terms are incorporated into the controller structure for proper oscillation cancellation. The authors propose a novel converter control and active power limitation in [94] to enhance LVRT requirements during grid faults. During faults, both peak current restriction and reactive power injection are accomplished by controlling the active power generation of the Type 4 wind system with the grid-side converter (GSC). DC-link and active power oscillations are also suppressed. In the novel control structure, the machine-side converter (MSC) regulates the dc-link voltage, while the GSC implements the MPPT. A dual current controller is also implemented in the GSC to cope with asymmetrical faults. Peak currents in all phases are kept within a safe range with the help of a novel upper limiter.

The third type of solutions for Type 4 WG is based mainly on implementation of hardware for enhanced ride-through performance. A combination of Energy Storage System (ESS) and dc-link chopper is exploited in [95] for fault ride-through capability as shown in Fig. 32. The ESS is regulated using a separate converter. During grid faults, the ESS regulates the dc-link voltage in place of the grid-side converter, while the grid-side converter is implemented to supply reactive current for grid stabilization.The authors propose a dc-link chopper-based ride-through scheme for extreme voltage dips in [96]. The dc- resistor sheds any excess energy during voltage dips and it is governed by a power electronic switch. This method is also known as electromagnetic braking. In [97], the Type 4 converter is manipulated utilizing certain blocking and restart sequences to enhance ride-through capability. During a voltage sag, the generator-side converter is sidestepped but the grid-side converter keeps working to support the grid voltage. The generator-side converter is restarted and reconnected to the grid when the disturbance fades.

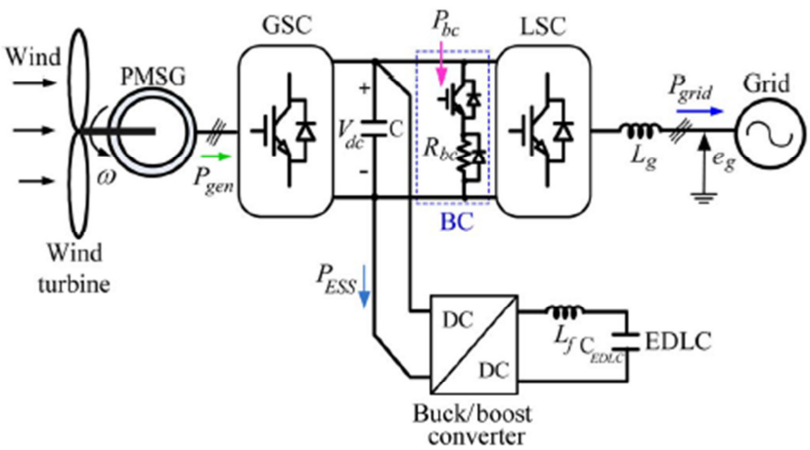

Figure 32: ESS-based control [95]

In [98], cascaded current source converters (CSCs) are implemented on the generator side and grid side. The intrinsic short-circuit operating ability is utilized to provide for fast power drop during grid faults. Reactive power support is also provided but only symmetrical voltage sags are incorporated in the scheme. It is important to note that many of the works utilized a combination of the three types of solutions for ride-through performance enhancement.In [99], a modified flux-coupling-type superconducting fault current limiter (SFCL) to improve fault ride-through capability of Type 4 wind turbine systems. The SFCL is installed between the grid-side converter and the PCC and it is composed of a coupling transformer (CT), a controlled switch (S_{cs}), a metal oxide arrester (MOA) and a superconducting coil (SC). In normal condition, the controlled switch is kept in closed state and the SC is kept at the zero resistance state. During a fault, S_{cs} opens and the MOA is utilized to protect the current transformer. The SFCL can limit the fault current and compensate for the grid voltage drop. It can also lessen the impact of dc-link overvoltage and maintain power balance by dissipating active power. In [100], a superconducting fault current limiter (SFCL) is utilized to enhance fault ride-through performance of Type 4 wind generators connected to DC microgrids. A DC microgrid removes the need for reactive power and frequency control. The SFCL is symbolised using a current controlled switch in parallel with a nonlinear resistance. The switch is normally closed which represents the superconducting state. Once the current exceeds a certain critical value, the switch is changed to the off state. A certain range of SFCL is chosen to keep the electrical power output close to its nominal value.

2.4. Summary

Grid codes of different countries regarding wind farm performance during grid voltage fluctuations are described. The expected response of wind farms to voltage sags varies from one grid code to the other. However, the German grid code, also known as the E.ON grid code, is utilized by various countries as a model to develop their own grid codes. This thesis uses the E.ON grid as a benchmark for assessment of wind farm ride-through performance. Australia is among a handful of countries which has developed specific requirements for wind farm performance under voltage swell conditions. It is important to note that these grid codes apply to all types of wind generator systems. There are presently four types of wind generator systems, namely, Type 1, Type 2, Type 3 and Type 4 wind generators. Type 3 and Type 4 are variable speed and they are more suitable for modern grids. That is why this thesis focuses on these two types of wind generators.

The literature review of ride-through strategies for Type 3 and Type 4 wind generator systems show that there are three approaches to solving the problem. The first approach involves designing advanced controllers and using them in place of or in conjunction with PI controllers to enhance ride-through performance. The second approach attempts to modify the traditional vector control strategy through various means. The most common way of modification is to generate new reference values using different algorithms. Lastly, the third approach employs hardware to counter ride-through issues. Different types of hardware have been utilized in series and shunt topology to assess their performance. An analysis of the literature review reveals that there is a dearth of a comprehensive solution which can counter the effects of both voltage sags and swells at the same time. Also, the ride-through solution should also be able to counter both symmetrical and asymmetrical type of disturbance. None of the solutions provided in the literature review attempts to deal with all facets of grid voltage fluctuation i.e., symmetrical and asymmetrical voltage sag, and symmetrical and asymmetrical swell. Furthermore, most of the ride-through solutions do not provide any reactive power support to the grid. Traditionally, wind farms were only supposed to supply active power. However, modern grid codes stipulate that wind farms need to provide reactive power support as well.

In conclusion, the current ride-through schemes are partial solutions to the problem of wind farm performance during grid voltage disturbance. Therefore, there is a need for a novel comprehensive ride-through solution which can counter all types of voltage disturbance and simultaneously support grid stability with reactive power support.

Chapter 3

Wind Generator Model

3.1. Introduction

It is of vital importance to develop an accurate model for wind farms to capture their true dynamics during grid fluctuations. Relatively detailed models of the Type 3 and Type 4 wind generator systems are presented and described in this chapter. The main issue of modelling is between fast simulations versus model accuracy. A model which provides simulation results very quickly can often be too simplistic and inaccurate, whereas, an overly detailed model can lead to unnecessary long simulation time. Therefore, Type 3 and Type 4 wind system models are presented in this chapter which provide sufficient accuracy within a reasonable time.

The chapter begins by explaining the aerodynamic model of a wind generator and then gives the equations for the mechanical system and electrical systems. Thereafter, the function of the power electronic converters implemented is explained. The control architecture based on traditional vector control are described and the detailed control architecture is discussed.

3.2. Overview of Type 3 and Type 4 wind power systems

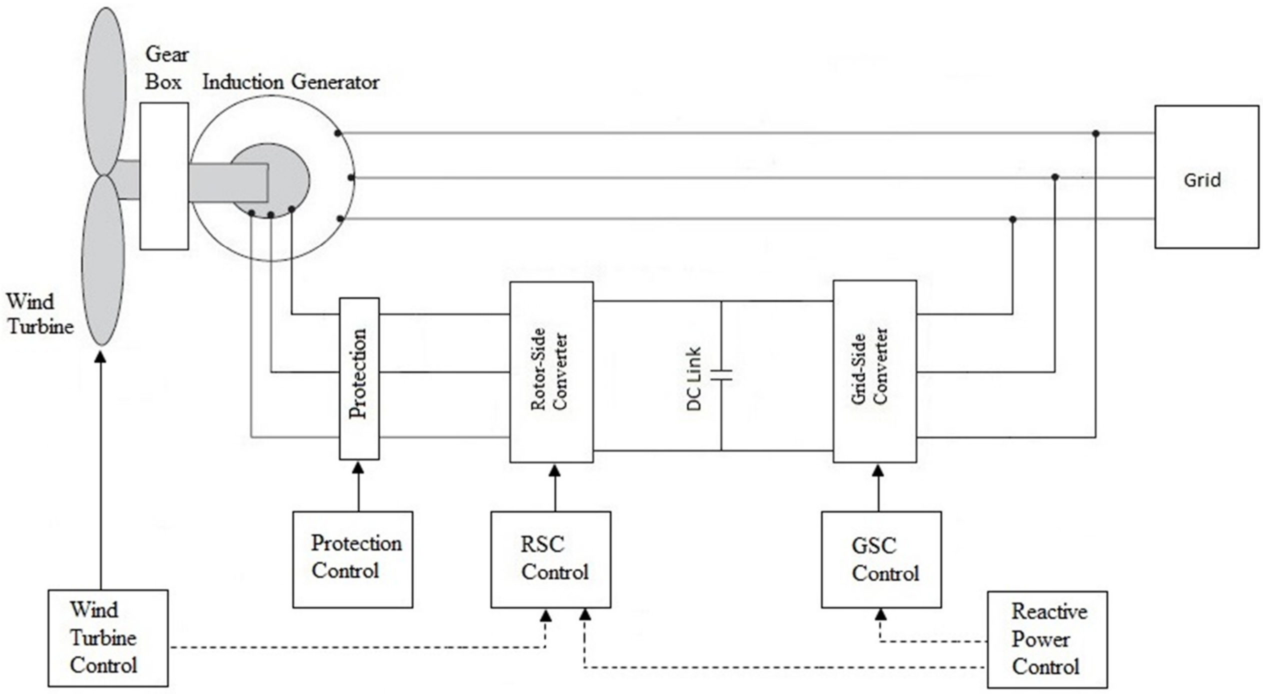

Figure 33: Type 3 wind generator configuration

Type 3 wind power systems comprise of Doubly-Fed Induction Generators (DFIG) as shown in Fig. 33. The stator of a DFIG is connected to the grid directly, while the rotor is connected to the partial-scale frequency converter. The partial scale converter is also known as a back-to-back converter consisting of the Rotor Side Converter (RSC) and the Grid Side Converter (GSC). Only 30% of the power generated is managed by the converter, while the speed range varies between -40% to +30% of synchronous speed. There is a dc-link capacitor in between which acts as an energy buffer between the RSC and the GSC. IGBT (Insulated gate bipolar transistor)/Diode based pulse width modulation is implemented in the converters. The wind turbine is connected to the generator via a gear box containing the drive train. The DFIG control architecture has three levels, namely, levels 1, 2 and 3 where level 1 is the lowest level of control and level 3 representing the highest level. The control of the RSC and GSC is relegated to level 1, level 2 deals with Maximum Power Point Tracking (MPPT) and pitch angle regulation, supervisory control for smooth grid integration and grid support is performed by level 3 control. A resistive-inductive filter is placed between the converter and grid to eliminate unwanted frequencies.

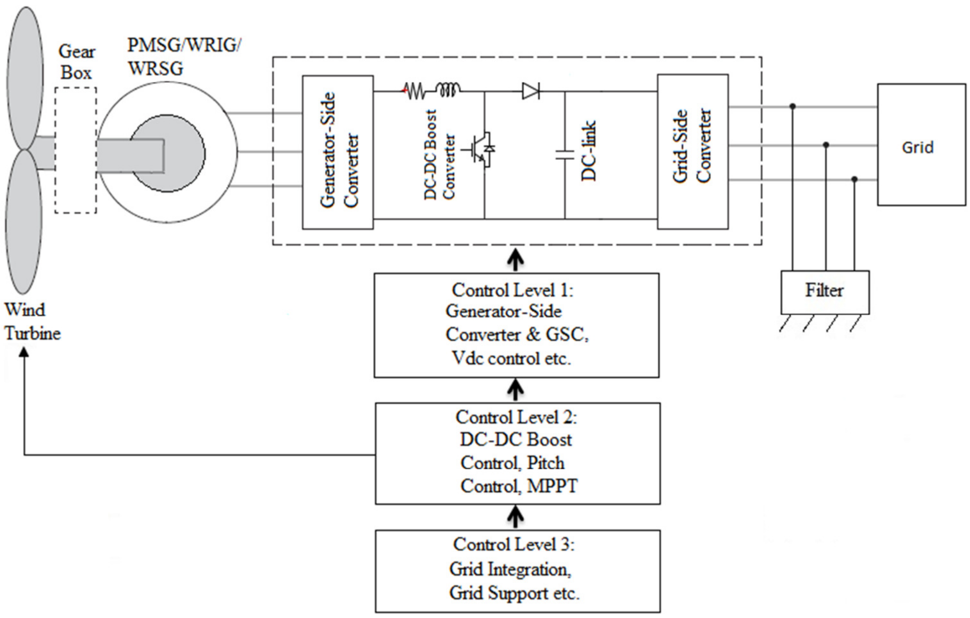

Figure 34: Type 4 wind generator configuration

Type 4 wind power systems as shown in Fig. 34 can consist of any one of the three types of generators: permanent-magnet synchronous generator (PMSG), wound-rotor induction generator (WRIG) or wound-rotor synchronous generator (WRSG). Regardless of the type of generator used, the stator of the Type 4 wind generator is connected to the full-scale converter which, in turn, is connected to the grid. Unlike Type 3 wind generators, the Type 4 converter handles 100% of the wind power generated. There is a dc-dc boost converter after the generator side converter to raise the dc voltage level. The dc-link capacitor acts as a buffer before injecting the power to the grid side converter (GSC). The generator side converter is uncontrollable implementing only diode-based switching, while IGBT/Diode based pulse width modulation is used in the grid side converter. The Type 4 wind generator control architecture also comprises three levels similar to those of Type 3 wind generators. The control of the generator side converter and GSC is relegated to level 1, level 2 deals with Maximum Power Point Tracking (MPPT), pitch control and dc-dc boost converter control; grid integration and grid support are achieved by level 3 control. A resistive-inductive filter eliminates unwanted frequencies coming from the full-scale converter. The wind turbine is connected to the generator via a gear box. However, some Type 4 wind generators have direct drive orientation without any gearbox.

3.3. Wind power and aerodynamic model

The amount of power present in wind is given in (42) where ρ is air density, A is the cross-sectional area of wind and V is the wind speed. However, the wind turbine rotor cannot extract all the power from wind. The amount of power that can be extracted is given in (43). C_p is known as the power coefficient and its value depends on the tip-speed ratio, λ, and the pitch angle/blade angle, β. The maximum value of the power coefficient is 0.59 which is known as the Betz constant. The relationship in (44) between C_p and, λ and β, is highly nonlinear and is often provided by the wind generator manufacturer, given in Fig. 35. The equation for tip-speed ratio is given in (45) where R is the radius of the wind turbine and ω_t is the mechanical rotor speed.

$$P_{wind} = \frac{1}{2}\rho A v^3 \tag{42}$$

$$P_{extracted} = C_p \times P_{wind} \tag{43}$$

$$\mathrm{C_p} = 0.6450*(0.00912*\lambda + (-5 - 0.4*(2.5 +\theta) + 116*(1/(\lambda + 0.08*(2.5 + \theta)) - 0.035/(1 + (2.5 +\theta)\verb|^|3)))/\exp(21*(1/(\lambda + 0.08*(2.5 + \theta)) - 0.035/(1 + (2.5 + \theta)\verb|^|3))) \tag{44}$$

$$\lambda = \frac{\omega_t r}{v} \tag{45}$$

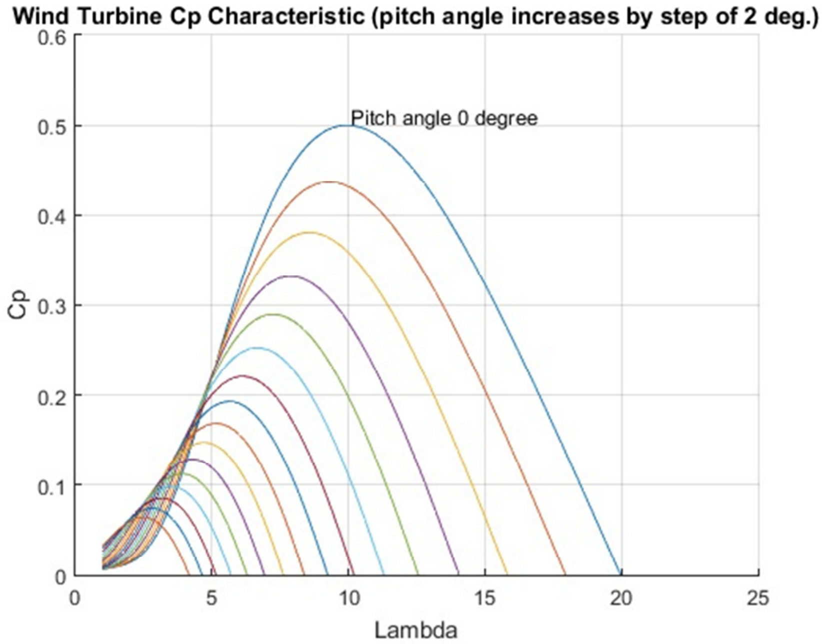

Figure 35: C_p characteristics

There are four different ways for modelling the aerodynamic system of a wind turbine. They are the blade element method, $C_p(\lambda, \beta)$ lookup table, analytical approximation and the wind speed-mechanical power lookup table. The blade element method divides the turbine blade into different cross-sections where only two main forces act. The forces are lift and drag forces. However, this method requires fast computation capability. Moreover, the mechanical torque cannot be found from the known mechanical power when the rotational speed is zero. The $C_p(\lambda, \beta)$ lookup table can overcome this problem. It is also possible to approximate $C_p(\lambda, \beta)$ dynamics utilizing non-linear functions as used in (42). Lastly, the relationship between wind speed and mechanical power can be converted into a 2-dimensional lookup table. This method is appropriate for long-term power system stability studies [89].

3.4. Mechanical system of Type 3 and Type 4 wind generators

A wind turbine is exposed to various dynamics like 3p effect, tower vibration effects and torsional dynamics. These dynamics have the capability to affect the generators electrical response. However, only torsional dynamics have any significant influence on power system stability studies. A two-mass model, as shown in Fig. 34, of the mechanical system is derived in this thesis for both Type 3 and Type 4 wind turbine generators. This model is sufficient for power system analysis [101]. The mechanical system can also be represented as a three-mass or one-mass model. Whereas, the three-mass model provides too many details which are unnecessary for this thesis, the one-mass model is overly simplified.

The two-mass model comprises two inertias: the turbine inertia (H_t) and the generator inertia (H_g). The turbine inertia consists of inertias of the turbine, part of gearbox and low-speed shaft; while, the generator inertia includes the mass of the rotor, part of gearbox and high-speed shaft. The two inertias are connected by a shaft which has stiffness coefficient K_s. T_t and ω_t are mechanical torque and speed respectively; whereas, T_e and ω_r represent electrical torque and speed correspondingly. There are three damping coefficients in Fig. 36, namely, turbine damping coefficient, D_t, generator damping coefficient, D_g, and mutual damping, D_m. D_t represents the aerodynamic resistance in the turbine blade, D_m characterises mechanical friction and windage; finally, D_m is the effect of the difference in speed between the generator rotor and turbine shaft [102]. Equations (46)-(49) describe the mechanical system of the wind generators.

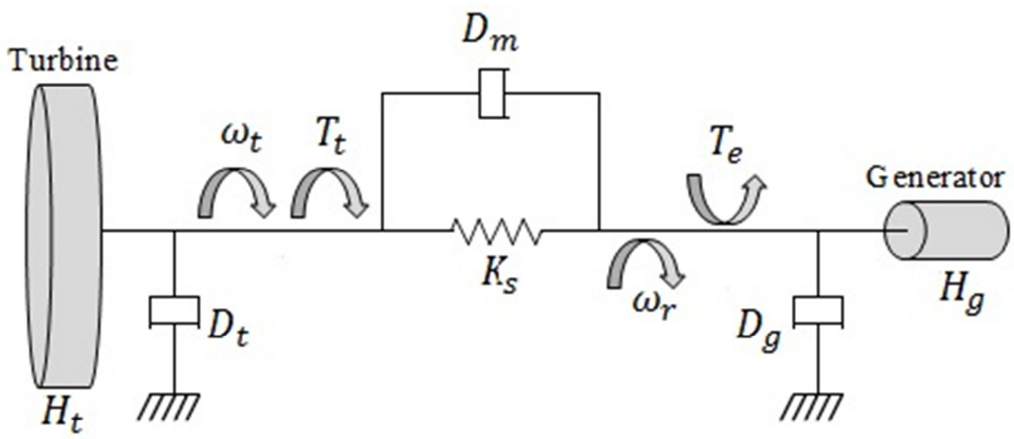

Figure 36: Wind generator mechanical system

$$2H_t\frac{d\omega_t}{dt} = T_t - K_s(\theta_r - \theta_t) - D_m(\omega_r - \omega_t) \tag{46}$$

$$2H_g\frac{d\omega_r}{dt} = -T_e + K_s(\theta_r - \theta_t) + D_m(\omega_r - \omega_t) \tag{47}$$

$$\frac{d\theta_t}{dt} = \omega_t \tag{48}$$

$$\frac{d\theta_r}{dt} = \omega_r \tag{49}$$

3.5. Wind generator electrical systems

3.5.1. Reference frame

The dq 2-axis theory is used for modelling the wind generators. There are three preferable reference frames that can be implemented. They are the stationary reference frame, the synchronously rotating reference frame and the rotor reference frame. As the name suggests, d-q axes do not rotate in the stationary reference frame, while they rotate at synchronous speed in the synchronous reference frame. The d-q axes rotating speed is the same as the rotor speed in the rotor reference frame and this reference frame is chosen in this thesis. In the rotor reference frame, the d-axis position coincides with phase A quantities of the rotor. The advantage of this is the d-axis rotor current behaves the same as the phase A rotor current. Hence, there is no need to calculate phase A rotor current at every step through invert Park's transformation. As a result, a lot of computation time is saved [103].

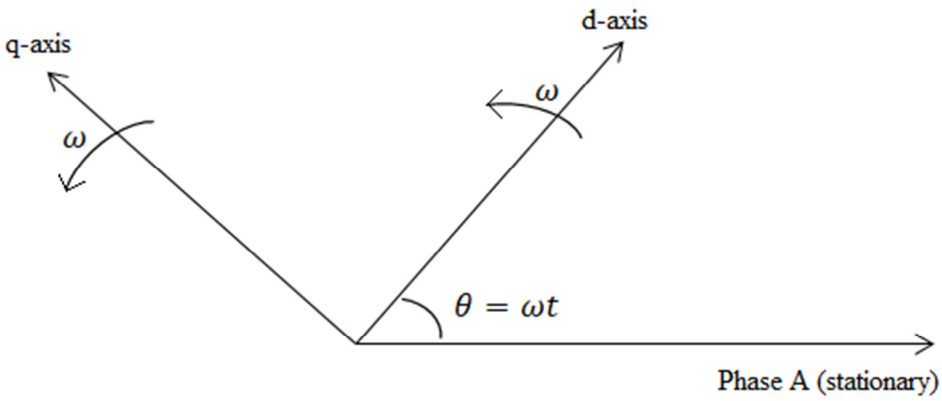

Figure 37: The dq reference frame

The transformation of variables from the ABC frame to the dq frame is performed with an arbitrary speed ω which is the angle of rotation of the dq frame. The arbitrary speed ω is related to θ as shown in (48). Trigonometric functions are derived from the orthogonal projections of ABC variables (x_A, x_B and x_C) to the corresponding dq-axis variables (x_d and x_q). In Fig. 37, it is seen that the d-axis is aligned with phase A at $t = 0$ and it starts rotating with speed ω when $t = 0^{+}$. The q-axis always remains 90° ahead of the d-axis. The exact relationships between the ABC and dq-axis variables are given in (50) - (52) [102].

$$\frac{d\theta}{dt} = \omega \tag{50}$$

$$x_d = \frac{2}{3}\left(x_A \cos\theta + x_B \cos\left(\theta - \frac{2\pi}{3}\right) + x_C \cos\left(\theta - \frac{4\pi}{3}\right)\right) \tag{51}$$

$$x_q = -\frac{2}{3}\left(x_A \sin\theta + x_B \sin\left(\theta - \frac{2\pi}{3}\right) + x_C \sin\left(\theta - \frac{4\pi}{3}\right)\right) \tag{52}$$

3.5.2. Type 3 (DFIG) wind generator electrical system

Equations (53)-(56) describe the electrical system of the DFIG wind generator in the rotor d-q reference frame. V_{ds} and V_{qs} are d and q components of stator voltage respectively, whereas V_{dr} and V_{qr} are d and q components of rotor voltage. The subscript ‘s’ symbolizes stator and ‘r’ symbolizes rotor, while ‘d’ and ‘q’ denote d-axis and q-axis components in that order. *R* and *I* stand for resistance and current respectively; ω and ψ mean speed and flux in that order. T_e represents the electrical torque and *p* is the number of poles. Equation (57) links the electrical system to the mechanical system of the wind generator. Fig. 38 presents the equivalent circuit of the induction generator. The flux linkage equations for the stator and rotor sides are given in (58)-(63) where L_{lr}, L_{ls} and L_m mean leakage rotor inductance, leakage stator inductance and magnetizing inductance in that order.

$$V_{ds} = R_s I_{ds} + \frac{d\psi_{ds}}{dt} + \omega_r \psi_{qs} \tag{53}$$

$$V_{qs} = R_s I_{qs} + \frac{d\psi_{qs}}{dt} - \omega_r \psi_{ds} \tag{54}$$

$$V_{dr} = R_r I_{dr} + \frac{d\psi_{dr}}{dt} \tag{55}$$

$$V_{qr} = R_r I_{qr} + \frac{d\psi_{qr}}{dt} \tag{56}$$

$$T_e = \frac{3}{2} p(\psi_{ds} I_{qs} - \psi_{qs} I_{ds}) \tag{57}$$

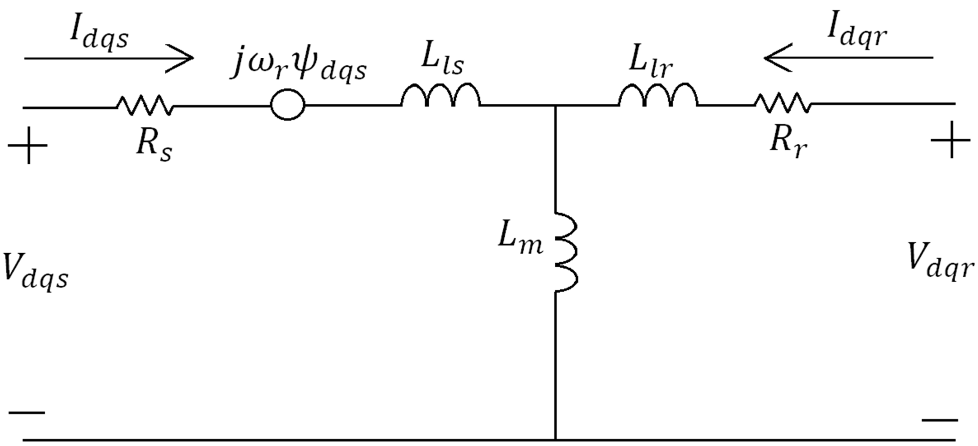

Figure 38: DFIG electrical system equivalent circuit

$$\psi_{ds} = L_s I_{ds} + L_m I_{dr} \tag{58}$$

$$\psi_{qs} = L_s I_{qs} + L_m I_{qr} \tag{59}$$

$$\psi_{dr} = L_r I_{dr} + L_m I_{ds} \tag{60}$$

$$\psi_{qr} = L_r I_{qr} + L_m I_{qs} \tag{61}$$

$$L_s = L_{ls} + L_m \tag{62}$$

$$L_r = L_{lr} + L_m \tag{63}$$

3.5.3. Type 4 synchronous generator electrical system

The electrical system of the Type 4 wind generator is presented in (64)-(69) in the rotor d-q reference frame. The subscripts 'd', 'q', 's', 'f' and 'k' symbolize d-axis, q-axis, stator, field and damping components respectively. *V, I, R* and ψ symbolise voltage, current, resistance and flux correspondingly. The electromagnetic torque that connects the electrical system to the mechanical system is given in (70). The flux linkage equations of the generators are given in (72)-(77). Figures (39) and (40) show the equivalent circuit of the Type 4 wind generator in the d- and q-axis separately. The rotor dq reference frame is utilized.

$$V_{ds} = R_s I_{ds} + \frac{d\psi_{ds}}{dt} - \omega_r \psi_{qs} \tag{64}$$

$$V_{qs} = R_s I_{qs} + \frac{d\psi_{qs}}{dt} + \omega_r \psi_{ds} \tag{65}$$

$$V_{fd} = R_{fd} I_{fd} + \frac{d\psi_{fd}}{dt} \tag{66}$$

$$V_{kd} = R_{kd} I_{kd} + \frac{d\psi_{kd}}{dt} \tag{67}$$

$$V_{kq1} = R_{kq1} I_{kq1} + \frac{d\psi_{kq1}}{dt} \tag{68}$$

$$V_{kq2} = R_{kq2} I_{kq2} + \frac{d\psi_{kq2}}{dt} \tag{69}$$

$$T_e = \psi_{ds} I_{qs} - \psi_{qs} I_{ds} \tag{70}$$

$$T_e = \psi_{ds} I_{qs} - \psi_{qs} I_{ds} \tag{71}$$

$$\psi_{ds} = L_d I_{ds} + L_{md}\left(I_{fd} + I_{kd}\right) \tag{72}$$

$$\psi_{qs} = L_q I_{qs} + L_{mq} I_{kq} \tag{73}$$

$$\psi_{fd} = L_{fd} I_{fd} + L_{md}(I_{ds} + I_{kd}) \tag{74}$$

$$\psi_{kd} = L_{kd} I_{kd} + L_{md}\left(I_{ds} + I_{fd}\right) \tag{75}$$

$$\psi_{kq1} = L_{kq1} I_{kq1} + L_{mq} I_{qs} \tag{76}$$

$$\psi_{kq2} = L_{kq2} I_{kq2} + L_{mq} I_{qs} \tag{77}$$

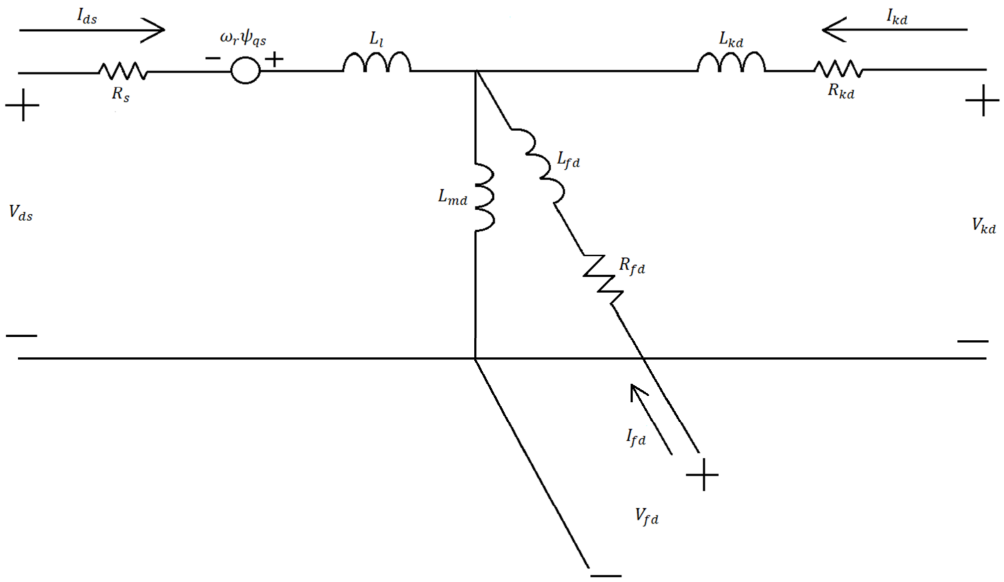

Figure 39: Type 4 generator d-axis equivalent circuit

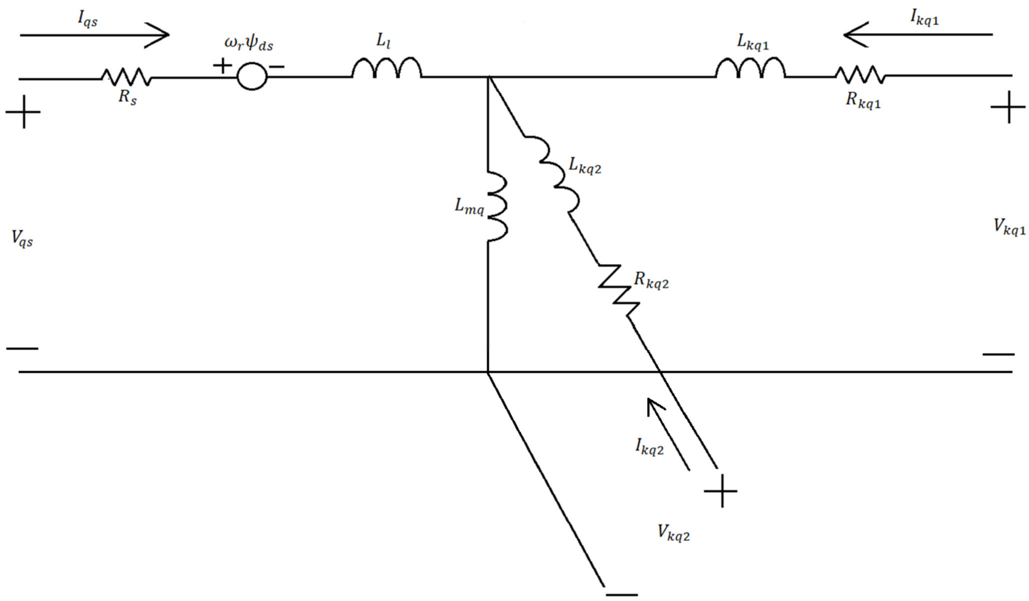

Figure 40: Type 4 generator q-axis equivalent circuit

3.6. Wind generator converters

3.6.1. Type 3 converter and grid filter

Power electronic converters enable variable speed operation of wind generators by adjusting the generator frequency to the grid frequency. The controllability of generator frequency has many added advantages [104]:

- Optimal energy capture from wind at various wind speeds
- Wind speed changes are absorbed by rotor speed variations thereby reducing stress on the gear and drive-train
- Prevention of life-consuming loads by load regulation
- Converters can act as an electrical gearbox thereby facilitating the use of gearless wind turbine systems
- Reduction in noise emission at low wind speeds

Power electronic converters also have a positive impact on power system dynamics. Wind farms become active contributors in power system dynamics:

- Both active and reactive power of a wind farm can be regulated
- In weak grids, wind farms act as a local reactive power source
- Network stability is enhanced
- Power quality is improved by reducing flicker

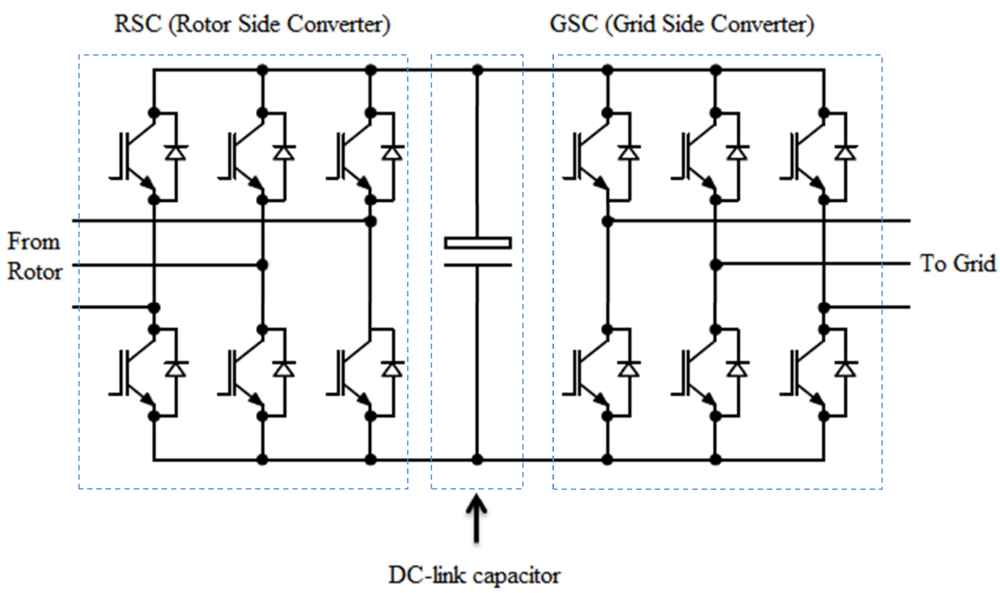

Figure 41: DFIG wind generator back-to-back power converter

The rotor of the DFIG is connected to the RSC, while the GSC is connected to the grid. There is an energy storage known as the dc-link capacitor. It is placed between the RSC and GSC which is always kept at a steady voltage (typically 1150 V). The dc-link capacitor decouples the operation of the RSC and GSC thereby compensating any power asymmetry on both sides. This converter orientation is also called the Scherbius scheme which allows for di-directional flow of active power [102]. The RSC regulates the flow of stator active (P_s) and reactive power (Q_s), whereas the purpose of the GSC is to maintain the dc-link capacitor voltage and the flow of reactive power from converter to the grid. The modelling of the RSC and GSC are done as voltage sources where the current is controllable. Each converter has six IGBT-Diodes connected in a universal bridge configuration and the switching is regulated utilizing Pulse-Width Modulation (PWM). The characteristic frequency of range of the IGBT is between 2 and 20 KHz. The dynamics of converter switching is disregarded because the system frequency is much lower than the PWM frequency.

The characteristic of the dc-link capacitor is shown in (78). C and V_c are the capacitance and the voltage of the dc-link capacitor correspondingly. P_f is the power transferred to the grid filter and P_r is the rotor active power. It is also assumed there is no loss power in the converter. The GSC is connected to the grid via a resistive-inductive (RL) filter. The filter dynamics is provided in (79). V_f and V_g are filter voltage and grid voltage correspondingly. I_f is the filter current; while, R_f and L_f are the filter resistance and inductance respectively. An equivalent circuit of the resistive-inductive (RL) filter is given in Fig. 42.

$$CV_c \frac{dV_c}{dt} = P_f - P_r \tag{78}$$

$$L_f \frac{dI_f}{dt} = V_f - \left(R_f + j\omega_s L_f\right) I_f - V_g \tag{79}$$

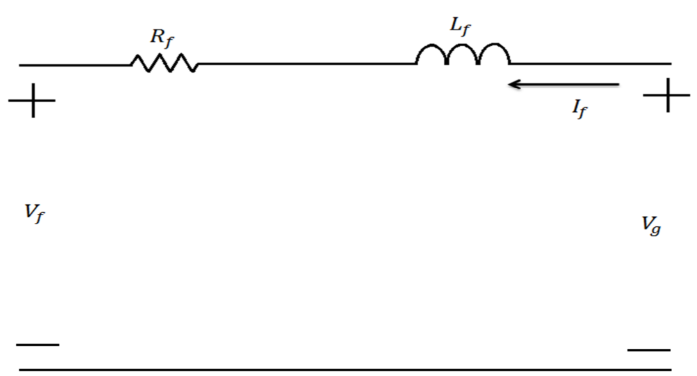

Figure 42: RL filter equivalent circuit

3.6.2. Type 4 full-scale converter

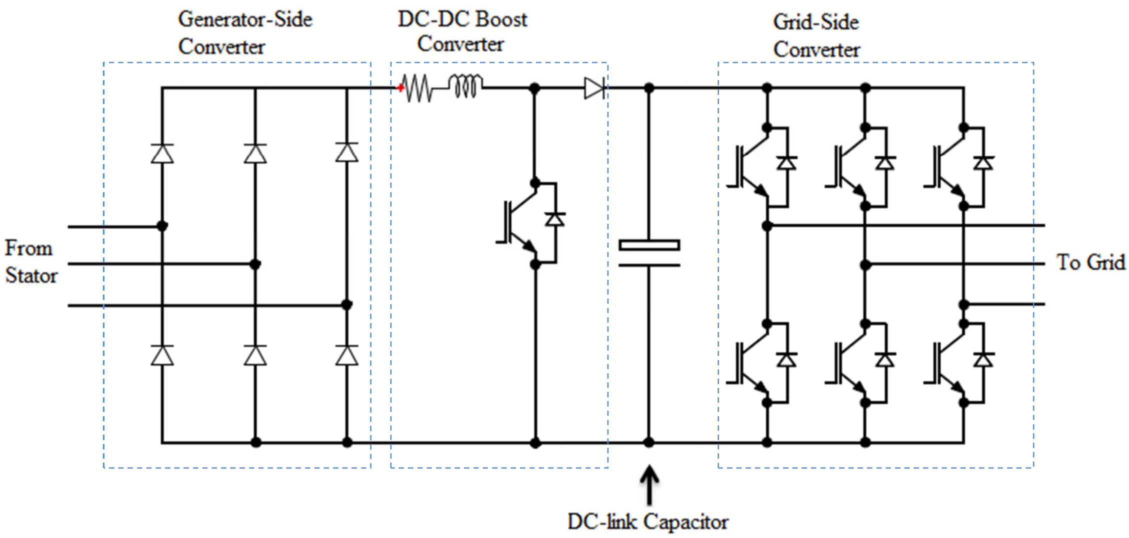

Figure 43: Type 4 full-scale converter

The full-scale converter of the Type 4 wind generator consists of a generator-side converter (diode-bridge rectifier), DC-DC boost converter, dc-link capacitor and grid-side converter (IGBT-Diode bridge). The rectifier is directly connected to the stator of the wind generator and it is not controllable. This brings down the cost of the overall system. It is also called the generator-side converter. The grid-side converter is regulated by implementing PWM switching. There is a DC-DC boost converter between the generator-side converter and the grid-side converter, and it is controlled using an IGBT switch. The dc-link voltage is maintained at a constant value (typically 1100 V) [105]. Two important functions of the frequency converter are smooth grid integration of the wind generator and reactive power compensation during grid disturbances. Compared to DFIG configuration, the Type 4 configuration allows for easier construction and more efficiency. The grid-side converter is connected to a resistive-inductive filter (RL) similar to the DFIGs.

3.7. DFIG control

There are three popular control methodologies for DFIG wind turbine systems. They are direct torque control (DTC), direct power control (DPC) and vector control (VC) [106]. A brief discussion of each of the approaches is given in the following sections.

3.7.1. Direct torque control (DTC)

Power electronic converters can impose a defined voltage into the machine circuit very quickly. DTC takes advantage of this functionality. The stator flux, ψ_s, is imposed by the grid voltage while the rotor flux is regulated by the RSC. Both the magnitude and angle of the rotor flux can be controlled. So, the torque, T_e, of the DFIG are established by regulating the angle, γ, between ψ_s and ψ_r, whereas the regulation of active and reactive power depends on the rotor flux magnitude, $|\psi_r|$. The entire DTC scheme depends on the accurate estimation of the instantaneous values of T_e and ψ_r. Equation (80) is utilized to calculate ψ_r, while (81) gives us T_e [106].

$$|\psi_r| = \sqrt{{\psi_{dr}}^2 + {\psi_{qr}}^2};\ \angle\psi_r = \tan^{-1}\frac{\psi_{qr}}{\psi_{dr}} \tag{80}$$

$$T_e = 3L_m(I_{qs}I_{dr} - I_{ds}I_{qr})/2 \tag{81}$$

3.7.2. Direct power control (DPC)

The DPC scheme is very similar to that of DTC. However, while DTC controls T_e and ψ_r, DPC regulated the *effect* the magnitudes have on active and reactive power. Although this is a subtle difference but it makes the DPC scheme more robust and easier to implement. The advantages of DPC are given below [106].

- No need to incorporate machine parameters in the scheme
- Measurement of just a few electrical magnitudes required for implementation
- Avoidance of reference frame transformation

The instantaneous active and reactive powers are calculated in the stationary $\alpha\beta$ reference frame according to (82) – (83).

$$P_s = \frac{3}{2}\left(V_{\beta s}I_{\beta s} + V_{\alpha s}I_{\alpha s}\right) \tag{82}$$

$$Q_s = \frac{3}{2}\left(V_{\beta s}I_{\alpha s} - V_{\alpha s}I_{\beta s}\right) \tag{83}$$

3.7.3. Vector control

Vector control has been implemented in this thesis as it is the most common of the three methodologies. The stator resistance, R_s, is neglected and stator voltage, V_s, is assumed to be constant and imposed by grid voltage, V_g. Equations (51) – (52) are simplified by aligning the stator voltage, V_s, with the direct axis of the rotating dq reference frame as shown in (84) –

(85). This makes the quadrature axis stator voltage equal to zero. This is called stator-voltage orientation vector control.

$$V_{ds} = V_s \tag{84}$$

$$V_{qs} = 0 \tag{85}$$

3.7.3.1. RSC control scheme

The RSC and GSC are regulated independently. The RSC control scheme is shown in Fig. 44. The RSC consists of two inner-loop current controllers regulating direct and quadrature axis currents, while the outer-loop contains a speed controller and a stator reactive power controller. The main function of the speed controller is to extract the maximum amount of energy from wind as long as the total power generated, P_T, is under 0.75 p.u which is the partial load region. This is performed by calculating the appropriate electromagnetic torque reference, T_e, going into the d-axis current controller. The relationship between the rotor speed and electromagnetic torque is given in (83) where K_{Cp} is a variable that depends on the wind turbine geometry. A constant rotor speed reference, ω_{ref}, of 1.2 pu is maintained when the power generated exceeds the value of 0.75 pu which is known as the full load region. In this region, the main purpose of the speed controller is to keep extracting the maximum energy from wind by involving pitch angle control ($\beta°$). The Maximum Power Point Tracking (MPPT) algorithm is presented in (86) - (88) [102].

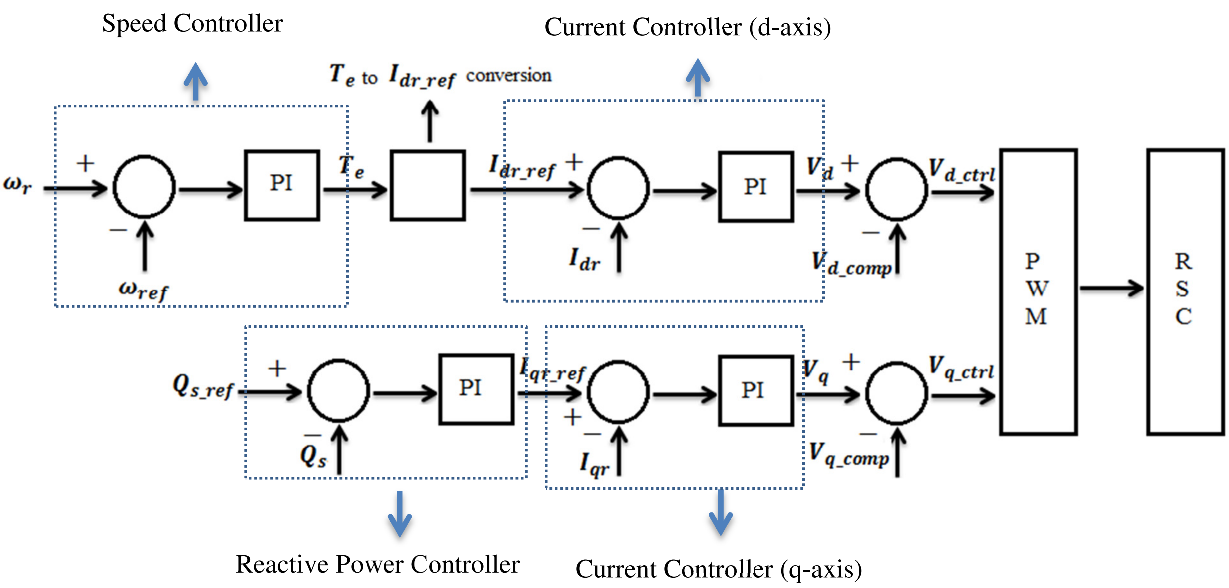

Figure 44: RSC control scheme

$$T_e = K_{Cp}\omega_r{}^2 \tag{86}$$

$$\omega_{ref} = -0.67P^2 + 1.42P + 0.51, when\ P_T < 0.75 \tag{87}$$

$$\omega_{ref} = 1.2, when\ P_T \gg 0.75 \tag{88}$$

The speed controller reference is also fed into a pitch angle controller shown in Fig. 45. While, the speed controller tries to maintain an optimal tip-speed ratio, λ, utilizing (43), the function of the pitch controller is to vary the pitch angle, $\beta°$, for maximum energy extraction. The wind turbine blade is regulated to either turn out or into the wind according to requirement. Jointly, they maintain an optimum value of the power coefficient (C_p). It has been stated earlier in the thesis that C_p is a function of λ and $\beta°$. The actuator used for pitch angle variation is a hydraulic servomotor. This is usually modelled as a first-order lag system as in (89) where T is the time lag of the actuator and β_{com} is the command signal from the pitch controller [107]. The rate limited decides how quickly mechanical power can be reduced to avoid the generator rotor from over-speeding.

$$\beta° = \frac{1}{1 + Ts}\beta_{com} \tag{89}$$

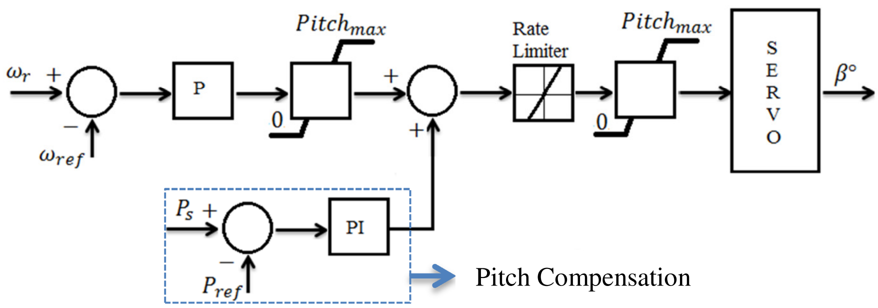

Figure 45: Pitch angle control scheme

The reactive power controller of the RSC controls the stator reactive power. Its output generates the reference value of the q-axis current controller. The d-axis current controller obtains its reference from the speed controller. The two current controllers are decoupled using voltage compensation terms V_{d_comp} and V_{q_comp}.

3.7.3.2. GSC control scheme

The control scheme for the GSC is shown in Fig. 46. It includes one outer loop controller for the regulation of the dc-link capacitor voltage. Its output is fed into the d-axis current controller (grid-side). The q-axis current controller (grid-side) reference is usually kept at zero to allow for DFIG operation at unity power factor. However, this can be changed to provide reactive power support to the grid during voltage disturbances. The current controller can be coupled with a higher level supervisory controller to support the grid by controlling the flow of reactive power between the grid and the GSC. This is demonstrated at a later chapter.

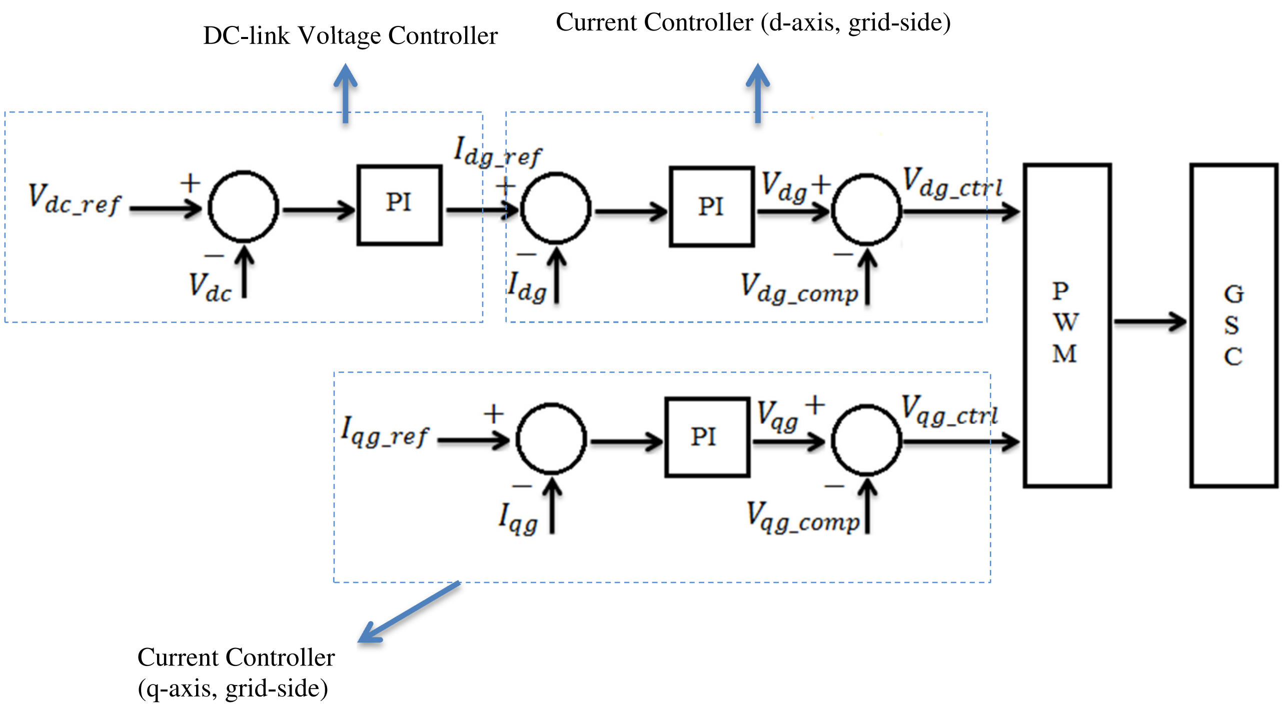

Figure 46: GSC control strategy

3.7.3.3. Type 3 wind generator operating modes

There are two modes of operation for Type 3 wind generators: sub-synchronous and super-synchronous operations. In the sub-synchronous mode, the rotor speed is lower than the electrical synchronous speed which makes the slip positive. In this mode, active power flows from the grid to rotor as shown in Fig. 47. Whereas, the rotor speed is higher in the super-synchronous mode i.e., the slip is negative and active power flows from the rotor to grid as in Fig. 48. It must be noted that the flow from the stator is uni-directional i.e., from stator to grid, in both modes. Considering no power loss in the converter, the total electrical power transferred to the grid is the sum of the rotor power and stator power [101].

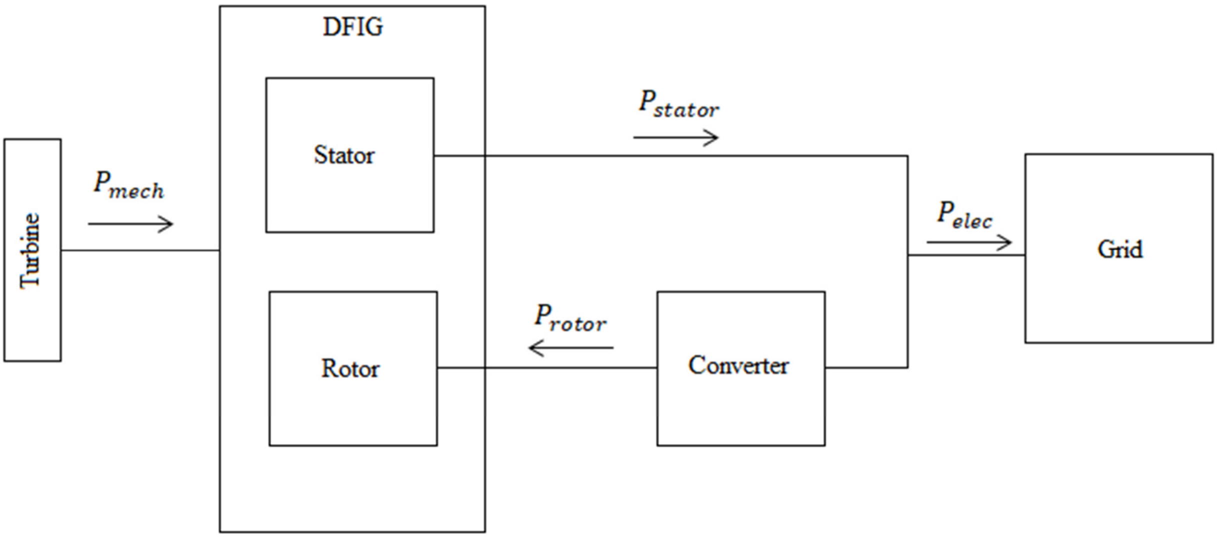

Figure 47: Type 3 WG sub-synchronous operation

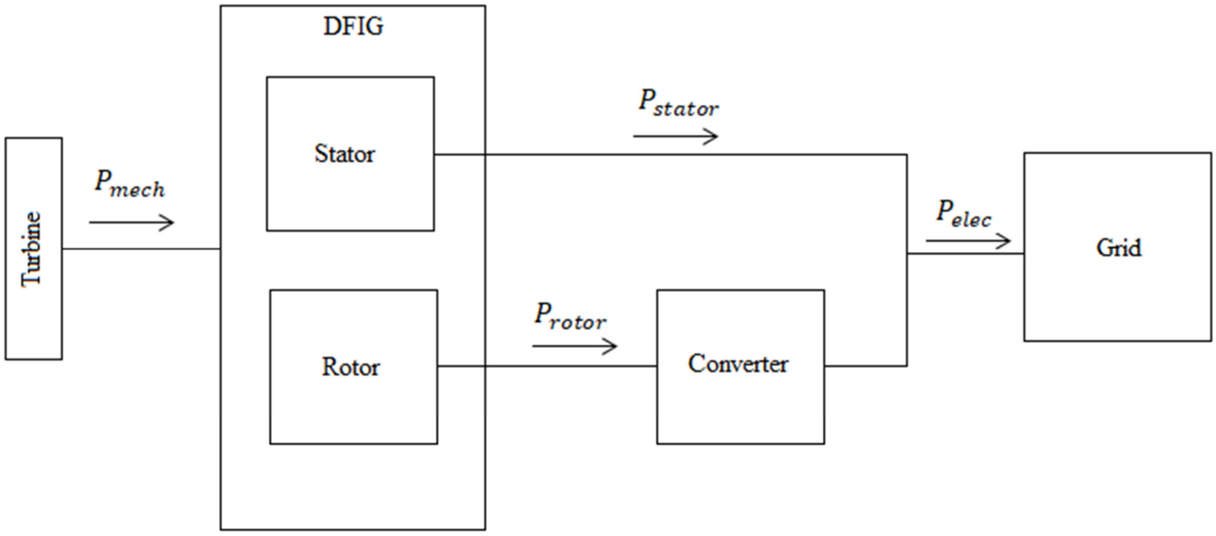

Figure 48: Type 3 WG super-synchronous operation

3.8. Type 4 wind generator control

The control hierarchy of the Type 4 WG wind generator presented in Fig. 32 is similar to that of the Type 3 WG. However, the most notable difference is that the generator-side converter is not controlled. It is a passive diode-bridge rectifier. This reduces the overall cost of the system.

In Fig. 49, the control scheme of the booster converter is shown. There is an outer loop speed controller linked to an inner loop current controller. The function of the current controller is to boost up the rectified voltage. This is performed by regulating the duty cycle of the pulse generator. An interconnected pitch controller is fed to the rotor speed reference from speed controller. The control scheme of the pitch controller is the same as that of the Type 3 WG configuration. The dc excitation system is shown in Fig. 50 which generates electromagnetic flux in the rotor windings of the synchronous generator.

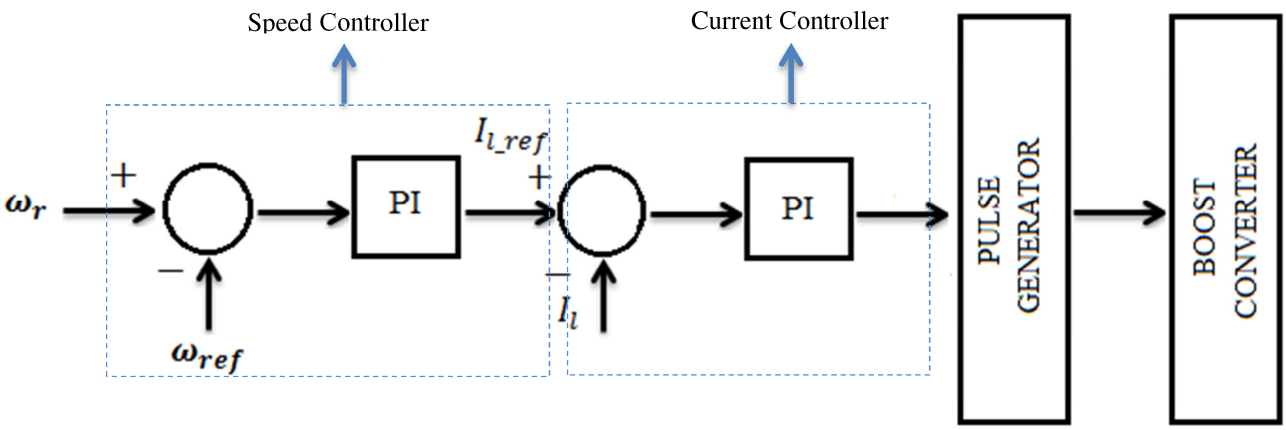

Figure 49: Boost converter control strategy

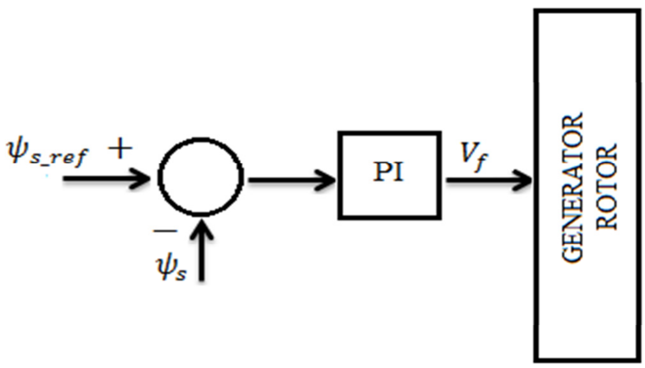

Figure 50: DC excitation control

The control scheme of the grid-side converter is shown in Fig. 51. It comprises two outer loop voltage and reactive power controllers connected to two inner loop current controllers. The voltage controller keeps the dc-link voltage at a constant value of 1100 V, while the reactive power controller regulates the flow of reactive power between the grid and the grid-side converter. Similar to the Type 3 WG configuration, the reactive power controller can be coupled with a higher level supervisory controller to support the grid by either injecting or absorbing reactive power.

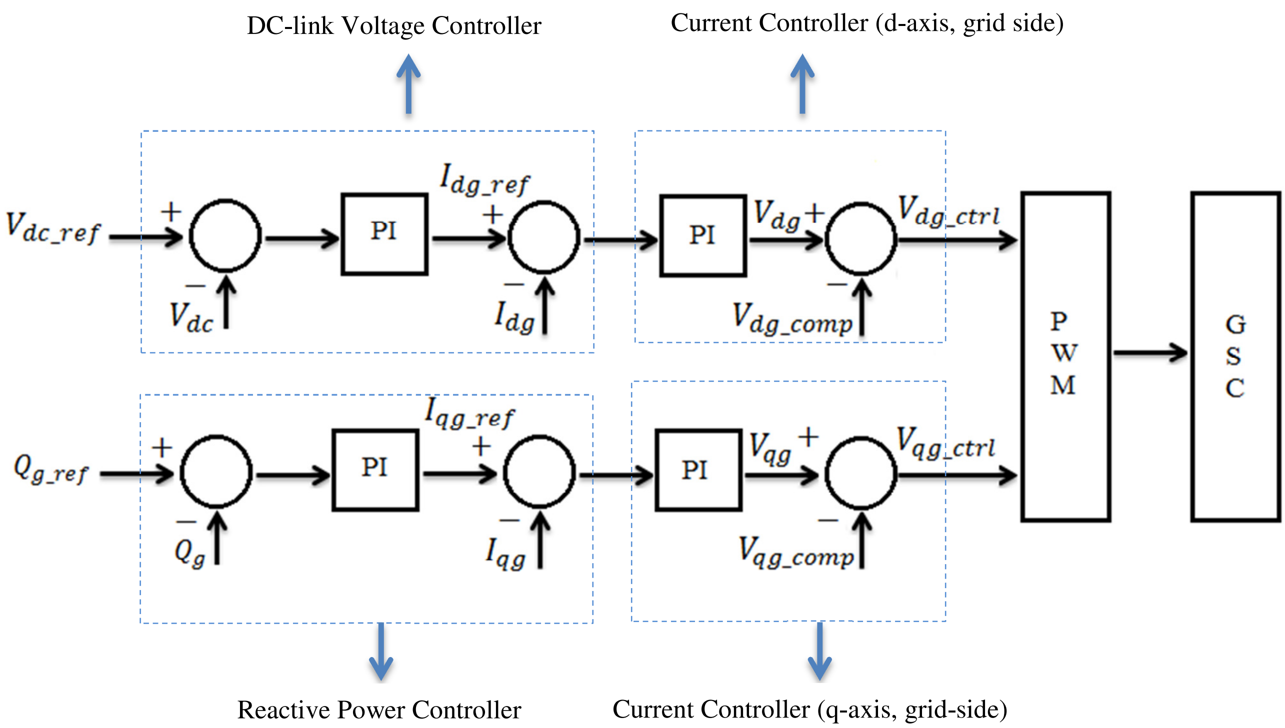

Figure 51: Grid-side converter control strategy

3.9. Operating regions

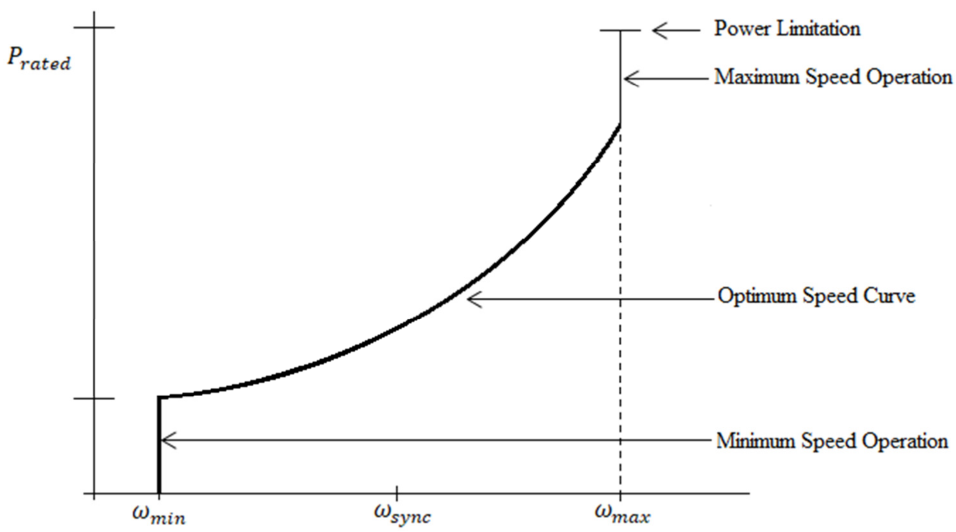

Figure 52: Power-speed curve

There are two operating regions for a wind generator: partial load region and full load region. The partial load region can be further divided into three distinct sections, namely, minimum speed operating region (MinSOR), optimum speed operating region (OSOR) and the maximum speed operating region (MaxSOR). MinSOR is chosen when the wind speed is low. So the generator speed is kept at steady at its minimum speed. This constant minimum speed is typically 30% lower than the synchronous speed. In OSOR, maximum power extraction takes place by varying the speed of the turbine at a given wind speed. This scheme is also known as the 'wind-driven mode.' The converter regulates the generator speed electromagnetically. In this mode, wind speed variations can lead to fluctuations in output power. MaxSOR is appropriate for high wind speeds because it is not possible for the generator to maintain optimum operation. This is because the generator speed cannot exceed a certain limit. Therefore, a generator speed equal to 15-20% above synchronous speed is maintained by the rotor side converter [101].

The full load region is also known as power limitation operating region. This is utilized when the wind speed crosses the rated value and, consequently, the converter cannot keep the generator speed below the maximum value. Therefore, the pitch angle controller is employed to reduce the aerodynamic torque. This is done by pitching the blade angle to decrease aerodynamic conversion. Thus the generator speed can be kept constant because there is less mechanical torque on the generator [102], [108].

3.10. Protection systems

Conventionally, two protection systems are very widely used for Type 3 wind generators, namely, rotor crowbar and dc-link chopper. Type 4 generators employ only dc-link choppers. Both are regulated using power electronic switches. The crowbar is deployed to protect the RSC from overcurrent during voltage sags/swells and the dc-link chopper safeguards the dc-link capacitor from overvoltage. The most common protection for Type 4 WG wind generator is the dc-link chopper. However, the traditional protection systems have not been utilised in this thesis. A brief discussion on both the systems is provided below [109].

The main function of the crowbar is to short-circuit the rotor in the event of a grid disturbance to prevent overcurrent in the RSC. A crowbar contains a thyristor with inserted external resistance. Conventionally, the resistance of the rotor crowbar, R_{crow}, is between 1 to 10 times of the rotor resistance. A large value of R_{crow} is good for dampening the rotor transient current but, if it is too large, it can lead to overvoltage on the converter. As a result, R_{crow} is decided by taking these factors into consideration. Equation (90) gives the maximum possible value of the crowbar resistance where $V_{r,max}$ is the maximum rotor voltage, X_s is the transient reactance of the stator and V_s is stator voltage [110].

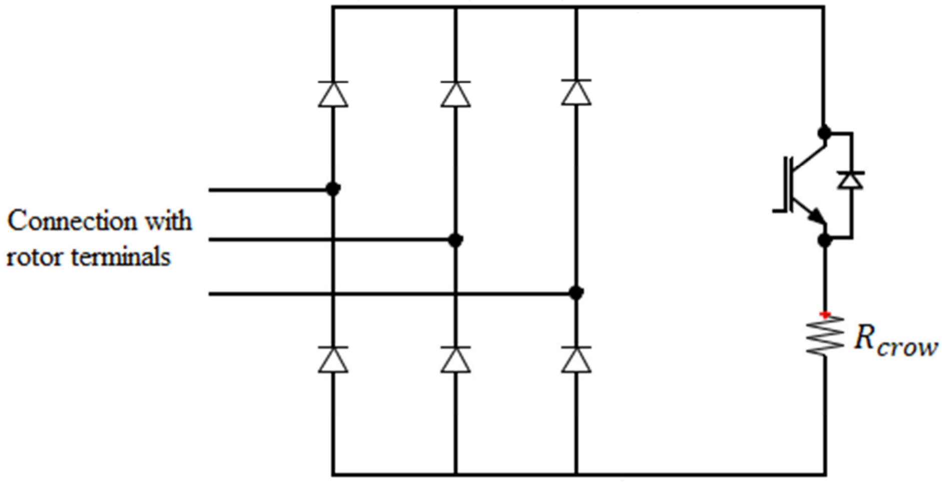

Figure 53: Active rotor crowbar configuration

$$R_{crow,max} = \frac{V_{r,max} X_s}{\sqrt{1.7|V_s|^2 - {V_{r,max}}^2}} \tag{90}$$

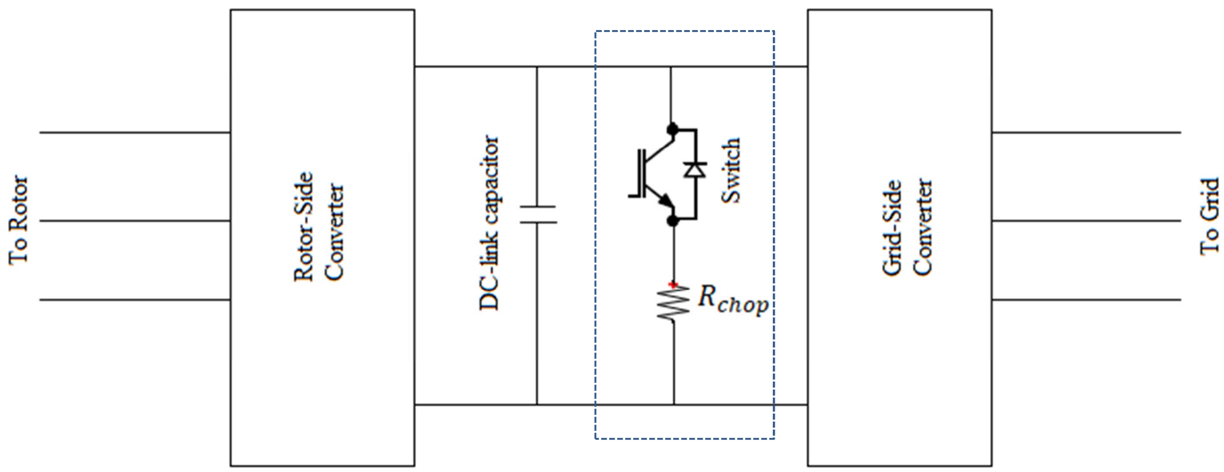

Figure 54: DC-link chopper in a back-to-back converter

The dc-link voltage or the RSC overcurrent triggers the rotor crowbar into action. The crowbar usually triggers when the dc-link voltage is 12% higher than the nominal voltage, while the protection limit for the RSC is established at 1.8 pu. A disadvantage of using a thyristor is that the crowbar can only be deactivated after taking tens of milliseconds. This is because the thyristor can only disconnect at zero crossing. As a result, it takes more time to re-engage the crowbar which is not ideal for recurrent grid disturbances. Therefore, instead of a thyristor, a GTO-thyristor or IGBT can be used in the crowbar. This is also known as an active crowbar, shown in Fig. 53, where forced commutation can be implemented to stop the rotor current [101].

The dc-link chopper is a resistor, R_{chop}, connected in parallel to the dc-link capacitor whose function is to shed excess power during a grid disturbance. This is done to protect the dc-link capacitor from overvoltage. An electronic switch, usually IGBT, is connected in series with the dc-link chopper to regulate how much power is dissipated in the chopper. A dc-link chopper connected to a back-to-back converter is shown in Fig. 54.

3.11. Summary

This chapter provides the modelling of Type 3 and Type 4 WGs utilized in this thesis. First, the aerodynamic model is presented which shows how much wind energy can be extracted by the wind turbines. This depends on the power coefficient value. The mechanical model for both Type 3 and Type 4 WGs is represented as a two-mass model. The electrical model for Type 3 WG is a doubly-fed induction generator (DFIG) in the rotor dq reference frame. Whereas, the electrical model for the Type 4 WG is a wound-rotor synchronous generator (WRSG) in the rotor dq reference frame. Type 3 implements a partial converter which is divided into the rotor side converter (RSC) and grid-side converter (GSC). The RSC regulates the flow of stator active and reactive powers, while the GSC stabilizes the dc-link capacitor voltage and regulates the reactive power flow between the converter and grid. A full-scale converter is utilized for Type 4 WGs where the generator side converter is not controllable. The grid side converter regulates reactive power flow and dc-link voltage. There is also an additional dc-dc boost converter which raises the rectified voltage from the generator side converter. Traditional vector control scheme is used for both Type 3 and Type 4 WGs to implement their converter control architecture. Thorough discussion of the RSC control scheme, the GSC control scheme, pitch angle control for Type 3 WGs is presented along with the three operating modes. For Type 4 WG, the dc excitation control, boost converter control and grid side converter control schemes are provided in detail. The operating regions of a wind generator are discussed. There are two operating regions namely, the partial load operating region and the full load operating region. The control schemes of the wind generator are utilized in the partial load region to extract maximum power from wind. The two most common protection devices used are the rotor crowbar and the dc-link chopper. Their relevance and function during grid voltage disturbance are described in brief.

Chapter 4

Analysis of the Impact of Grid Voltage Fluctuations on Wind Generators

4.1. Introduction

The stator flux is an important variable which has a major impact on the performance of wind generators. Any voltage fluctuation in the grid changes the stator flux dynamics. This, in turn, affects the performance of wind generators. Not all types of voltage fluctuations have the same level of impact on wind generators. There is a need to conduct extensive study to determine which relative degree of risk posed by different types of voltage disturbances.

4.2. Stator flux dynamics

Voltage sags and swells at PCC have an effect on the stator electromagnetic flux (ψ_s) of the machine, which, in turn, leads to overcurrents in Type 3 WG converter. It is convenient to use the stator oriented dq reference frame for the electrical machine to show the effects on the stator dynamics on the rotor voltage. The stator oriented machine equations are given in (88)-(89); while the stator and rotor fluxes are shown in (91)-(94) [111].

$$V_{dqs} = R_s I_{dqs} + \frac{d\psi_{dqs}}{dt} \tag{91}$$

$$V_{dqr} = R_r I_{dqr} + \frac{d\psi_{dqr}}{dt} - j\omega\psi_{dqr} \tag{92}$$

$$\psi_{dqs} = L_s I_{dqs} + L_m I_{dqr} \tag{93}$$

$$\psi_{dqr} = L_r I_{dqr} + L_m I_{dqs} \tag{94}$$

Combining (93) and (94), an expression for ψ_{dqr} is obtained as a function of ψ_{dqs} in (95) where σ is the leakage factor and σL_r is known as the transient inductance of the rotor. The new expression of ψ_{dqr} is substituted in (92) to get a new expression for the rotor voltage V_{dqr} in (96). According to (96), the rotor voltage comprises of two distinct terms. The first term is induced by the stator flux, while the second term is induced when there is current flowing in the rotor [112]. Therefore, the stator flux dynamics can impose a voltage on the rotor and lead to overcurrents in the RSC.

$$\psi_{dqr} = \tfrac{L_m}{L_s}\psi_{dqs} - \sigma L_r I_{dqr} \text{ ,} where$$
$$\sigma = \frac{L_s L_r - {L_m}^2}{L_s L_r} \tag{95}$$

$$V_{dqr} = \frac{L_m}{L_s}\left(\frac{d}{dt} - j\omega\right)\psi_s + \left(R_r + \sigma L_r\left(\frac{d}{dt} - j\omega\right)\right)I_{dqr} \tag{96}$$

At steady state, the stator voltage space vector is given by (97) which rotates at the synchronous speed at a constant value of V. By considering that the stator resistance is negligible in (91), the stator flux dynamics at steady state is obtained in (98). Therefore, the voltage imposed by the stator flux dynamics at steady state is shown in (99). During symmetrical voltage sags, the stator voltage is calculated as (100) where p is the depth of the voltage sag. Hence, the flux behaviour changes to that of (101). There is a dc-component in the stator flux to avoid any discontinuity and it is represented by $\frac{pV_s}{j\omega_s}e^{\frac{-t}{\tau}}$. The resulting induced rotor voltage is given in (102) [113].

$$V_{dqs} = Ve^{j\omega_s t} \tag{97}$$

$$\psi_s = \frac{V}{j\omega_s}e^{j\omega_s t} \tag{98}$$

$$V_{dqr} = V_s\frac{L_m}{L_s}\frac{\omega_r}{\omega_s} + \left(R_r + \sigma L_r\left(\frac{d}{dt} - j\omega\right)\right)I_{dqr} \tag{99}$$

$$V_s = (1-p)Ve^{j\omega_s t} \tag{100}$$

$$\psi_s = \frac{(1-p)V}{j\omega_s}e^{j\omega_s t} + \frac{pV}{j\omega_s}e^{\frac{-t}{\tau s}} \tag{101}$$

$$V_{dqr} = (1-p)V\frac{L_m}{L_s}\frac{\omega_r}{\omega_s}e^{j\omega_s t} - \frac{L_m}{L_s}\left(\frac{1}{\tau_s} + j\omega\right)\frac{pV}{j\omega_s}e^{-t/\tau s} \tag{102}$$

Equation (103) presents the stator voltage dynamics during asymmetrical voltage dips where V_1, V_2 and V_0 are positive, negative and zero sequences. It is to be noted that the zero sequence does not create any flux. Hence, the stator flux dynamics is given by (104) where $\psi_{dc}e^{\frac{-t}{\tau}}$ ensures that there is not discontinuity in the flux. The voltage imposed on the rotor by the stator flux is given in (105). Lastly, the voltage dynamics during symmetrical swells is shown in (106) which results in the stator flux in (107). Equation (108) gives the voltage imposed on the rotor. Therefore, it is evident that the stator fluxes arising from grid voltage fluctuations induce a voltage in the generator rotor and this causes overcurrents in the RSC of a Type 3 WG [111]-[113]. However, the phenomenon of overcurrents in the RSC converter is not relevant to Type 4 wind generator systems.

$$V_{dqs} = V_1 e^{j\omega_s t} + V_2 e^{-j\omega_s t} + V_0 \tag{103}$$

$$\psi_s = \frac{V_1}{j\omega_s} e^{j\omega_s t} - \frac{V_2}{j\omega_s} e^{-j\omega_s t} + \psi_{dc} e^{\frac{-t}{\tau}} \tag{104}$$

$$V_{dqr} = V_1 \frac{L_m}{L_s}\frac{\omega_r}{\omega_s} e^{j\omega_r t} + V_2 \frac{L_m}{L_s}\left(\frac{\omega_r}{\omega_s} - 2\right) e^{-j\left(2-\frac{\omega_r}{\omega_s}\right)\omega_s t} - j\omega \frac{L_m}{L_s}\psi_{dc} e^{\frac{-t}{\tau s}} e^{-j\omega t} \tag{105}$$

$$V_{dqs} = (1+p)V e^{j\omega_s t} \tag{106}$$

$$\psi_s = \frac{V_s(1+p)}{j\omega_s} e^{j\omega_s t} - \frac{V_s}{j\omega_s} e^{\frac{-t}{\tau}} \tag{107}$$

$$V_{dqr} = V \frac{L_m}{L_s}\frac{\omega_r}{\omega_s}(1+p) e^{j\omega_s t} + \frac{L_m}{L_s}(1 - \frac{\omega_r}{\omega_s}) V p e^{j\omega_s t} e^{-t/\tau s} \tag{108}$$

The impact of grid voltage fluctuations on Type 3 WGs are given in Figures 55, 56, 57 and 58. When there is no grid disturbance, the d-axis stator voltage stays constant at 1 pu while the q-axis stator voltage is at 0 pu. The stator magnetic flux is steady around 1.02 pu in normal conditions. When a symmetrical sag occurs at PCC in Figure 55, the d-axis stator voltage rises to a peak of 0.64 pu and then maintains a steady value of 0.73 pu during the rest of the sag. The value of the q-axis stator voltage drops to a maximum of 0.15 pu and then slowly goes to zero. The stator magnetic flux value increases to a maximum value of 0.68 pu and then steadies at 0.74 pu during the rest of the sag. In Figure 56, a 30% asymmetrical sag occurs at PCC, the d-axis stator voltage rises to a maximum of 0.66 pu and then oscillates approximately between 0.70 pu and 0.95 pu. The q-axis stator voltage rises to a peak of 0.25 pu and drops to a minimum of -0.19 pu, oscillation is also present. The stator magnetic flux drops to a minimum of 0.78 pu and also exhibits oscillatory behaviour.

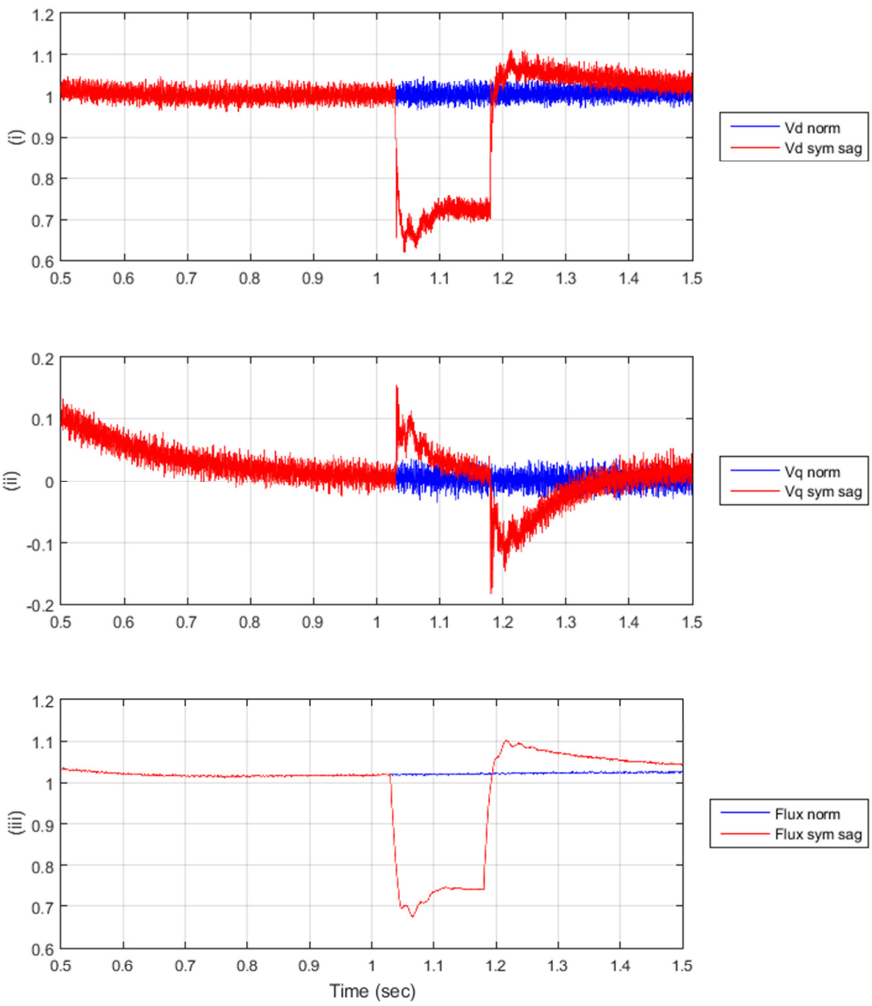

Figure 55: Type 3 wind generator response to 30% symmetrical voltage sag at PCC. (i) Stator d-axis voltage (pu). (ii) Stator q-axis voltage (pu). (c) Stator magnetic flux (pu).

The wind generator is exposed to a 30% symmetrical swell at PCC in Figure 57. The d-axis stator voltage rises to 1.30 pu at its peak and then gradually comes down, while the q-axis stator voltage falls to a minimum of -0.12 pu and then starts rising gradually. The magnetic flux rises to a peak of 1.29 pu and then falls gradually. In Figure 58, the wind generator is exposed to a 30% voltage swell at PCC and the d-axis stator voltage increases to a maximum of 1.07 pu and there is oscillation present. The q-axis stator voltage goes up to a maximum of 0.17 pu and drops to a minimum of -0.22 pu, oscillation is observed. There is oscillation in the stator magnetic flux value which rises to a maximum of 1.22 pu.

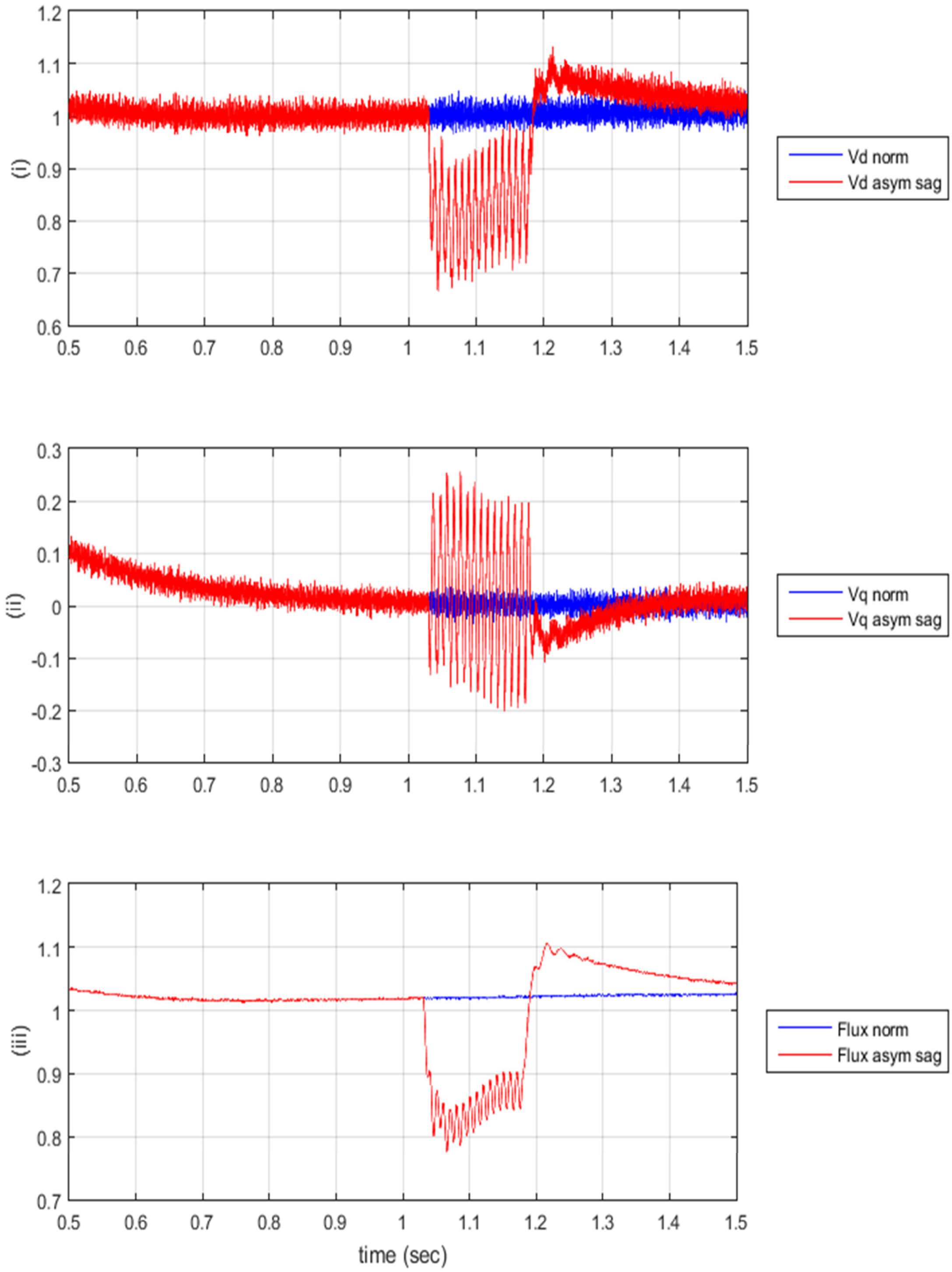

Figure 56: Type 3 wind generator response to 30% asymmetrical voltage sag at PCC. (i) Stator d-axis voltage (pu). (ii) Stator q-axis voltage (pu). (c) Stator magnetic flux (pu).

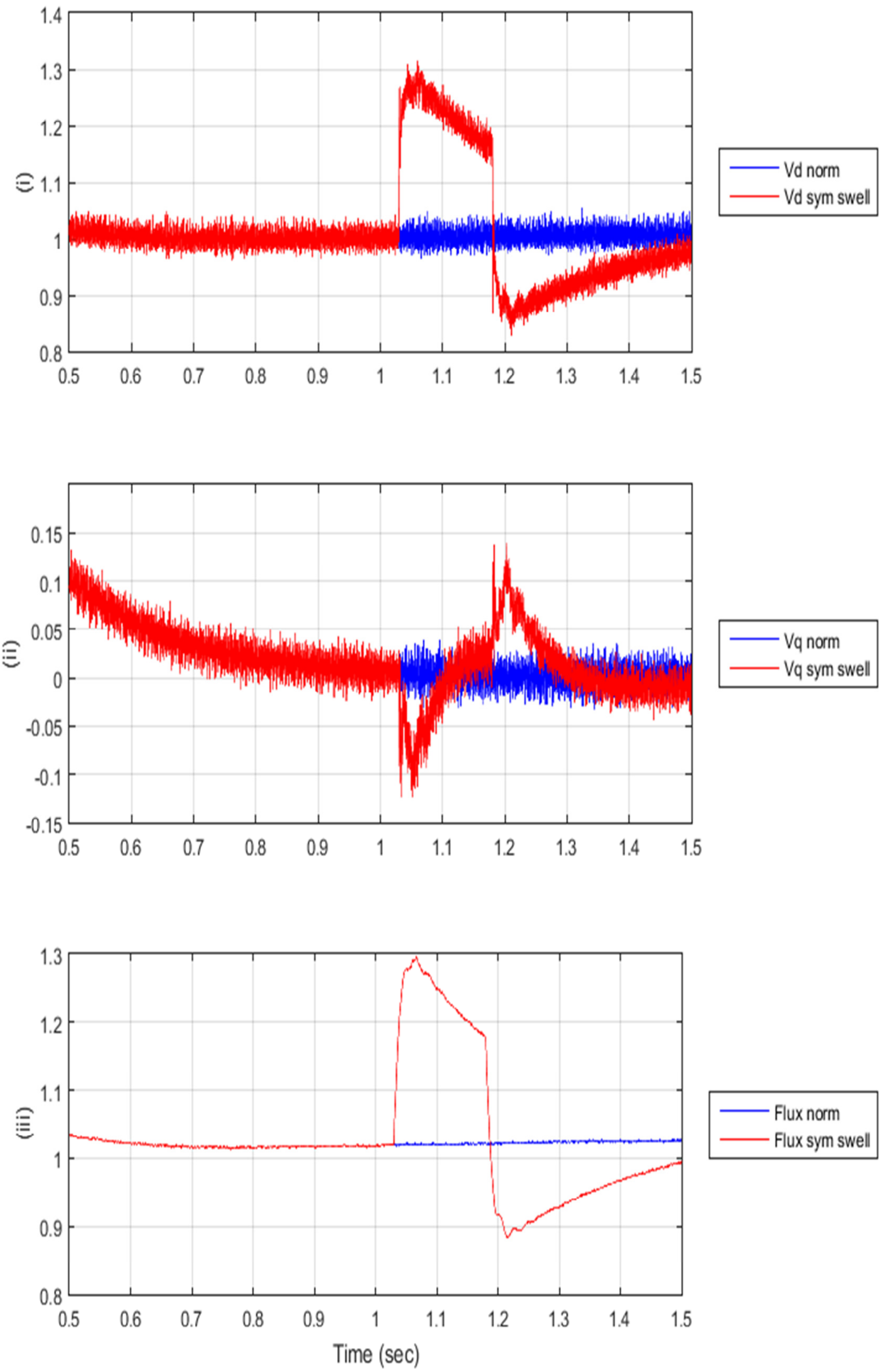

Figure 57: Type 3 wind generator response to 30% symmetrical voltage swell at PCC. (i) Stator d-axis voltage (pu). (ii) Stator q-axis voltage (pu). (c) Stator magnetic flux (pu).

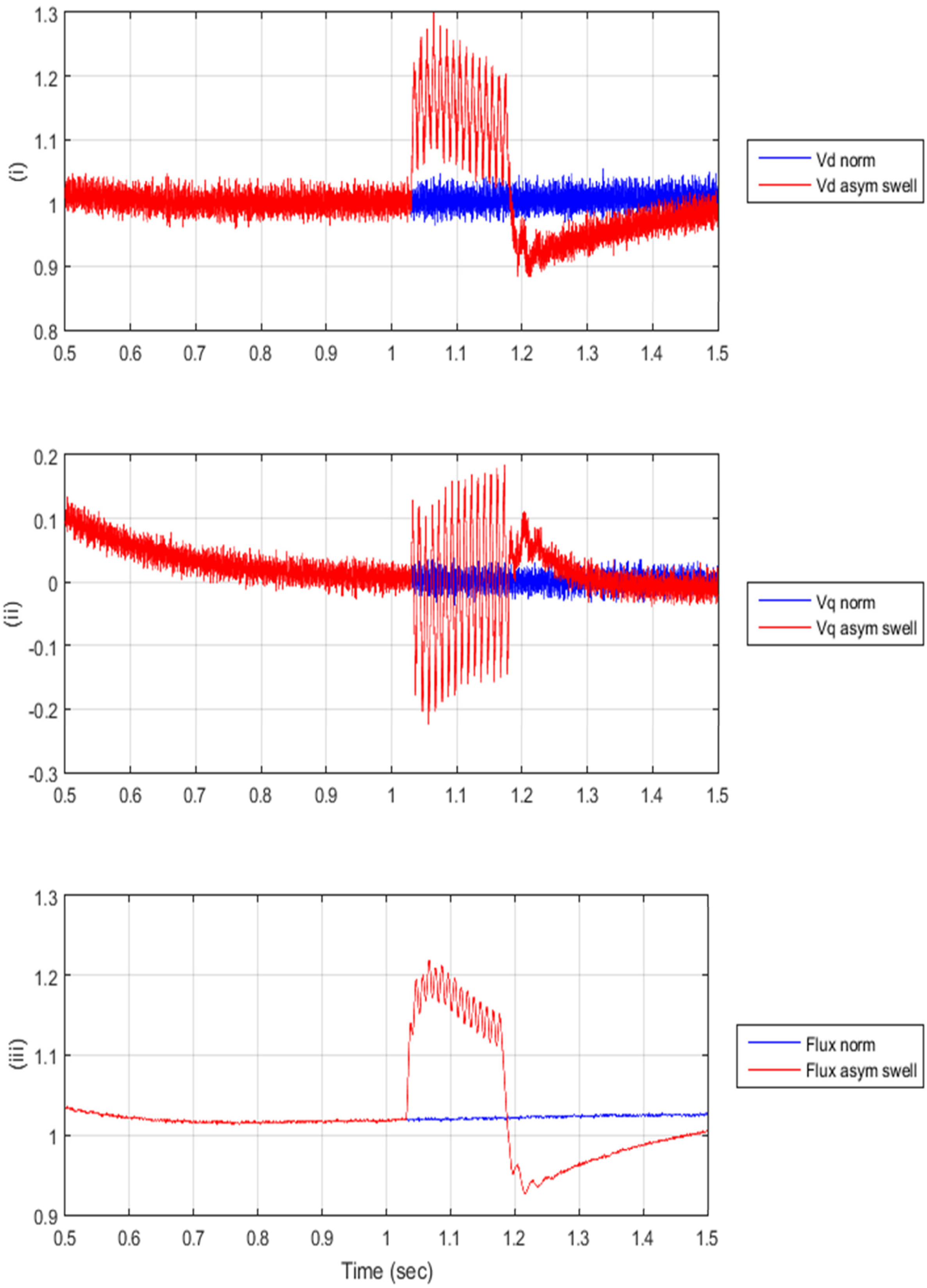

Figure 58: Type 3 wind generator response to 30% asymmetrical voltage swell at PCC. (i) Stator d-axis voltage (pu). (ii) Stator q-axis voltage (pu). (c) Stator magnetic flux (pu).

Grid voltage fluctuations also cause dc-link overvoltage in both Type 3 and Type 4 wind generator systems. The dc-link capacitance encounters overvoltage which can lead to capacitor damage. In the absence of the dc-link capacitor, the wind generator converter cannot operate because the capacitor is an essential energy buffer between the rotor-side/generator-side converter and grid-side converter. Both voltage sags and swells can be the cause of dc-link overvoltage, and can be explained using (109) which shows the dynamics of the dc-link capacitor. C and V_c are dc-link capacitance and voltage respectively; P_f and P_g are grid-filter and rotor power in that order. When the power transferred by the generator to the dc-link capacitor, P_g, equals the power transferred from the dc-link capacitor to the grid filter, P_f, the dc-link voltage remains constant [114]. A power imbalance occurs due to voltage sag or swell where P_r and P_f do not have the same value. This leads the dc-link capacitor voltage to increase. As an alternative explanation, it can also be stated that there is excess energy being delivered into the dc-link capacitor during both voltage sags and swells. Hence, the dc-link voltage increases consistent with (110). The solution to maintain an acceptable dc-link voltage is to either reduce the energy delivered to the capacitor, E_c, or to raise the capacitance value of the dc-link, C_{Total}.

$$CV_c\frac{dV_c}{dt} = P_f - P_r \tag{109}$$

$$V_c = \sqrt{\frac{2E_c}{C_{Total}}} \tag{110}$$

An alternative explanation for the loss of power balance during grid voltage disturbance is given below. The mechanical power, $\boldsymbol{P_t}$, is equal to the sum of stator power, $\boldsymbol{P_s}$, and rotor power, $\boldsymbol{P_r}$. The power flow between stator and grid, $\boldsymbol{P_s}$, and the power flow between the filter and grid, $\boldsymbol{P_f}$, are given in (111) and (112) where $\boldsymbol{X_s}$, $\boldsymbol{\delta_s}$, $\boldsymbol{X_f}$ and $\boldsymbol{\delta_f}$ are stator reactance, stator phase angle, filter reactance and filter phase angle respectively.

$$P_t = P_s + P_r \tag{111}$$

$$P_s = \frac{V_s V_g}{X_s}\sin\delta_s \tag{112}$$

$$P_f = \frac{V_s V_g}{X_f} \sin \delta_f \tag{113}$$

At steady state, the grid voltage, V_g, is constant. While the grid voltage changes during transients changing the value of P_s and P_f. Therefore, at steady state the power flow equation is that of (113). If a single-mass model is considered for simplification, then the following torque balance equation is obtained where J is the rotor-turbine inertia. By multiplying (114) by ω_r, a power balance equation can be obtained as in (115). At steady state, the value of ω_r stays constant, the power balance equation is thus equal to zero as in (116).

$$J \frac{d\omega_r}{dt} = T_t - T_e \tag{114}$$

$$\omega_r J \frac{d\omega_r}{dt} = P_t - P_e \tag{115}$$

$$\omega_r J \frac{d\omega_r}{dt} = P_t - P_e = 0 \tag{116}$$

In transient state, for example, a sag event, the value of V_g decreases which causes P_s and P_f to decrease instantly. The rotor power, P_r, increases according to (117) as the electrical power does not change. Consequently, the rotor power, P_r, does not stay equal to the power delivered to the grid, P_f. Hence, the power balance in the dc-link is lost as shown in (118).

$$P_r = P_e - P_s \tag{117}$$

$$P_r - P_f > 0 \tag{118}$$

According to (109), this results in $\boldsymbol{\frac{dV}{dt} > 0}$ and hence the increase of $\boldsymbol{V_c}$, and the charging current, $\boldsymbol{i_{charge}}$ to the dc-link equals $\boldsymbol{\frac{1}{C}\frac{dV}{dt} = \frac{P_r - P_f}{C}}$ which causes overcurrent of RSC.

4.3. Comparative study of wind generator behaviour

A comparative study of the dynamic behaviour of Type 3 and Type 4 wind generators in the event of voltage sags and swells is conducted. Both symmetrical and asymmetrical voltage sags and swells are considered. This relative analysis provides an understanding of the relative degree of risk involved in various grid voltage conditions to the normal operation of wind generators. It is observed that certain voltage conditions are more harmful than others to the functioning of wind generators. The comparison results can be useful while designing sophisticated protection schemes for wind turbine generators. In Fig. 59, a grid-connected 9-MW Type 3 wind farm or a 10-MW Type 4 wind farm is utilized for simulation in MATLAB/SimPowerSystems.

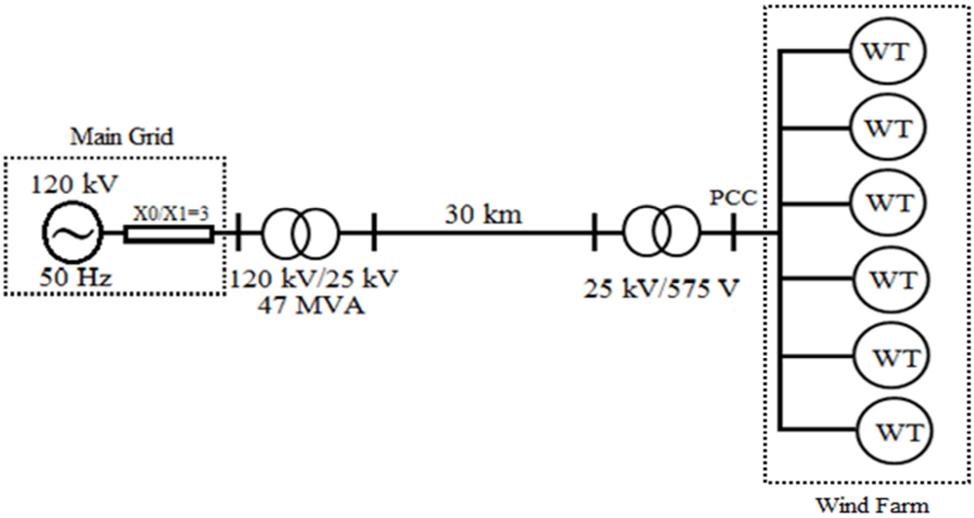

Figure 59: Type 3/Type 4 grid-connected wind farm

4.3.1. Type 3 wind generator response to voltage sags

In Fig. 60, a comparative study is done to observe the effect of symmetrical and asymmetrical voltage sags on Type 3 wind generators. A 30% voltage sag occurs in all three phases in case of the symmetrical sag, while, for the asymmetrical sag, there is a 30% voltage sag only in one of the phases (it is phase B is this study). The voltage sag lasts for a duration of 150 ms. It is seen that asymmetrical sags lead to oscillation in rotor and stator currents, electromagnetic torque and dc-link voltage, while there is slight oscillation for symmetrical sags. The maximum change in the value of torque is 0.92 pu during symmetrical sags and 1.48 pu during asymmetrical sags. Oscillation in the electromagnetic torque can decrease the operating lifetime of the wind turbine drive train.

The maximum d-axis rotor currents are 1.21 pu and 1.37 pu for symmetrical and asymmetrical sags respectively, and the maximum q-axis rotor currents are -0.94 pu and -1.4 pu for symmetrical and asymmetrical sags in that order. Hence, the maximum rotor current in the d and q-axis is higher for asymmetrical sags. An overcurrent will cause damage to the RSC. There is also a higher overvoltage in the dc-link in the event of asymmetrical sags, which can destroy the dc-link capacitor. The maximum overvoltages for symmetrical and asymmetrical sags are 1181 V and 1193 V correspondingly. Hence, it is evident from the simulation results that asymmetrical sags pose a greater risk to the functioning of Type 3 wind generators than symmetrical sags.

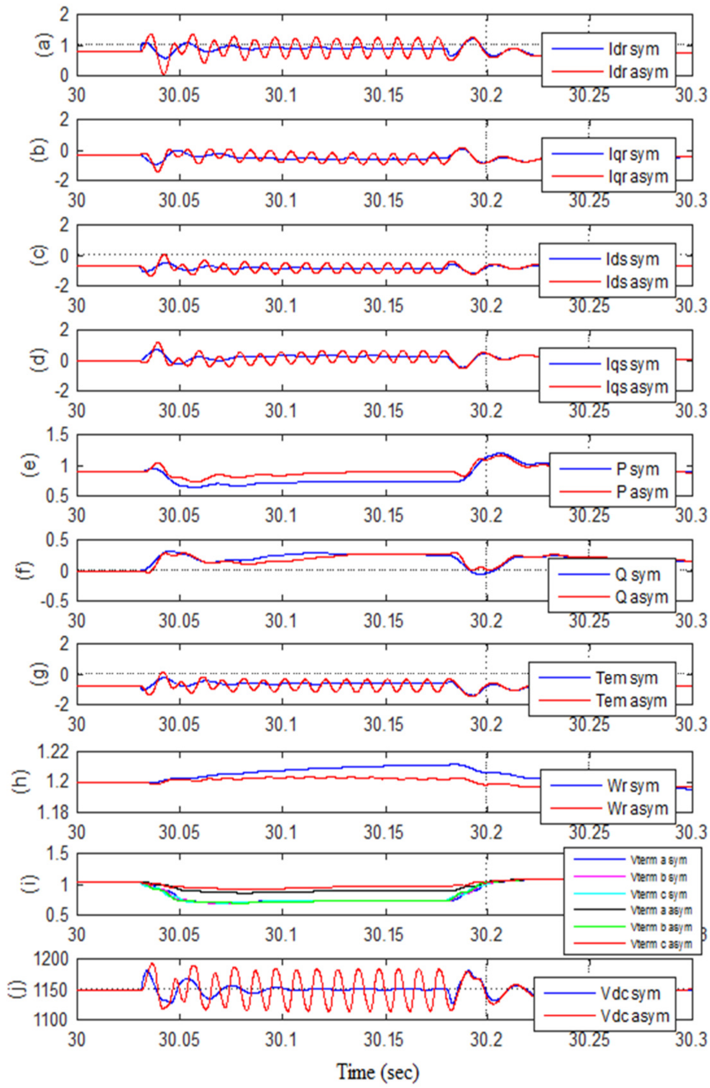

Figure 60: Type 3 wind generator simulation results for 30% symmetrical and asymmetrical voltage sags for 150 ms at PCC. (a) Rotor d-axis current (pu). (b) Rotor q-axis current (pu). (c) Stator d-axis current (pu). (d) Stator q-axis current (pu). (e) Active power (pu). (f) Reactive power (pu). (g) Electromagnetic torque (pu). (h) Rotor speed (pu). (i) Terminal voltage (pu). (j) DC-link voltage (V).

4.3.2. Type 3 wind generator response to voltage swells

In Fig. 61, a 30% voltage swell happens in all three phases during symmetrical swell, while only voltage in phase B rises by 30% during asymmetrical swell. The voltage swell lasts for a duration of 50 ms. It is seen that rotor and stator currents, electromagnetic torque and dc-link voltage exhibit some oscillation during the asymmetrical swell but not during the symmetrical swell. The maximum torque changes for symmetrical and asymmetrical swells are 0.73 pu and 1.35 p.u respectively. Torque oscillation can decrease the operating lifetime of the wind turbine drive train.

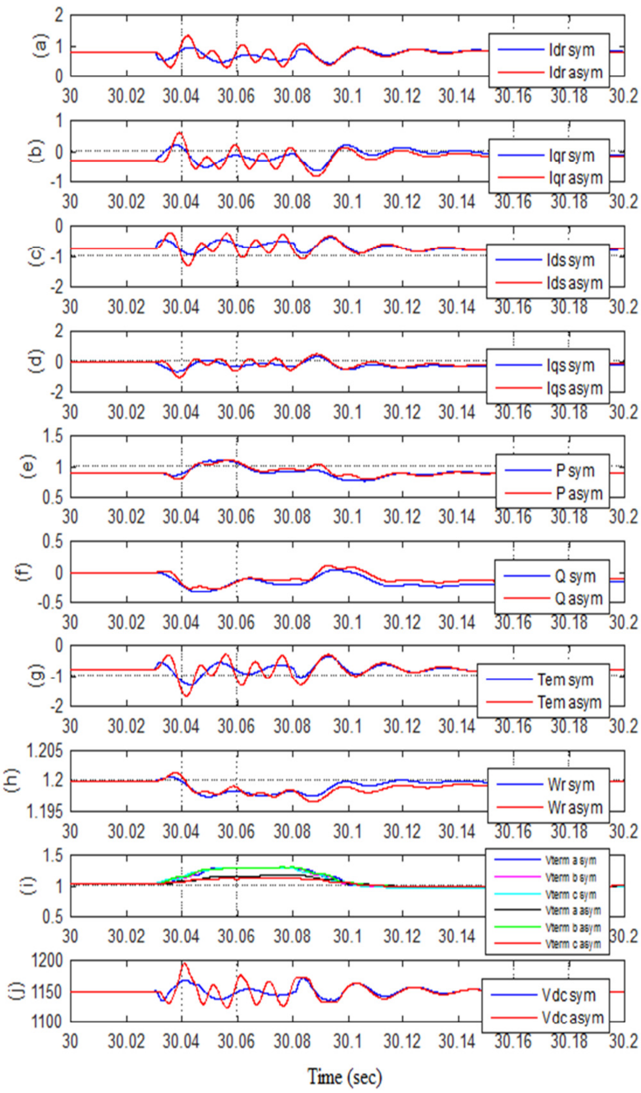

Figure 61: Type 3 wind generator simulation results for 30% symmetrical and asymmetrical voltage swells for 50 ms at PCC. (a) Rotor d-axis current (pu). (b) Rotor q-axis current (pu). (c) Stator d-axis current (pu). (d) Stator q-axis current (pu). (e) Active power (pu). (f) Reactive power (pu). (g) Electromagnetic torque (pu). (h) Rotor speed (pu). (i) Terminal voltage (pu). (j) DC-link voltage (V).

The maximum d-axis rotor overcurrents are 0.95 pu and 1.33 pu for symmetrical and asymmetrical swells respectively, and the maximum overvoltages are 1172 V and 1195 V for symmetrical and asymmetrical swells respectively. Thus, there is a higher overcurrent in the rotor in the event of asymmetrical swells which can destroy the RSC, likewise, the dc-link overvoltage is much higher, which has the potential to damage the dc-link capacitor. Therefore, it is apparent that asymmetrical voltage swells are more damaging to Type 3 wind generators than symmetrical swells.

4.3.3. Type 3 wind generator comparative response for sags and swells

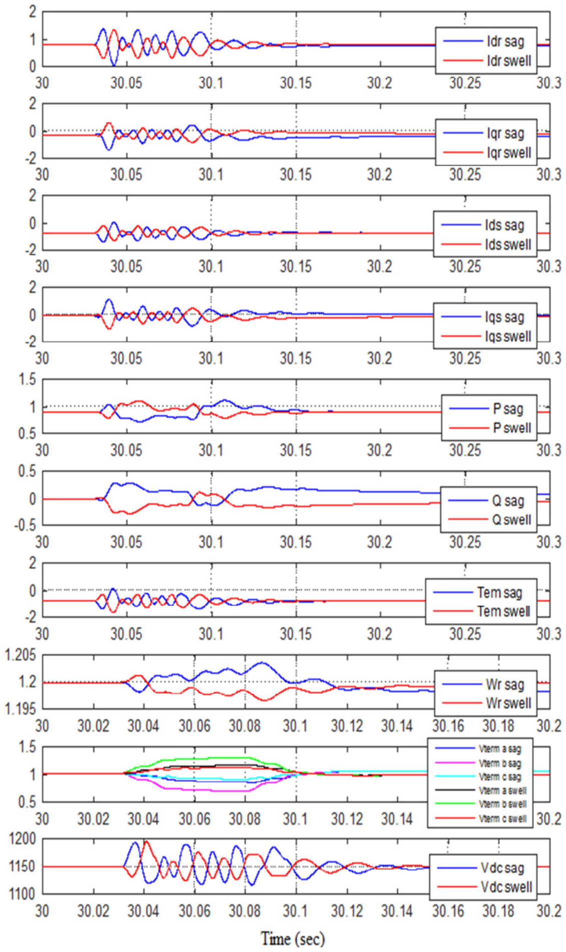

Figure 62: Type 3 simulation results for 30% asymmetrical voltage sags and swells for 50 ms at PCC. (a) Rotor d-axis current (pu). (b) Rotor q-axis current (pu). (c) Stator d-axis current (pu). (d) Stator q-axis current (pu). (e) Active power (pu). (f) Reactive power (pu). (g) Electromagnetic torque (pu). (h) Rotor speed (pu). (i) Terminal voltage (pu). (j) DC-link voltage (V).

In Fig. 60 and Fig. 61, it is observed that asymmetrical voltage sags and swells are more destructive for Type 3 wind generators. In Fig. 62, the impact of asymmetrical voltage sags and swells are compared to ascertain which one presents the greatest danger to the normal operation of Type 3 wind generators. A 30% sag takes place in phase B for the asymmetrical voltage sag and a 30% rise happens in phase B for the asymmetrical voltage swell. The duration for both is 50 ms. It is noticed that the d-axis rotor overcurrents are 1.37 pu and 1.33

pu for sags and swells respectively. The q-axis rotor overcurrents for sags and swells are 1.43 pu and 0.61 pu in that order. Thus, the sag leads to more damage of the RSC compared to the swell. Nonetheless, the DC-link maximum overvoltage for the swell is 1195 V, while it is 1193 V for the sag. Hence, the swell is marginally more harmful for the dc-link capacitor. Both asymmetrical sags and swells exhibit oscillation in some of the generator variables. However, the maximum change in electromagnetic torque for the sag is 1.49 p.u which is more than that for the swell (1.35 pu). Consequently, the overall risk posed by asymmetrical sags to Type 3 wind generators is greater.

4.3.4. Type 4 wind generator response to voltage sags

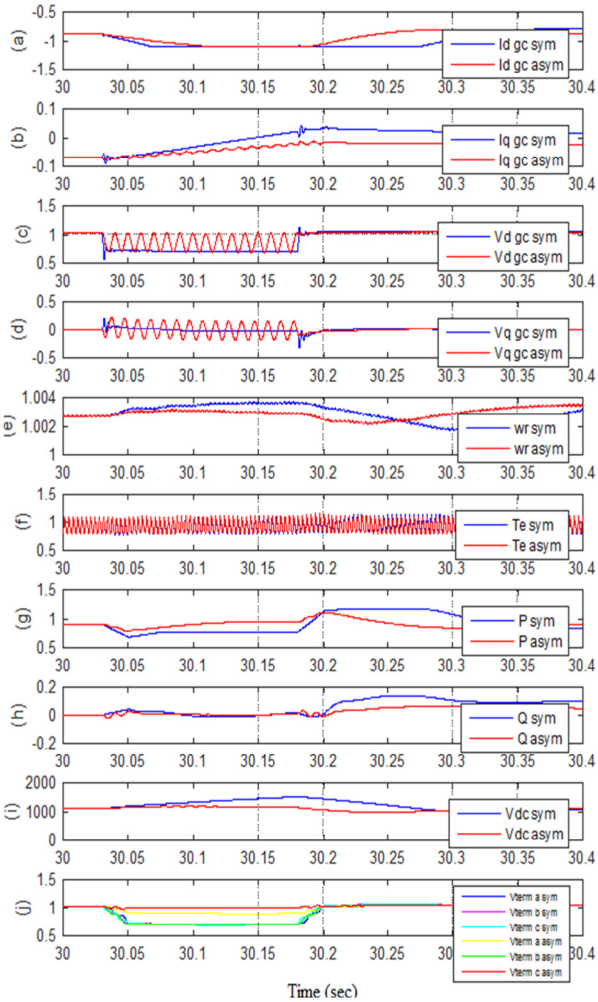

Figure 63: Type 4 simulation results for 30% symmetrical and asymmetrical voltage sags for 150 ms at PCC. (a) Grid- side converter d-axis current (pu). (b) Grid-side converter q-axis current (pu). (c) Grid-converter d-axis current (pu). (d) Grid-side converter q-axis current (pu). (e) Rotor speed (pu). (f) Electromagnetic torque (pu). (g) Active power (pu). (h) Reactive power (pu). (i) DC-link voltage (V). (j) Terminal voltage (pu

4.3.5. Type 4 wind generator response to voltage swells

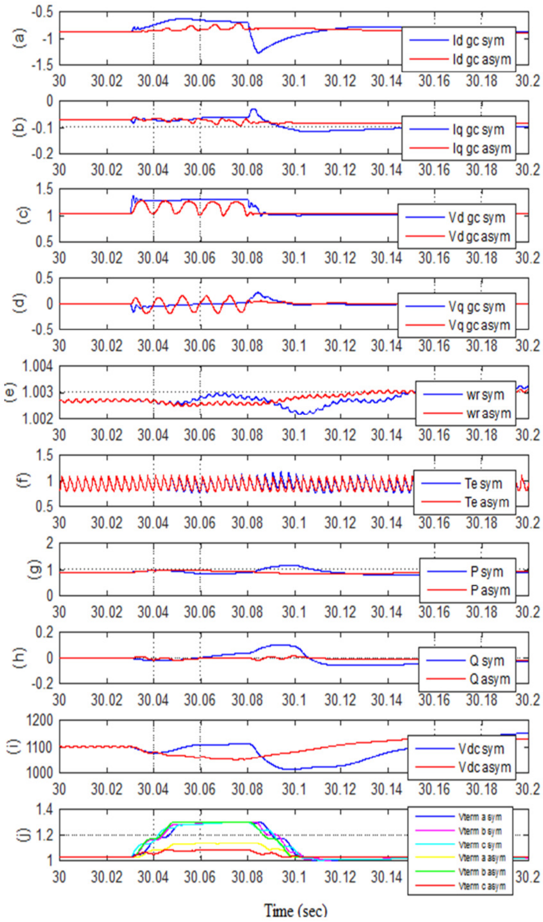

Figure 64: Type 4 simulation results for 30% symmetrical and asymmetrical voltage swells for 50 ms at PCC. (a) Grid- side converter d-axis current (pu). (b) Grid-side converter q-axis current (pu). (c) Grid-converter d-axis current (pu). (d) Grid-side converter q-axis current (pu). (e) Rotor speed (pu). (f) Electromagnetic torque (pu). (g) Active power (pu). (h) Reactive power (pu). (i) DC-link voltage (V). (j) Terminal voltage (pu).

In Fig. 64, a 30% swell takes place in all three phases during the symmetrical swell and only phase B voltage increases by 30% in the event of the asymmetrical swell for a time duration of 50 ms. The grid converter voltage exhibits oscillation during the asymmetrical swell but it is absent during the symmetrical swell. The maximum d-axis grid converter currents are -1.27 pu and -0.76 pu for symmetrical and asymmetrical swells in that order. The current value is larger for the symmetrical swell. There is minor variation in the rotor speed for the symmetrical swell. The active power drops to 0.84 pu and 0.94 pu for symmetrical and asymmetrical swells correspondingly. In the dc-link capacitor, an overvoltage occurs during the symmetrical swell and an under-voltage happens during the asymmetrical swell. The maximum overvoltage during the symmetrical swell is 1113 V and the maximum undervoltage for the asymmetrical swell is 1050V. Therefore, symmetrical swells are more damaging to the dc-link and can lead to more destruction of the converter. Thus, it can be stated that symmetrical swells are more damaging to Type 4 wind generators.

4.3.6. Type 4 wind generator comparative response for sags and swells

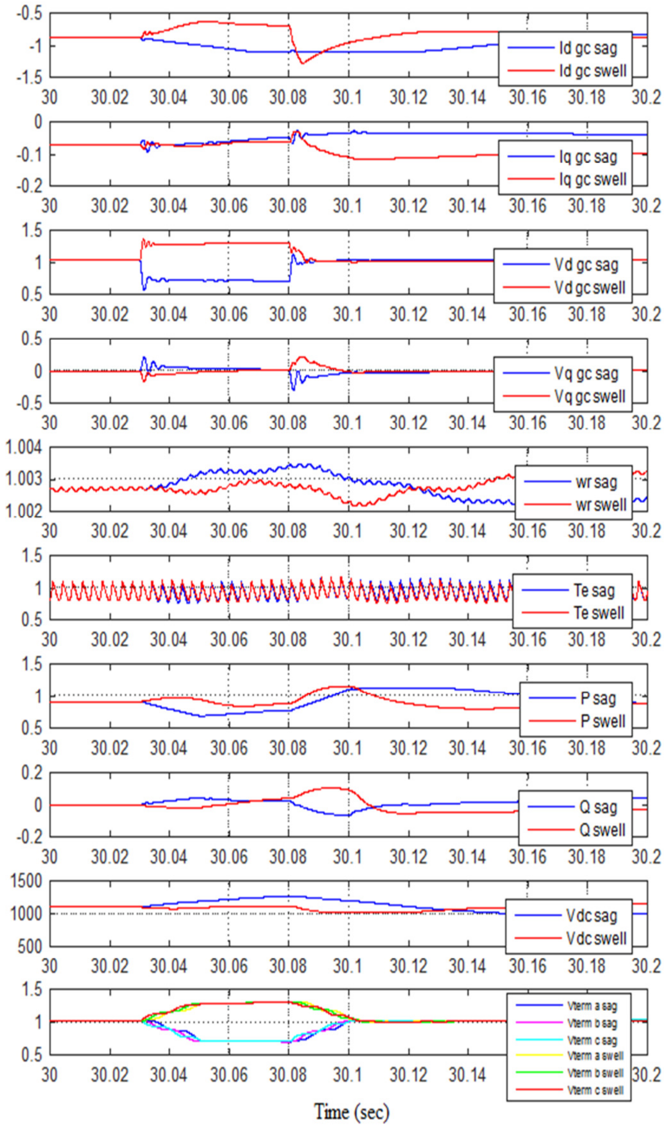

Figure 65: Type 4 simulation results for 30% symmetrical sag and symmetrical voltage swell for 50 ms at PCC. (a) Grid- side converter d-axis current (pu). (b) Grid-side converter q-axis current (pu). (c) Grid-converter d-axis current (pu). (d) Grid-side converter q-axis current (pu). (e) Rotor speed (pu). (f) Electromagnetic torque (pu). (g) Active power (pu). (h) Reactive power (pu). (i) DC-link voltage (V). (j) Terminal voltage (pu).

In Fig. 63 and Fig. 64, it is observed that symmetrical sags and swells lead to more destruction to Type 4 wind generators. In Fig. 65, a comparative study is performed between the effects of symmetrical sags and swells to ascertain which one is poses a greater risk to Type 4 wind generators. A 30% sag happens in all three phases during the symmetrical sag and a 30% swell takes place in all three phases during the symmetrical swell. The sags and swells last for a length of 50 ms. It is observed that the d-axis grid converter current goes up to -1.10 pu during the sag but drops to -0.63 p.u during the swell. Likewise, the respective active power output drops during the sag and swell are 0.68 pu and 0.84 pu. In the dc-link capacitor, overvoltages of 1273 V and 1113 V occur for the sag and swell in that order. Consequently, the symmetrical sag is more damaging to the dc-link capacitor and can lead to greater destruction of the converter. To sum up, it can be stated that symmetrical sags are of greater risk to Type 4 wind turbine generators.

4.4. Summary

Any change in the grid voltage has an impact on the stator flux linkage of the wind generator and the balance of its input and output power. In case of Type 3 WGs, the change in the stator flux magnitude is reflected in the rotor voltage of the generator. This means the stator flux can impose a voltage on the rotor of the Type 3 WG and that drives an extra current to the dc-link resulting in harmful overcurrents in the rotor side converter. These overcurrents can cross the maximum allowable limit and damage the converter permanently. A detailed study of the change of stator flux during different types of grid voltage disturbance is conducted. It is found that there is significant change in the stator flux when grid voltage fluctuations occur. In case of both Type 3 and Type 4 WGs, grid voltage fluctuations lead to overvoltage in the dc-link of the converter. An excessive overvoltage can damage the dc-link and make the converter dysfunctional. Grid voltage fluctuations cause a power imbalance in the dc-link capacitor where the power received form the rotor is not equal to the power delivered to the grid. Consequently, there is a build-up of additional energy in the capacitor leading to harmful overvoltages. Finally, theses overcurrents and overvoltages have to be dealt with during all types of grid voltage disturbances. A study of the impact of different types of grid voltage fluctuations reveal that asymmetrical voltage disturbance is more damaging to Type 3 WGs, whereas symmetrical voltage disturbance tends to be more harmful for Type 4 WGs.

Chapter 5

Ride-through Performance Enhancement of Type 3 Wind Farms

5.1. Introduction

The need for a novel comprehensive solution to the technical issues faced by Type 3 WGs has been well established in the previous chapters. The feasibility of higher wind power integration is enhanced significantly with such a ride-through enhancement scheme. While, protection and performance of the wind generator system are the main concern of the scheme, it should also provide some type of reactive power support to stabilize the grid. This chapter presents an innovative ride-through strategy that enhances Type 3 wind farm performance during grid voltage disturbance and provides grid augmentation through appropriate regulation of reactive power.

5.2 Type 3 wind farm performance enhancement scheme

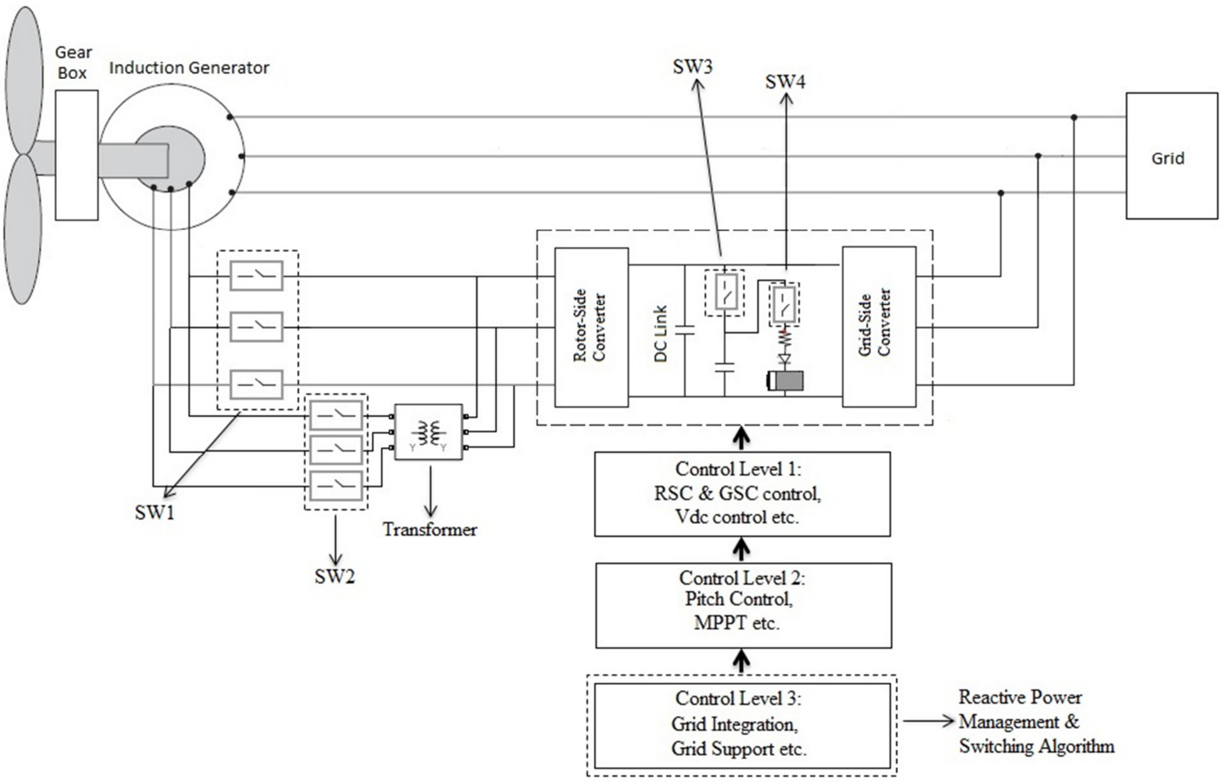

Figure 66: Type 3 wind generation ride-through strategy

A novel integrated ride-through scheme is developed for Type 3 wind generators to improve their operation in the event of voltage sags and swells. The ride-through scheme is divided into a protection system and a reactive power management system. Both symmetrical and asymmetrical voltage sags and swells have been taken into account in the design of the ride-through scheme. The protection system restricts the overcurrent in the Rotor Side Converter (RSC) and maintains the dc-link voltage inside a suitable range, while the reactive power management augments the grid by either supplying or absorbing reactive power to decrease the magnitude of voltage sags and swells.

The protection configuration in Fig. 66comprises two parts. The first part consists of a three-phase step-up transformer connected between the generator rotor and the RSC. Switch sets SW1 and SW2 are used to regulate the insertion of the transformer in the circuit. Under normal operation, SW1 is closed and SW2 is open. Hence, the transformer is by-passed by the rotor current. When a voltage sag is detected, SW1 opens and SW2 closes to include the transformer between the rotor windings and the RSC. The switching time is assumed to be instantaneous. According to (119), the power in the primary transformer circuit is the same as in the secondary circuit. As the voltage at the RSC, V_{second}, is stepped up slightly, the current, I_{second}, flowing through the RSC is reduced considerably, as shown in (120). This ensures that the RSC power electronic switches are not damaged during voltage sags. When the voltage sag is cleared, the system goes back to the normal operation mode. The same algorithm is used for voltage swells, which gets rid of excessive current peaks at the beginning of the swell. The voltage at the RSC in normal operation is 1975 V [115]. Hence, the transformer ratio is designed in such a way to get a step-up voltage of 2350 V. It is found, through trial and error, that this value is sufficient to restrict the excessive current through RSC and it is also well below the maximum voltage capability of IGBTs [8].

$$P_r = V_{prim} I_{prim} = V_{second} I_{second} \tag{119}$$

$$I_{second} = \frac{P_r}{V_{second}} \tag{120}$$

The second part of the protection system involves an additional capacitor connected in parallel with the dc-link capacitor. Moreover, there is a discharge circuit for the additional capacitor containing a rechargeable Nickel-Metal-Hydride battery. The battery is connected in series with a diode and a resistor. The inclusion of the capacitor and battery are controlled using switches SW3 and SW4. Under normal operation, SW3 stays open and SW4 stays closed. The total capacitance of the dc-link arm, C_{Total}, is equal to the dc-link capacitor, $C_{dc-link\,capacitor}$ given in (121). $C_{dc-link\,capacitor}$ has a typical capacitance of 10000 μF [115]. When a voltage sag/swell is detected by the supervisory controller, SW3 is closed and

SW4 is opened. This includes the additional capacitance, $C_{additional\ capacitance}$, in parallel with the dc-link capacitor, $C_{dc-link}$, thereby increasing the total capacitance, C_{Total}, in (122). The additional capacitance is chosen to be 200000 μF because it has been found, through trial and error, that this is sufficient to limit the dc-link voltage and also avoid high currents flowing through just one capacitor during a sag or swell event. It should be noted that the additional capacitance represents 15 capacitors of value 10000 μF each connected in parallel. Therefore, though the value of E_c goes up in (110), V_c stays within an acceptable limit. Hence, the dc-link capacitor does not get damaged and the DFIG converter can continue to operate normally. When the voltage sag/swell is cleared, the SW3 opens and SW4 closes. The additional capacitors are then discharged into the Nickel-Metal-Hydride battery. The series resistor avoids any current spikes during switching; while, the diode stops the battery from discharging back into the capacitor. Parallel additional capacitors have been used in [50] where the excess energy is dissipated in a resistor. However, in our protection scheme, the capacitor is discharged into the battery. The accumulated energy in the battery is then fed back into the grid shown in Fig. 67 with the help of a simple converter control mechanism.

$$C_{Total} = C_{dc-link\ capacitor}\ without\ additional\ capacitor \tag{121}$$

$$C_{Total} = C_{dc-link\ capacitor} + C_{additional\ capacitor} \tag{122}$$

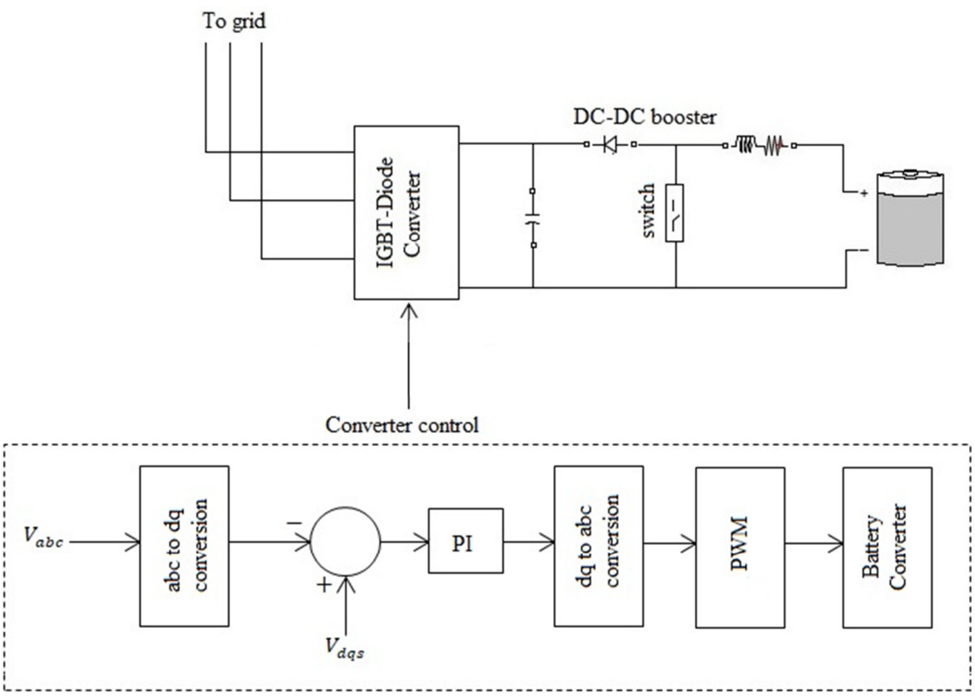

Figure 67: Feeding back stored battery energy into the grid

Traditionally, the DFIG is operated at unity power factor at all times, even during grid voltage transients. However, this is no longer a feasible option as the reactive power generated/consumed by the DFIG converter is kept at zero. This is accomplished by keeping the reactive current reference generation at zero. Hence, this mode of operation does not provide any support to grid voltage stability. Equation (123) shows the reactive power dynamics of the Type 3 wind generator converter. V_{q_conv} and $V_{d_{conv}}$ are grid-side converter d and q-axis voltages; whereas, I_{d_conv} and $I_{q_{conv}}$ are d and q-components of grid-side converter currents. These components are controlled in such a way that Q_{conv} is always set to zero.

$$Q_{conv} = V_{q\_conv} I_{d\_conv} - V_{d\_conv} I_{q\_conv} \tag{123}$$

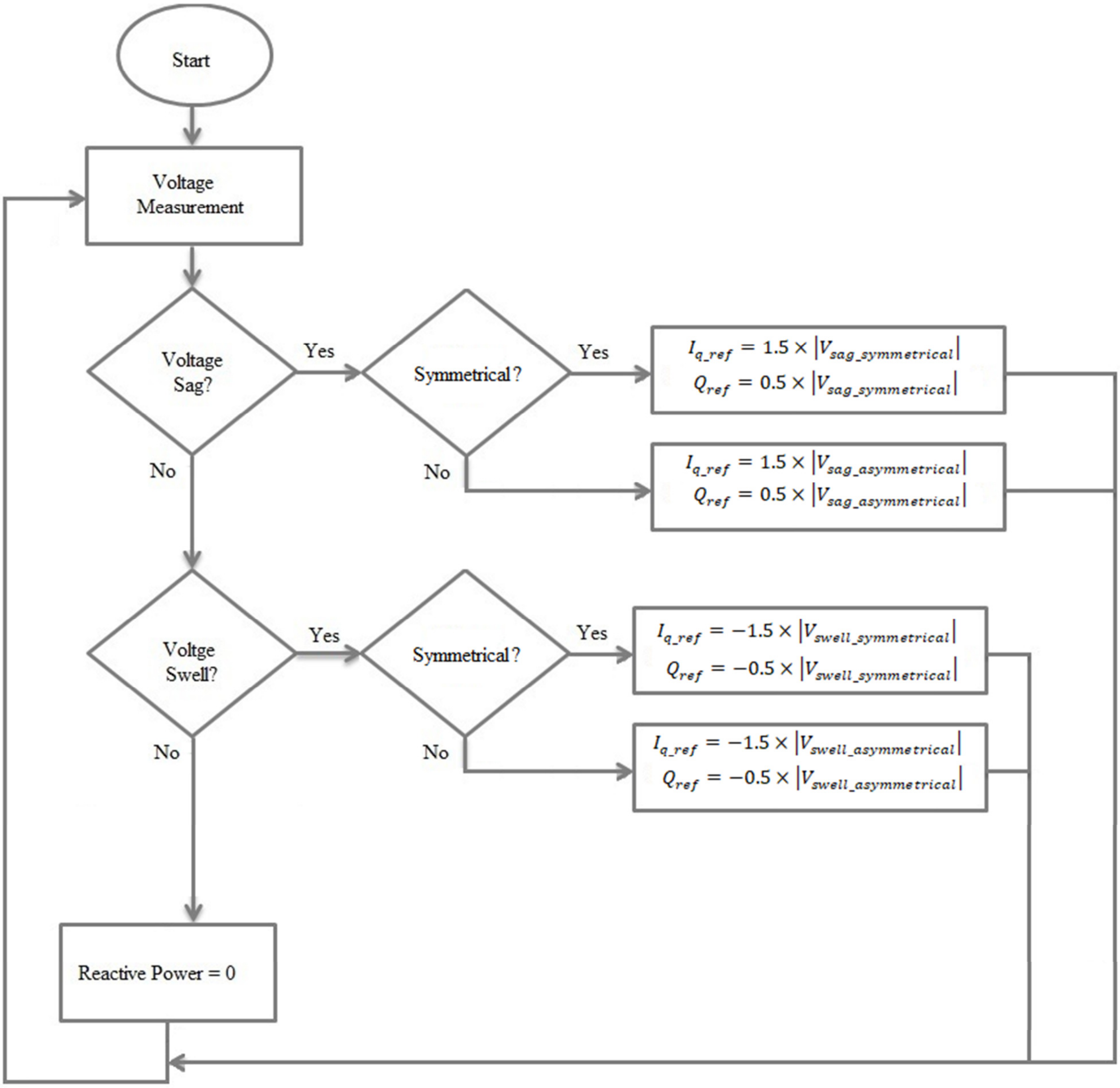

Figure 68: Reactive power management algorithm

A supervisory controller utilizes an algorithm to control the switching of SW1, SW2, SW3 and SW4. It also calculates the amount of reactive current, I_{qr}, that has to be supplied or absorbed from the grid and sends relevant signals to the GSC converter. The reactive power management algorithm calculates Q_{conv} in (120) to reduce the magnitude of grid voltage sag or swell. The q-axis current reference, I_{q_ref}, is changed according to the E.ON grid code during a sag or swell according to (121)-(122) to change V_{q_conv}, which, in turn, changes the value of Q_{conv} accordingly. The rated current of the system is assumed to be 1 p.u. in this paper and hence it is not shown in the equations.

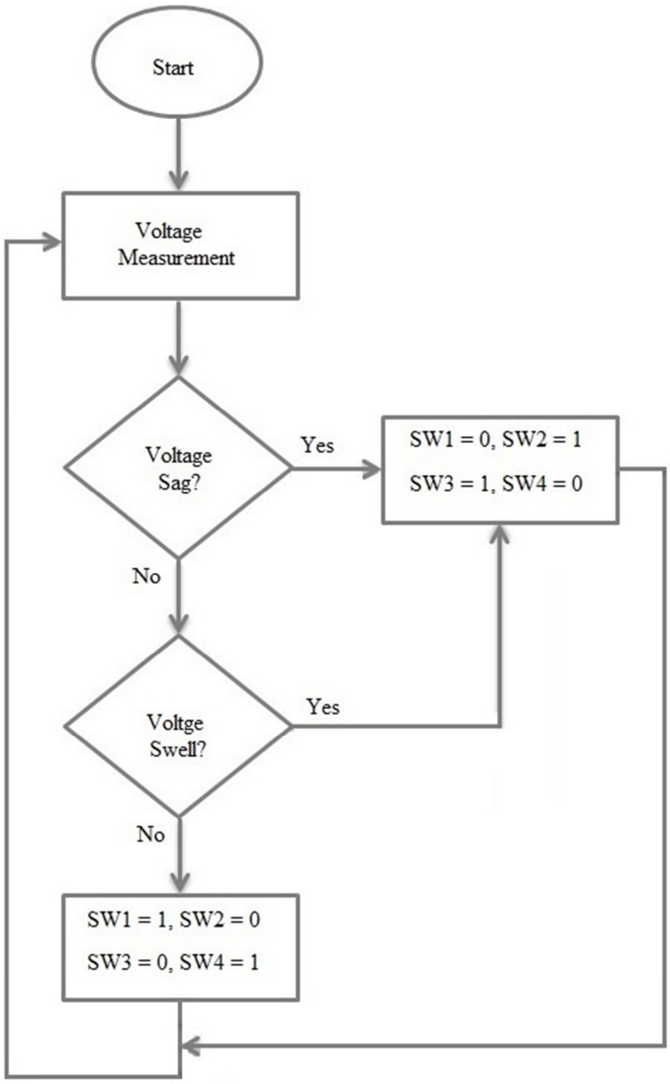

Figure 69: Protection switching algorithm

The d-axis reference current, I_{d_ref}, is connected to the dc-link voltage regulation and is used to keep the standard capacitor voltage of 1150 V. Equations (105)-(106) are used by the controller to set reactive power injection and absorption. V_{q_conv} and V_{d_conv} are q and d-component grid converter voltages correspondingly; I_{d_conv} and I_{q_conv} are d and q-component converter currents correspondingly; R_{RL} and L_{RL} are resistance and inductance of the RL circuit connected with the GSC respectively; K_P and K_I are PI controller constants. Compensation terms are added to V_{q_conv} and V_{d_conv} to decouple dc-link voltage regulation from the reactive power regulation to a certain extent. However, it is found that the reactive power management does affect the magnitude of the dc-link voltage. The RSC reactive power reference Q_{ref} is set according to (124)-(129) to contribute reactive power from the stator. However, in this paper the focus is on the GSC because it has access to large storage of reactive power in the dc-link capacitor while the RSC does not have such storage. Hence, the GSC is found to be more effective in providing reactive power for grid stability.

$$I_{q\_ref} = 1.5 \times |V_{sag}| \tag{124}$$

$$I_{q\_ref} = -1.5 \times |V_{swell\_asymmetrical}| \tag{125}$$

$$V_{q\_conv} = -(I_{q\_ref} - I_q)\left(K_P + \frac{K_I}{s}\right) + V_q - I_{d\_ref}L_{RL}\omega - I_{q\_ref}R_{RL} \tag{126}$$

$$V_{d\_conv} = -(I_{d\_ref} - I_d)\left(K_P + \frac{K_I}{s}\right) + V_d + I_{q\_ref}L_{RL}\omega - I_{d\_ref}R_{RL} \tag{127}$$

$$Q_{ref} = 0.5 \times |V_{sag}| \tag{128}$$

$$Q_{ref} = -0.5 \times |V_{swell\_asymmetrical}| \tag{129}$$

5.3. Simulation study of Type 3 wind generator behaviour

The aggregate wind farm in Fig. 59 uses a cluster representation. For this simulation purpose, the wind farm consists of 6 x 1.5 MW Type 3 wind generators which transfers power to the grid through a 30-km long, 25 kV transmission line. A 120 KV variable voltage source represents the 50 Hz grid. The wind speed is kept unchanged at 15 m/s for convenience. The rotor speed and dc-link voltage are maintained at 1.2 pu and 1150 V respectively. Conventional PI control is used for the control of the RSC and GSC. Traditional protection systems such as the AC crowbar or DC chopper have not been employed. In MATLAB/Simscape Power Systems, the efficacy of the novel integrated ride-through scheme is tested under four scenarios: symmetrical voltage sags, asymmetrical voltage sags, symmetrical voltage swells and asymmetrical voltage swells.

5.3.1. Symmetrical voltage sag performance

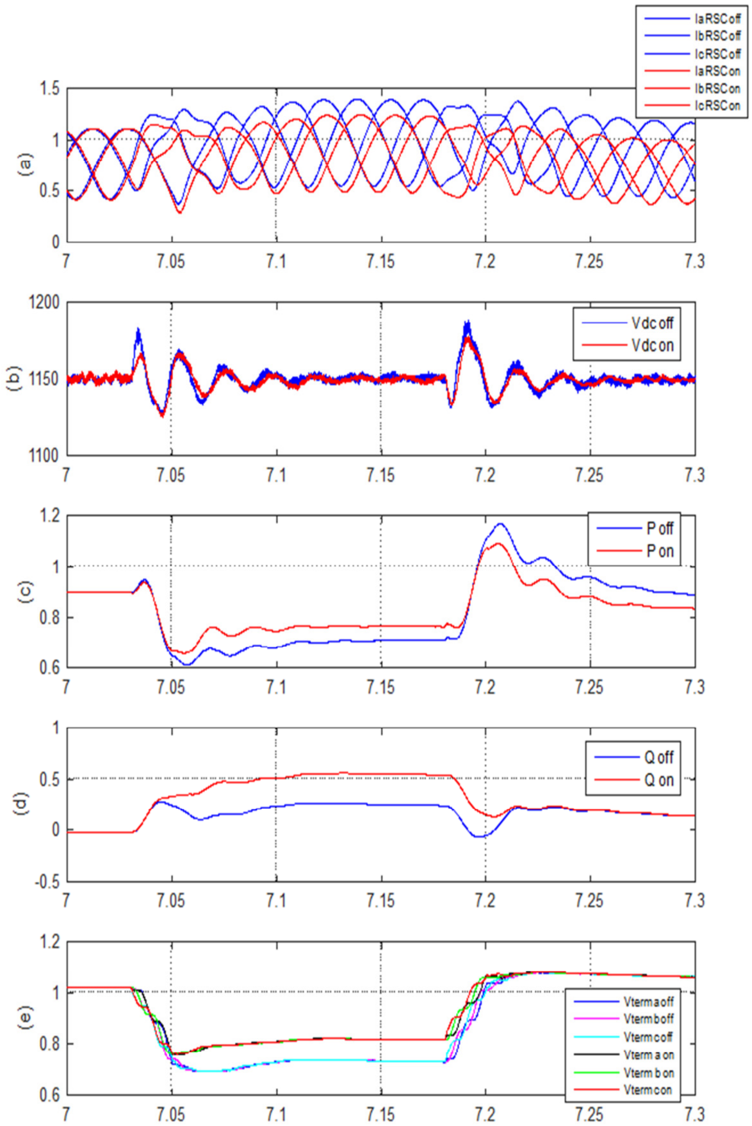

Figure 70: Novel scheme performance for symmetrical sag

The performance of the novel protection and reactive power management scheme is evaluated for a 30% symmetrical voltage sag at PCC. In Fig. 70, the red line represents the behaviour of the DFIG wind generator when the proposed scheme is employed. The related variables are labelled with ‘on’ at the end to represent novel scheme inclusion. Additionally, the blue line represents the DFIG behaviour without the scheme and the related variables are labelled with ‘off’ at the end. It is apparent that the RSC (I_RSC) overcurrent is much lower with the proposed scheme. The overcurrents with and without the scheme are 1.38 pu and 1.25 pu respectively. The dc-link overvoltage (V_dc) with the scheme is 1175 V; while, it is 1187 V without the scheme. Therefore, the dc-link overvoltage is reduced. Active power drops are 0.61 p.u and 0.67 pu with and without scheme respectively. The reactive power supply with the scheme is 0.58 pu; while, it is 0.31 pu without scheme. Hence, The fall of active power is less and the supply of reactive power is increased with the scheme. Consequently, the magnitude of the voltage sag is also reduced to 22% from 30% in all three phases. Overall, the Type 3 wind generator performance is improved.

5.3.2. Asymmetrical voltage sag performance

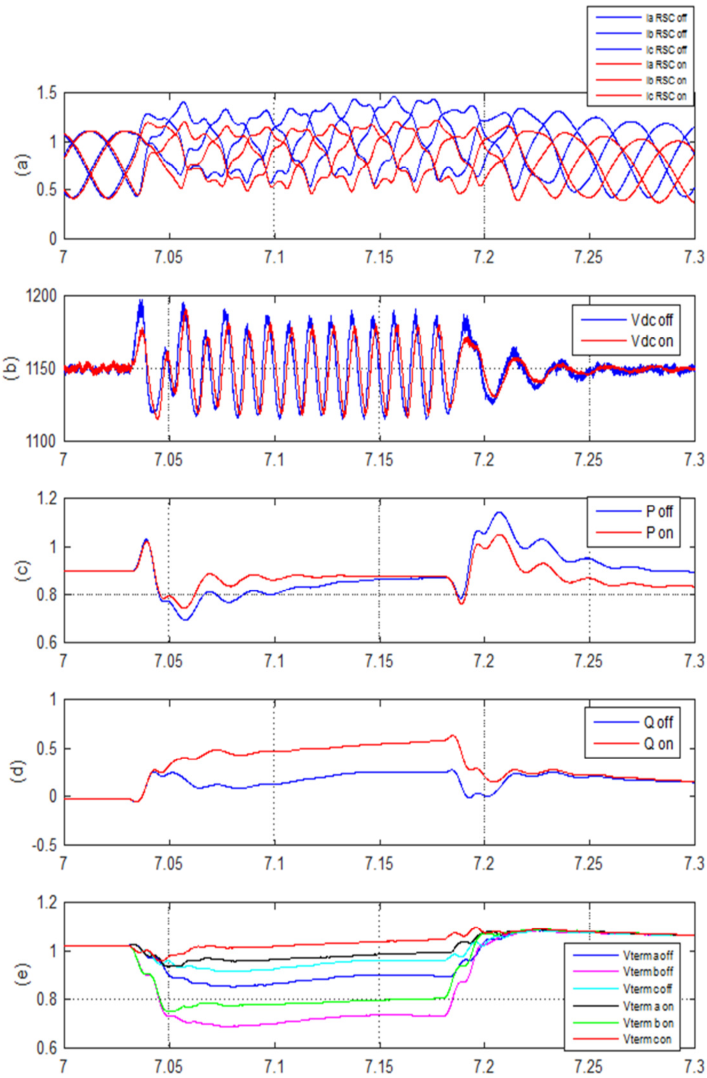

Figure 71: Novel scheme performance for asymmetrical sag

The performance of the novel protection and reactive power management scheme is evaluated for a 30% asymmetrical voltage sag in phase B at PCC. In Fig. 71, it is seen that the RSC overcurrent with the scheme is 1.21 pu; and it is 1.42 pu without scheme. So, the overcurrent is reduced. Moreover, the dc-link overvoltages are 1181 V and 1196.8 V with and without scheme respectively. Therefore, the overvoltage is reduced. Active power drops are 0.75 pu and 0.69 pu with and without scheme correspondingly. The reactive power injection with scheme is 0.66 pu, while it is 0.25 pu without scheme. Hence, the fall of active power is less and the supply of reactive power is increased with the scheme. The magnitude of the voltage sag in phase B is also brought down from 30% to 24%. In conclusion, the overall Type 3 wind generator performance is enhanced.

5.3.3. Symmetrical voltage swell performance

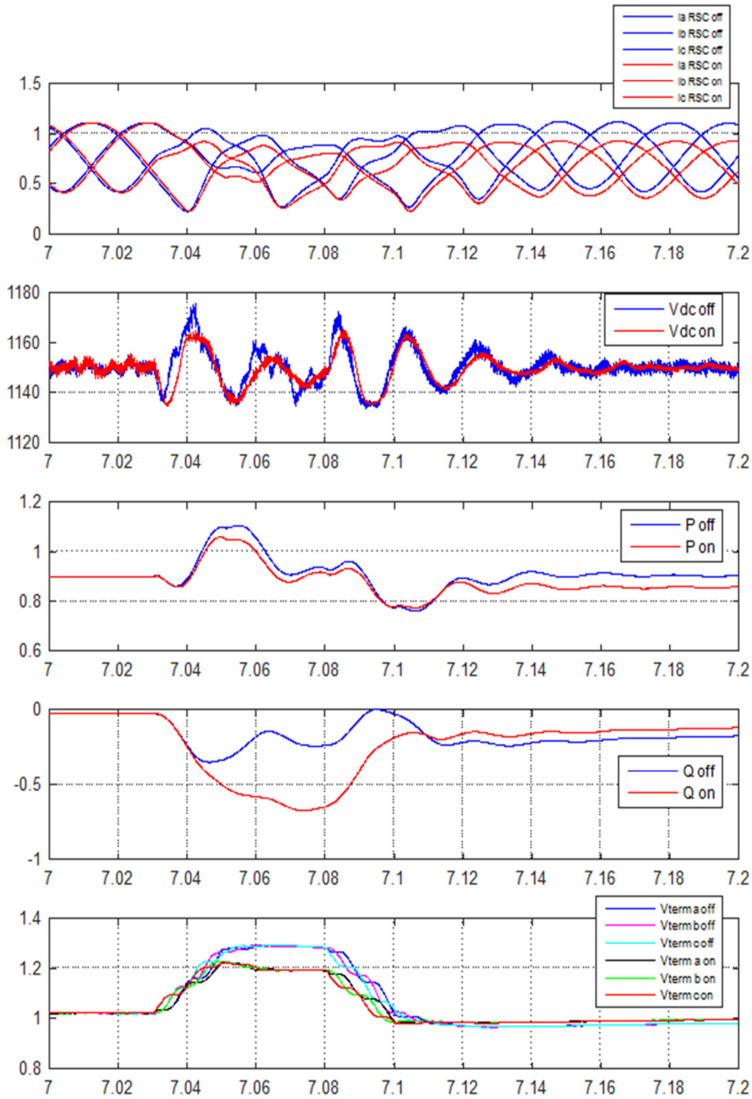

Figure 72: Novel scheme performance for symmetrical swell

The performance of the novel protection and reactive power management scheme is evaluated for a 30% symmetrical voltage swell at PCC. In Fig. 72, it is seen that the RSC overcurrent is 0.75 pu with the scheme; and it is 0.84 pu without scheme. So, the maximum current is decreased. The dc-link overvoltages are 1162 V and 1176 V with and without scheme respectively. Therefore, the overvoltage is lessened. The rise of active power is 1.08 pu with scheme and 1.11 pu without scheme. The reactive power absorptions with and without scheme are 0.69 pu and 0.31 pu correspondingly. Hence, the rise of active power is less and reactive power absorption is higher with the scheme. The magnitude of the voltage swell is also brought down to 21% from 30%. Hence, the overall Type 3 wind generator performance is improved.

5.3.4. Asymmetrical voltage swell performance

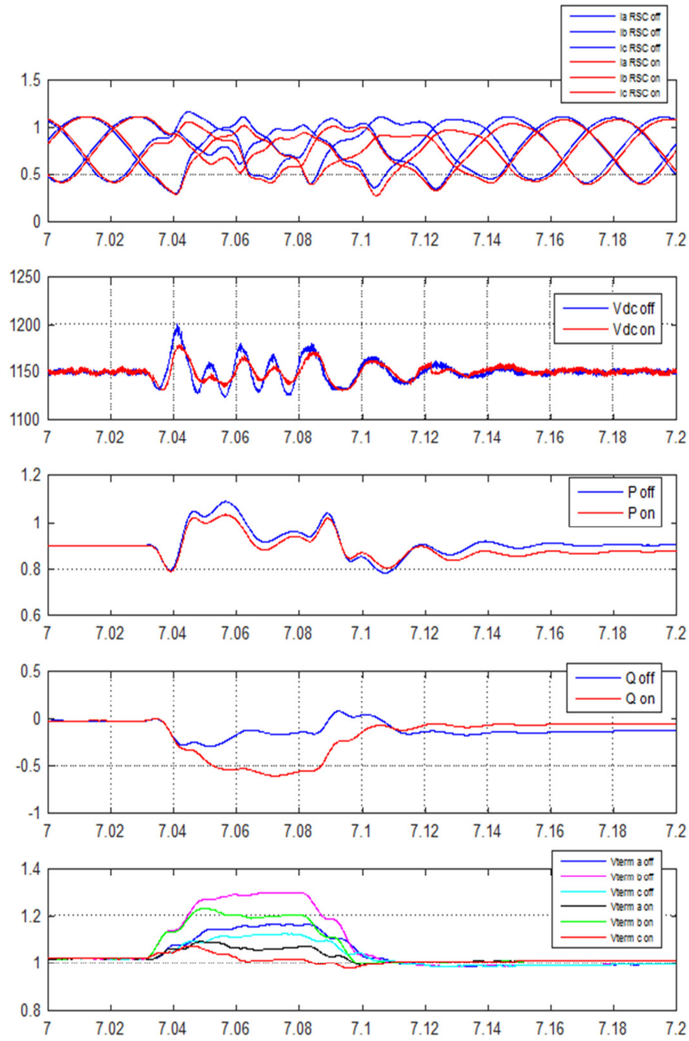

Figure 73: Novel scheme performance for symmetrical swell

The performance of the novel protection and reactive power management scheme is evaluated for a 30% asymmetrical voltage swell in phase B at PCC. In Fig. 73, it is seen that the RSC currents with and without the scheme are 1.16 pu and 1.01 pu correspondingly. So, the current is lower with the scheme. The dc-link overvoltages are 1176 V and 1200 V with and without scheme respectively. Hence, the overvoltage is reduced with the scheme. The rise of active power is 1.03 pu with scheme and 1.11 pu without scheme. Reactive power absorption with the scheme is 0.61 p.u; while, it is 0.29 pu without scheme. Therefore, the rise of active power is less and absorption of reactive power is higher with the scheme. The magnitude of the voltage swell in phase B is reduced to 22% from 30%. Overall, Type 3 wind generator performance is enhanced.

5.4. Summary

A novel coordinated ride-through scheme is designed for Type 3 WGs to deal with grid voltage fluctuations. The scheme is divided into two parts: a protection system and a reactive power management system. The function of the protection system is to limit the RSC overcurrent and dc-link overvoltage to a reasonable limit. There is a feature in the protection system to feed the additional energy back into the grid. This increases the efficiency of the entire system by minimizing energy loss. On the other hand, the reactive power management scheme supplies the grid with reactive power from the wind generator converter during a sag event and absorbs reactive power during a swell event. It is observed that the novel ride-through scheme greatly improves the performance of Type 3 WGs during symmetrical and asymmetrical voltage sags, and symmetrical and asymmetrical voltage swells. The scheme also helps in maintaining a stable grid through effective reactive power management between the converter and grid. This scheme is more comprehensive because it provides protection during four different types of grid voltage fluctuation.

Chapter 6

Ride-through Performance Enhancement of Type 4 Wind Farms

6.1. Introduction

The need for an extensive ride-through strategy for Type 4 WGs has been well explained in the literature review. The full convertibility of power in Type 4 WGs is an attractive feature for more efficient renewable energy integration in the grid. That is why it is essential to ensure safe and reliable operation of Type 4 WGs under grid voltage disturbances. The ride-through strategy should also contribute to grid stabilization through efficient reactive power management. This chapter presents a novel ride-through strategy that augments Type 4 wind farm performance in the event of grid voltage fluctuations and supports grid stability through appropriate regulation of reactive power. To improve dc-voltage regulation, a neural network predictive controller (NNPC) is designed for rotor speed control. There are two steps involved in this, namely, system identification and control design.

6.2. Type 4 wind farm performance enhancement strategy

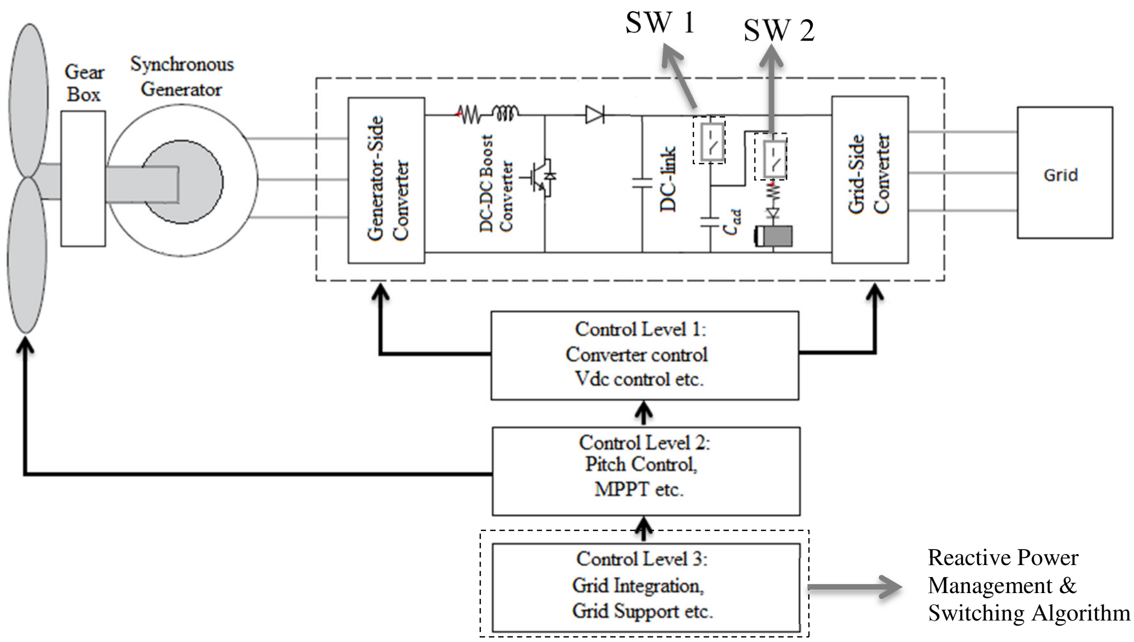

Figure 74: Type 4 wind generator novel protection scheme

A novel coordinated ride-through strategy is proposed for Type 4 wind systems to augment their operation during voltage fluctuations. Both symmetrical and asymmetrical voltage transients are considered in the design of the scheme. The strategy includes a safety scheme and a reactive power regulation scheme. The protection arrangement is given in Fig.

68. It includes a parallel arrangement of a NiMH battery and a supplementary capacitor, C_{ad}. The battery comprises 100 cells in series and its discharge characteristic is given in Fig. 75. A parallel capacitor based ride-through strategy has been utilized for Type 3 wind generators but without any power storage capacity [50]. A diode and a resistor are connected in series with the battery. The insertion of the extra capacitor and battery are regulated using switches SW1 and SW2 with the help of a supervisory (Level 3) controller. In steady state, SW1 stays open and SW2 stays closed. When voltage fluctuations occur, SW1 is closed and SW2 is opened by the supervisory controller. This inserts the capacitor C_{ad} in parallel with the dc-link capacitor, thereby increasing the total capacitance, C_{Total}, in (130). Although, the value of E_c goes up in (131), V_c stays within acceptable limits because the total capacitance increased. Hence, the converter is protected from any damage. Upon clearance of the voltage sag or swell, SW1 is opened and SW2 is closed by the supervisory controller. This enables the additional capacitor to discharge completely into the battery. Current spikes are resulting from switching is prevented by the series resistor. A diode is utilized to make sure that no energy gets transferred from the capacitor thereby discharging it. The energy accumulated in the battery is then fed back into the grid.

$$C_{Total} = C_{dc-link} + C_{additional} \tag{130}$$

$$V_c = \sqrt{\frac{2E_c}{C_{Total}}} \tag{131}$$

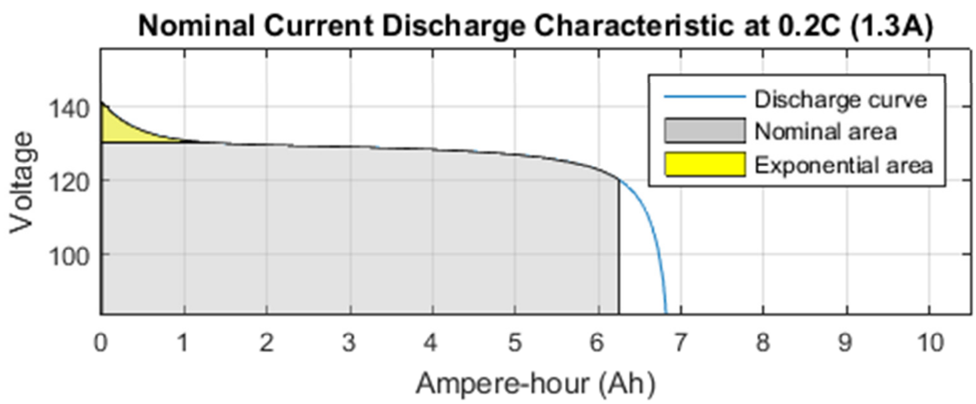

Figure 75: Discharge characteristics of Nickel-Metal-Hydride battery

The supervisory controller (level 3 control) calculates the reactive current reference, I_{qr}, that has to be injected or consumed from the grid by the grid-side converter. The reactive power management algorithm shown in Fig. 76 calculates Q_{conv} in (132) to decrease the extent of PCC voltage sag or swell. The q-component of reference current, I_{q_ref}, is calculated according to a modified E.ON grid code during a sag or swell following (133)-(134) to change V_{q_conv}, which, in turn, sets the desired value of Q_{conv}. The E.ON grid code is modified for asymmetrical sags and swells because a higher quantity of reactive power supply for asymmetrical voltage sags can lead to voltage swells; and a higher absorption for asymmetrical voltage swells can cause voltage sags. The d-component of reference current, I_{d_ref}, is implemented for the dc-link voltage control and it maintains a voltage of 1100 V. The supervisory control system uses (135)-(136) to calculate the required reactive power. V_{d_conv} and V_{q_conv} are q and d-components of grid converter voltages respectively; I_{d_grid} and I_{q_grid} are d and q-components of converter currents respectively; R_{RL} and L_{RL} represent the resistance and inductance of the resistive-inductive circuit connected to the GSC respectively; K_p and K_i are the constants of PI control. Compensation terms are included in the output of the current regulators to decouple the dc-link voltage and reactive power regulations. Nevertheless, the reactive power regulation does have an impact on the dc-link voltage regulation.

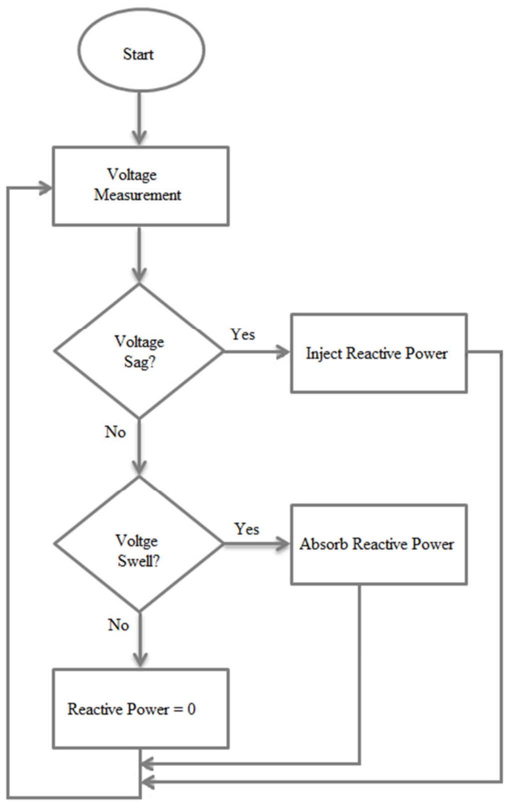

(i)

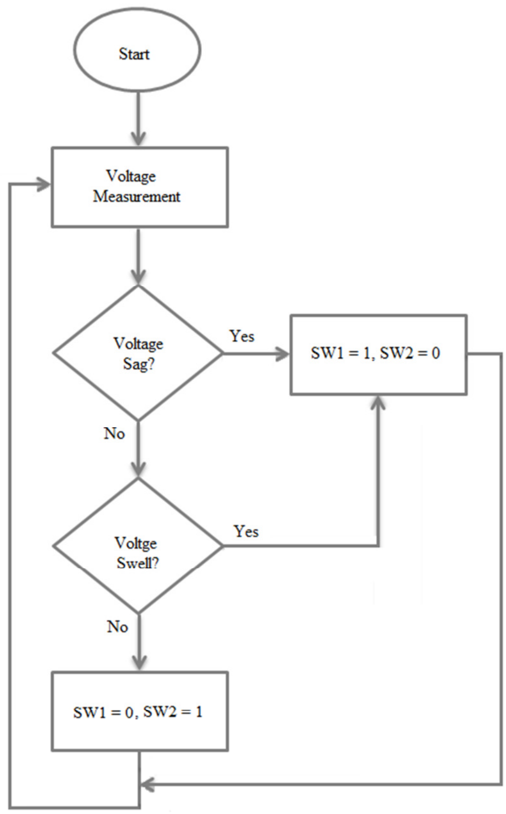

(ii)

Figure 76: (i) Reactive power management algorithm, (ii) Switching algorithm

$$Q_{conv} = V_{q\_conv}I_{d\_conv} - V_{d\_conv}I_{q\_conv} \tag{132}$$

$$I_{q\_grid\_ref} = 2 \times |V_{sym\_sag}| \text{ or, } 1 \times |V_{asym\_sag}| \tag{133}$$

$$I_{q\_grid\_ref} = -2 \times |V_{sym\_swell}| \text{ or, } -1 \times |V_{asym\_swell}| \tag{134}$$

$$V_{d\_conv} = -(I_{d\_grid\_ref} - I_{d\_grid})\left(K_p + K_i \int dt\right) + V_d + I_{q\_grid\_ref}L_{RL}\omega - I_{d\_grid\_ref}R_{RL} \tag{135}$$

$$V_{q\_conv} = -(I_{q\_grid\_ref} - I_{q\_grid})\left(K_p + K_i \int dt\right) + V_q - I_{d\_grid\_ref}L_{RL}\omega - I_{q\_grid\_ref}R_{RL} \tag{136}$$

The nonlinear mechanical system of the wind generator is approximated using a neural network model as shown in Fig. 77, where y_p and y_m are plant and neural network model outputs respectively and u is the control input. The Levenberg-Marquardt training algorithm is chosen for this paper.

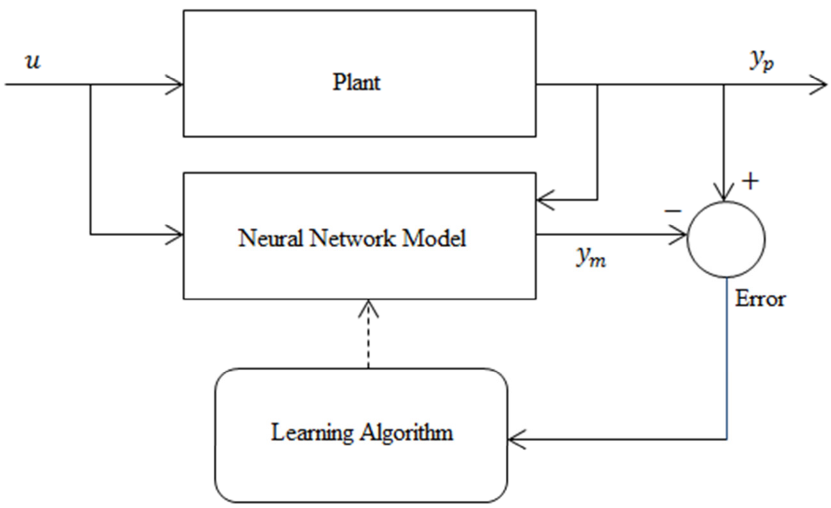

Figure 77: System identification

The receding horizon technique is utilized for the predictive controller where the response of the plant is predicted over a definite time horizon. An optimization algorithm that calculates the desired control input by minimizing the performance criterion, J, given in (137). The horizons over which the control increments and tracking error are calculated are represented by n_1, n_2 and n_u. y_r and y_m are the desired and network model responses respectively, while u' is the tentative control signal. The value of ρ is used to adjust weighting on control increments in the performance inject J [116]. The complete architecture of the Type 4 WG control system is shown in Fig. 78 and Fig. 79. It shows how the NNPC fits in the overall control architecture.

$$J = \sum_{j=n_1}^{n_2} (y_r(k+j) - y_m(k+j))^2 + \rho \sum_{j=1}^{n_u} (u'(k+j-1) - u'(k+j-2))^2 \quad (137)$$

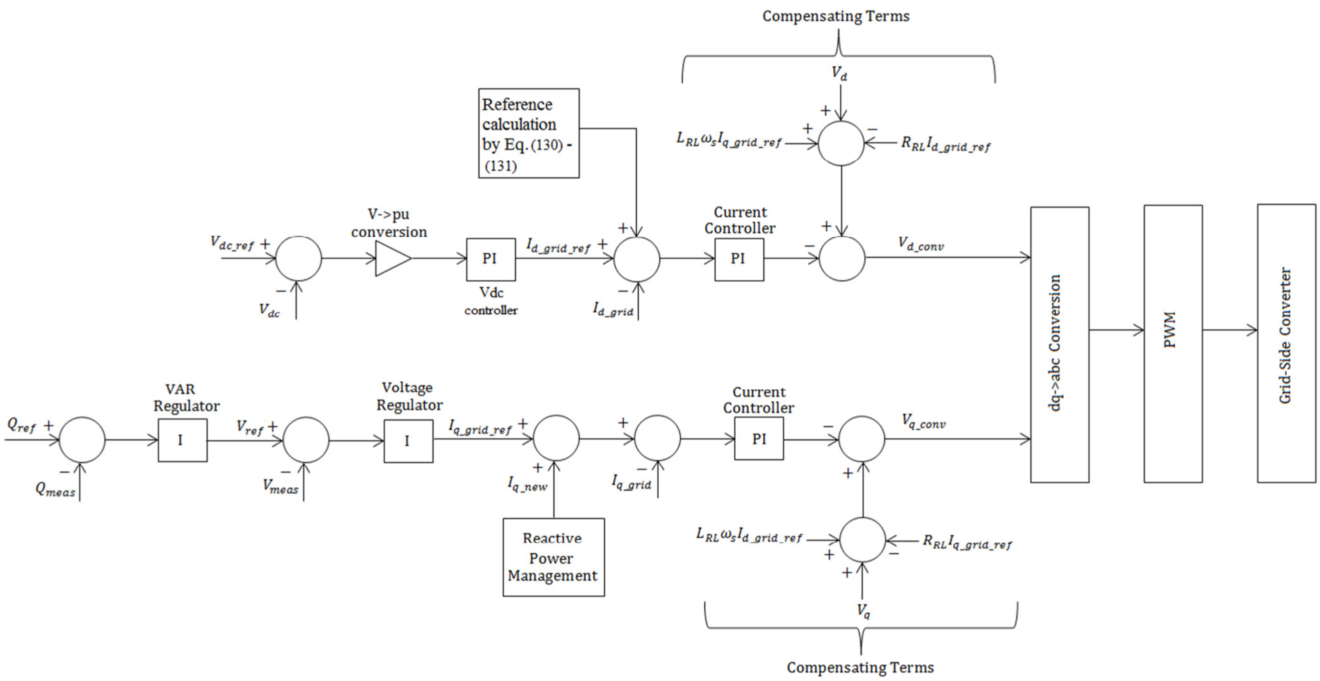

Figure 78: Architecture of grid side control

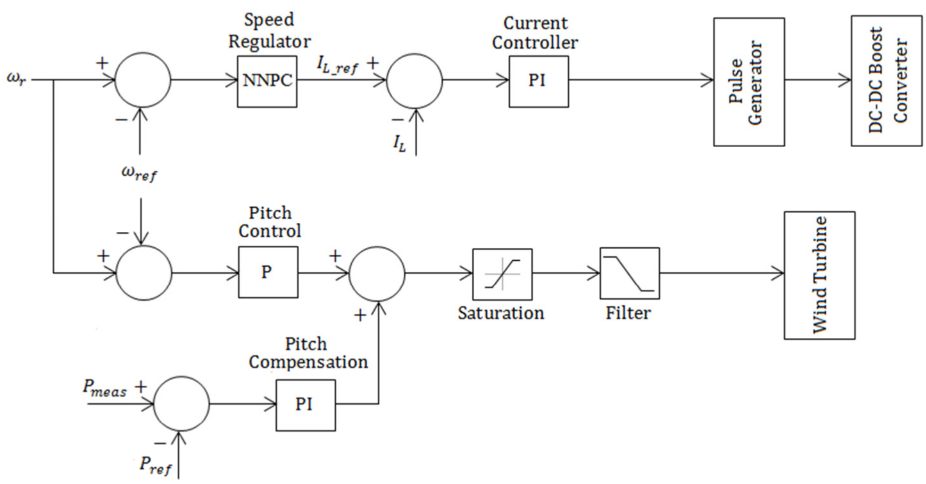

Figure 79: NNPC implementation

6.3. Simulation study of Type 4 wind generator behaviour

The aggregate wind farm in Fig. 59 consists of 5 x 2 MW Type 4 wind generators for the purpose of simulation. The farm transmits energy to the electric grid with the help of a 25 kV transmission line (30 km). A 120 KV variable voltage source symbolizes the grid of 50 Hz frequency. The wind speed is maintained at a constant value of 15 m/s. The dc-link voltage is set at 1100 V in steady state. Proportional-Integral control is implemented for the regulation of the converters. In MATLAB/Simscape Power Systems, the validity of the performance enhancement scheme is evaluated in the following scenarios: symmetrical and asymmetrical voltage sags; symmetrical and asymmetrical voltage swells. The advantage of NNPC over PI is also demonstrated.

6.3.1. Symmetrical voltage sag performance

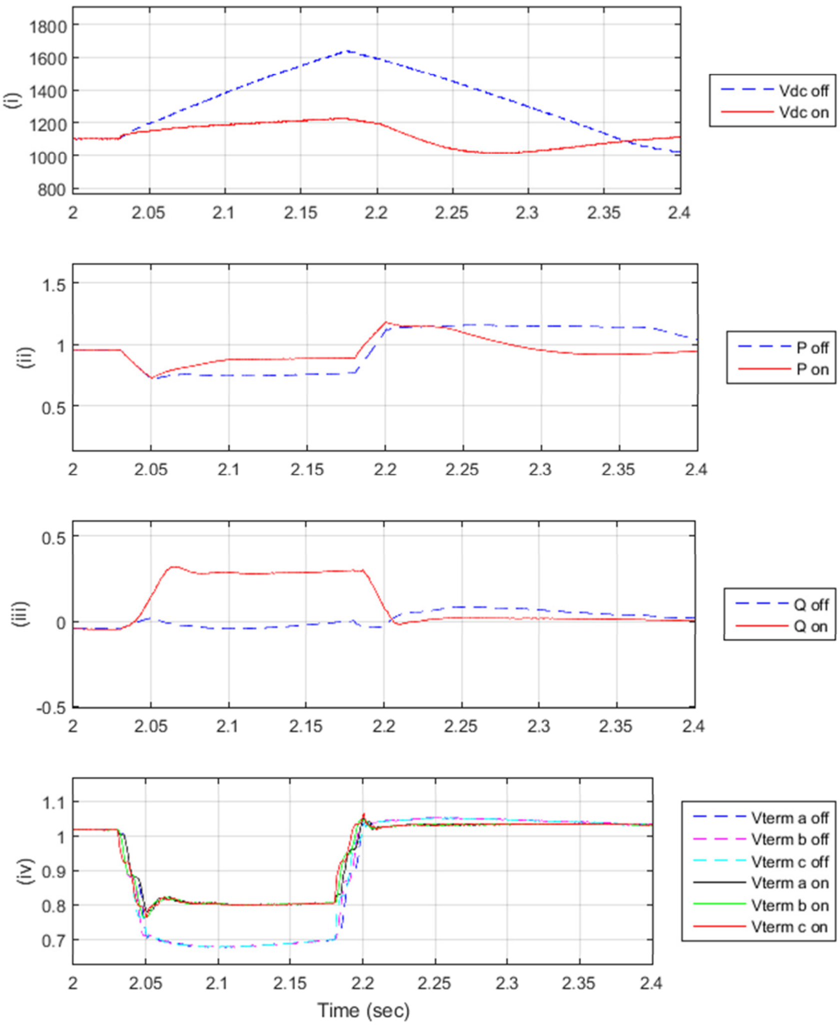

Figure 80: Type 4 wind generator response for 30% symmetrical voltage sag. (i) DC-link voltage (V). (ii) Active power (p.u.). (iii) Reactive power (p.u.). (iv) Terminal voltage (p.u.).

In Fig. 80, the behaviour of Type 4 wind generators during a 30% PCC symmetrical voltage sag which lasts for 150 ms is shown with and without the novel performance augmentation strategy. Henceforth, the wind generator behaviour without the proposed strategy will be called the OFF mode, whereas the wind generator behaviour with the performance augmentation strategy will be referred to as the ON mode. The OFF and ON mode dc-link overvoltages are 1638 V and 1229 V respectively. Therefore, the novel strategy protects the converter from any damage. The supply of active power is higher in the ON mode which peaks at 0.882 p.u. compared to 0.751 p.u. in the OFF mode. Also, there is greater reactive power supply in the ON mode at 0.279 p.u., while it is kept at 0 in the OFF mode. Consequently, the magnitude of voltage sag is reduced to 0.80 p.u. in the ON mode from the OFF mode value of 0.68 p.u.

6.3.2. Asymmetrical voltage sag performance

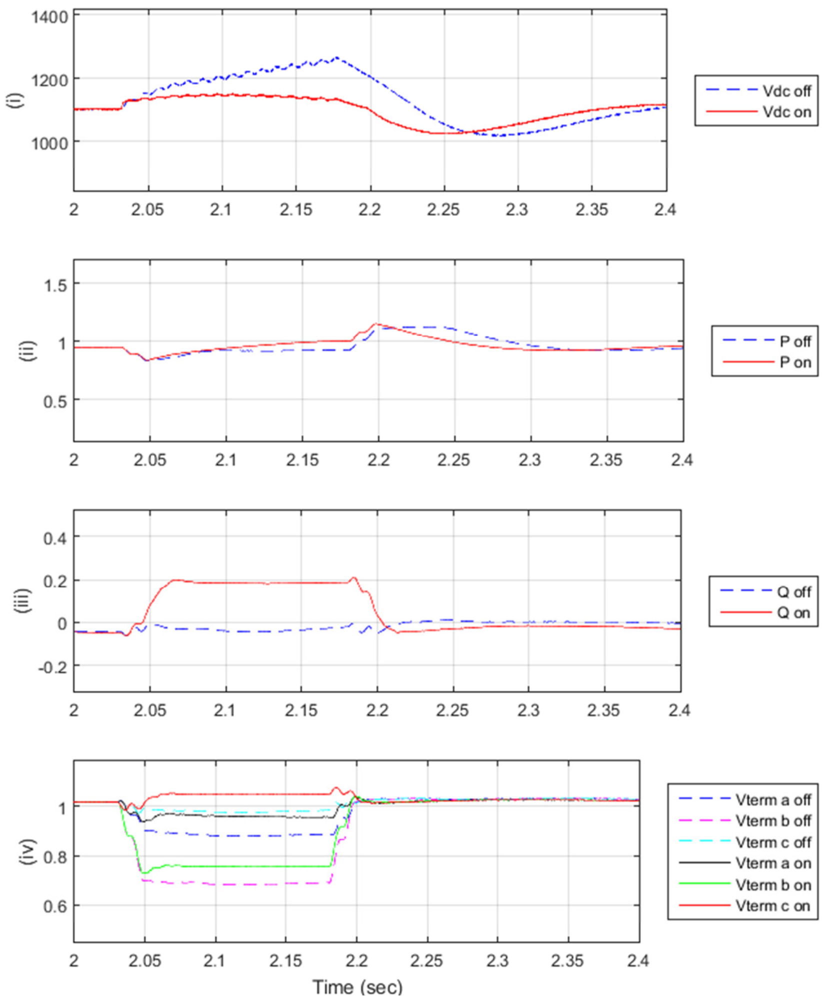

Figure 81: Type 4 wind generator response for 30% asymmetrical voltage sag. (i) DC-link voltage (V). (ii) Active power (p.u.). (iii) Reactive power (p.u.). (iv) Terminal voltage (p.u.).

The performance of the novel protection and reactive power management scheme is evaluated for a 30% asymmetrical voltage sag in phase B at PCC. In Fig. 81, the dc-link overvoltage with the scheme is 1127 V, while it is 1286 V without the scheme. Therefore, the dc-link overvoltage is reduced considerably. Active power drops to 0.87 p.u with and without the scheme. However, the recovery of active power to acceptable levels happens much faster with the scheme. The reactive power supply with the scheme is 0.41 pu; while, it is 0.02 pu without scheme. Hence, the overall fall of active power is less and the supply of reactive power is raised with the scheme. Consequently, the magnitude of the voltage sag is also reduced to 22% from 30% in all three phases. Overall, the Type 4 wind generator performance is enhanced.

6.3.3. Symmetrical voltage swell performance

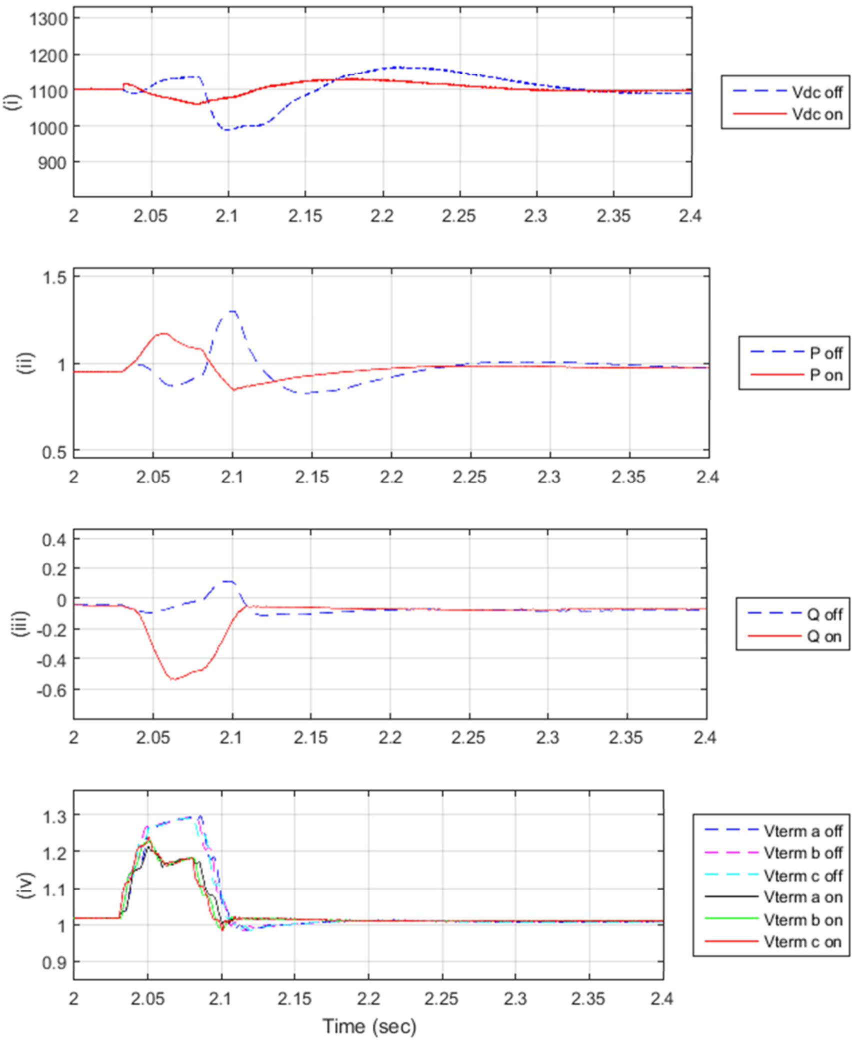

Figure 82: Type 4 wind generator response for 30% symmetrical voltage swell. (i) DC-link voltage (V). (ii) Active power (p.u.). (iii) Reactive power (p.u.). (iv) Terminal voltage (p.u.).

The performance of the novel protection and reactive power management scheme is evaluated for a 30% symmetrical voltage swell at PCC. In Fig. 82, the dc-link undervoltage with the scheme is 1042 V, while it is 976 V without the scheme. Therefore, the dc-link undervoltage is reduced considerably. An undervoltage will affect the performance of the wind generator adversely. Active power increments are 1.19 p.u and 1.40 pu with and without the scheme correspondingly. The reactive power absorption with the scheme is 0.50 pu; while, it is 0.09 pu without scheme. Hence, the rise of active power is less and the absorption of reactive power is raised with the scheme. Consequently, the magnitude of the voltage swell is also decreased to 22% from 30% in all three phases. Overall, the Type 4 wind generator performance is enhanced.

6.3.4. Asymmetrical voltage swell performance

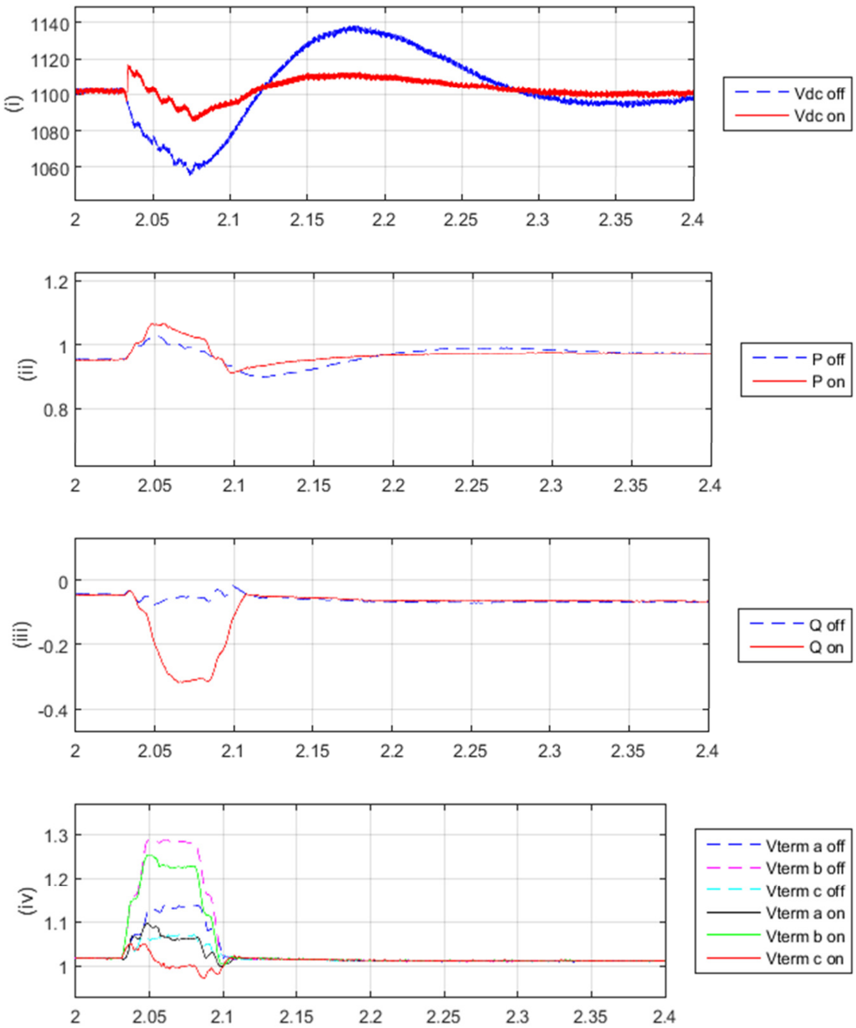

Figure 83: Type 4 wind generator response results for 30% asymmetrical voltage. (i) DC-link voltage (V). (ii) Active power (p.u.). (iii) Reactive power (p.u.). (iv) Terminal voltage (p.u.).

In Fig. 83, the behaviour of Type 4 wind generator during a 30% PCC asymmetrical voltage swell lasting for 50 ms is shown with and without the performance augmentation strategy. The dc-link undervoltages are 1056 V and 1086 V for OFF and ON modes in that order. Hence, ON mode is closer to the steady-state value of 1100 V. Also, the post-swell return to steady state is faster in ON mode. The ON mode active power injection is 1.065 p.u. while it is 1.026 p.u. in OFF mode. Furthermore, the reactive power absorption is -0.314 p.u. in ON mode compared to 0 p.u. in OFF mode. This augments the PCC voltage by reducing the voltage swell to 1.223 p.u. in ON mode from 1.283 p.u. in OFF mode.

6.3.5. NNPC performance evaluation

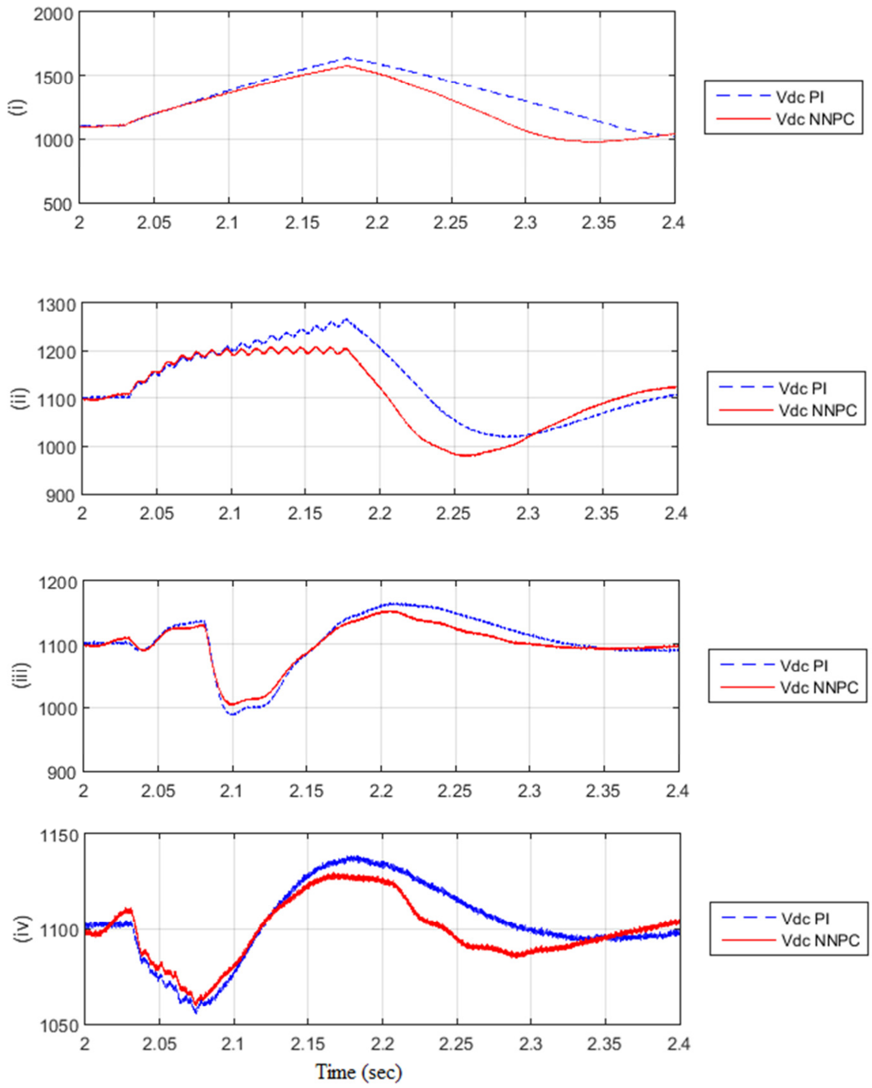

Figure 84: Performance of NNPC and PI for different PCC voltage scenarios. (i) DC-link voltage at 30% symmetrical sag (V). (ii) DC-link voltage at 30% asymmetrical sag (V). (iii) DC-link voltage at 30% symmetrical swell (V). (iv) DC-link voltage at 30% asymmetrical swell (V).

In Fig. 84, the performance of the PI and NNPC in terms of dc-link voltage regulation is shown under a voltage sag at PCC. In this case, the reactive power management and the protection system are turned off to isolate the performance of the PI and NNPC. For a 30% symmetrical sag, the dc-link overvoltage is 1638 V for PI and 1577 V for NNPC. Similarly, the overvoltages are 1267 V and 1207 V for PI and NNPC in that order for a 30% asymmetrical voltage sag. In case of a 30% voltage swell, the undervoltages for PI and NNPC are 934.1 V and 951.9 V respectively, while the overvoltages are 1178 V and 1165 V for PI and NNPC in that order. Lastly, for a 30% asymmetrical voltage swell, the PI and NNPC undervoltages are 1038 V and 1046 V respectively, whereas the respective overvoltages are 1145 V and 1137 V. Thus, it is apparent that the NNPC provides far more efficient dc-link voltage regulation than PI.

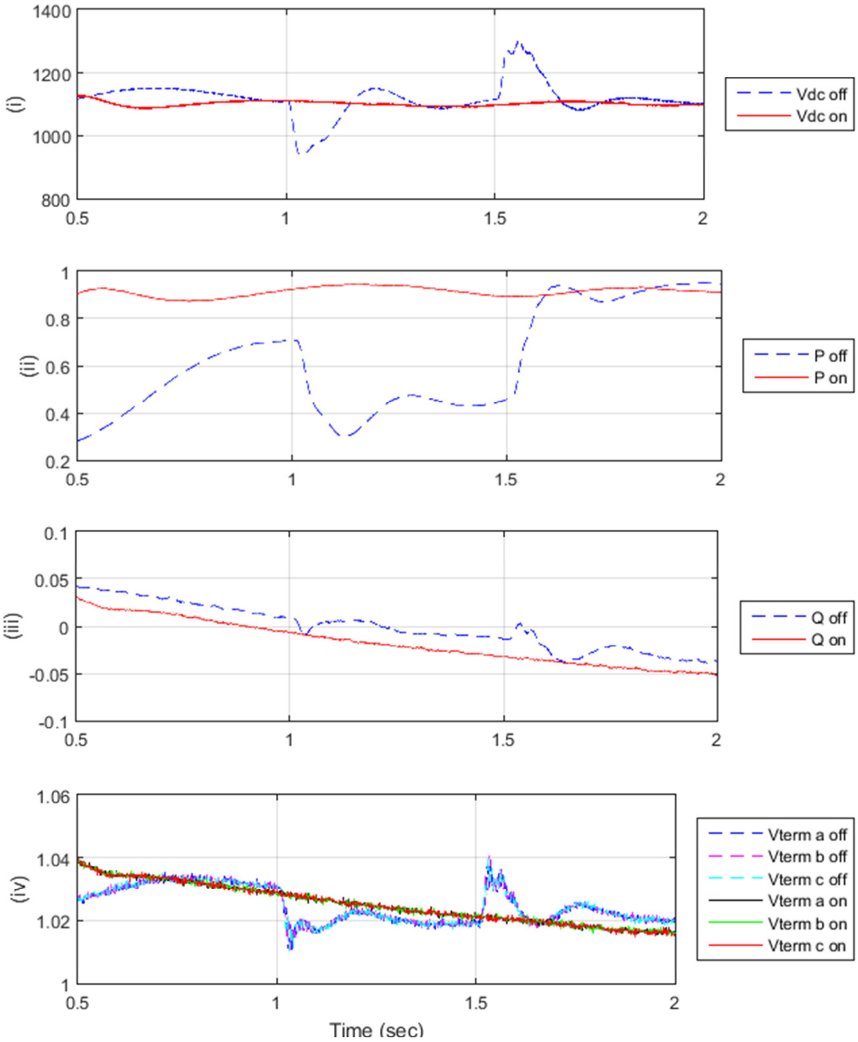

Figure 85: Type 4 wind generator simulation results for output disturbance at the mechanical system. (i) DC-link voltage (V). (ii) Active power (p.u.). (iii) Reactive power (p.u.). (iv) Terminal voltage (p.u.).

In Fig. 85, the response of the Type 4 wind generator to a disturbance in the mechanical system is shown. The reactive power management and the protection system are turned off to isolate the performance of the PI and NNPC. A step disturbance signal of magnitude 0.1 is added to the rotor speed at 1s and it steps down to zero at 1.5s. The dc-link voltage stays steady for NNPC but fluctuates between 936.6V and 1300V for PI. In case of NNPC, both active power and terminal voltage are kept at constant values of 0.9275V and 1.023 pu respectively. However, these variables show oscillatory behaviour for PI. The behaviour of reactive power is similar for both controllers but some oscillation is observed for PI control. Hence, it can be said that NNPC has the added functionality of improved wind generator performance when the mechanical system is subjected to disturbance.

6.4. Summary

An advanced integrated ride-through strategy is designed for Type 4 WGs to counter the adverse effects of grid voltage disturbances. This strategy is also split into two parts, namely a safety scheme and a reactive power management scheme. The purpose of the safety scheme is to maintain the dc-link overvoltage within a tolerable limit. This ensures that the full-scale converter is not destroyed during grid voltage events. The reactive power management scheme controls the flow of reactive power between the grid and converter. During a sag, the flow of reactive power is from the converter into the grid, while it is from the grid to the converter during a swell. This helps maintain grid voltage stability. A neural network predictive controller is implemented for rotor speed control instead of a PI controller, which leads to a more efficient dc-link voltage regulation. Additionally, the neural network predictive controller improves the wind generator response to a disturbance to the mechanical system. The addition of this advanced controller further improves the reliability of the entire system. It is seen that the advanced ride-through strategy noticeably enhances the operation of Type 4 WGs grid voltage fluctuations. The voltage fluctuations include symmetrical and asymmetrical voltage sags, and symmetrical and asymmetrical voltage swells. Grid voltage stability is also strengthened by the appropriate management of reactive power.

Chapter 7

Conclusion and Future Work

7.1. Conclusion

This is a fact that the future of power generation is renewable power generation. This means the overall contribution of wind power as a major source of electricity generation will rise rapidly in the coming years. The variable nature of wind energy due to the intermittent behaviour of wind speed impacts the reliability of grid operation. Consequently, there are many challenges that have to be faced for the stable operation of electricity grids. Some of the challenges include voltage fluctuations, frequency variations, power imbalance due to a mismatch between generation and load demand, additional energy storage requirements etc. The technology used in wind generators is also different and more advanced than that in conventional generators due to the fact that partial-scale or full-scale converters have to be utilized for power conversion. This can affect power system dynamics because it is mainly dependent on the type of generators. It is of utmost importance that grid stability does not get compromised due to the massive integration of wind turbines. This thesis focuses on the impact of grid voltage fluctuations on Type 3 and Type 4 wind generators and the design of novel solutions to counter the adverse effects caused by voltage fluctuations.

Firstly, this thesis conducts an extensive literature review of low-voltage ride-through and high-voltage ride-through solutions developed for Type 3 and Type 4 wind generator systems. The solutions proposed for Type 3 WGs can be divided into three types. The first type involves the design and implementation of advanced controllers in the current loop of the Type 3 control architecture. Conventionally, PI controllers are used for this purpose. The literature review provides description of the controller design and their application within the vector control scheme. Internal Model Control (IMC), proportional resonant (PR), hysteresis control, sliding mode control, linear quadratic (LQ), proportional integral resonant (PIR), fuzzy control, genetic algorithm, model predictive control (MPC) and resonant control are some of the advanced control techniques investigated in the literature review. The second type of ride-through solution for Type 3 WG considers rearrangement of the traditional vector control scheme. It is found that the most common rearrangement is to create novel current reference generation strategies. Sequence decomposition is often used in the new current generation techniques. Some other rearrangement techniques used are flux manipulation, additional feed-forward terms, demagnetizing current, virtual resistance and kinetic energy storage. Flux manipulation is utilized to compensate for the flux offset induced by voltage sags, whereas additional feed-forward terms include extra terms in the current loop of the control algorithm. Demagnetizing current can act in opposite direction of the stator natural flux to decrease its impact on the rotor. Virtual resistance contains a partial feedback term in the inner loop current control which is seen as series resistance with the Type 3 WG rotor. The storage of kinetic energy is done by converting the power imbalance during voltage sags into kinetic energy of wind turbines, and this is performed by increasing the rotor speed.

Finally, the third type of ride-through solution for Type 3 WG is hardware-based where specialized hardware is installed for improved performance. Hardware used for this purpose can have either shunt or series topology. The most common hardware of shunt topology is the dc-link chopper, it is used to protect the dc-link capacitor from overvoltages. Some pieces of hardware used in the series topology are series dynamic resistor (SDR), series dynamic braking resistor (SDBR) and modulated series dynamic braking resistor (MSDBR). Current limiting hardware such as bridge-type fault current limiter (BTFCL), switch-type fault current limiter (STFCL) and superconducting fault current limiter (SFCL) are also implemented for performance enhancement. Electric doubly layer capacitors are utilized as energy storage device (ESD) which regulates the dc-link capacitor voltage during grid voltage fluctuations. In the works described above, none of the solutions deals with all aspects of grid voltage fluctuations i.e., symmetrical and asymmetrical voltage sags, and symmetrical and asymmetrical voltage swells. Therefore, all of these solutions are partial in nature. Moreover, very few have any reactive power support capability to augment grid stability during voltage fluctuations. Hence, there is a need for a comprehensive ride-through solution for Type 3 WGs which can counter all types of grid voltage fluctuations and simultaneously stabilize the grid.

The ride-through solutions for Type 4 WGs are also classified into three types. The first type of solution for Type 4 WG includes the implementation of advanced control primarily in the current loop. Feedback linearization control, sliding mode control, linear quadratic regulation (LQR), fuzzy logic control, nonlinear adaptive control, predictive control, model predictive control (MPC) are some of the control methods implemented for enhanced operation of Type 4 WG under grid voltage fluctuations. The second type of solution includes rearrangement of the traditional vector control scheme. Some of the rearrangement techniques are described hereafter. An active damping technique is used where a band-pass filter dampens the natural frequency response of the wind generator. The generator-side and grid-side converter control is harmonized using a unified dc-link control, whereas the generator-side converter regulated the dc-link voltage and the grid-side controls the power flow between the grid and converter in the unified power control technique. Storage of additional kinetic energy as inertia of the wind turbine is utilized by increasing the rotor speed. This is also done by rearranging the vector control scheme. Novel current reference generation techniques are also employed for Type 4 WG performance improvement. The third type of solution involves installing specialized hardware. An energy storage system (ESS) technique is implemented for the regulation of the dc-link voltage. Electromagnetic braking is exploited in a dc-chopper based strategy where the excess energy is dissipated. Cascaded current source converters (CSCs) are installed in a strategy on the generator and grid sides. Similar to the solutions for Type 3 WG, none of the solutions above deals with all aspects of grid voltage fluctuations i.e., symmetrical and asymmetrical voltage sags, and symmetrical and asymmetrical voltage swells. Hence, all of these are partial solutions in terms of efficient ride-through. Furthermore, very few have any reactive power support to strengthen grid stability during voltage fluctuations. Consequently, there is a requirement for a complete ride-through solution for Type 4 WGs which can deal with all types of grid voltage fluctuations and simultaneously maintain grid stability.

An analysis on the impact of grid voltage fluctuations on Type 3 and Type 4 wind generators is conducted. Grid voltage fluctuation influences stator magnetic flux which, in turn, imposes a voltage on the rotor of the generator. This imposed voltage leads to damaging overcurrents in the RSC of Type 4 WGs. Symmetrical and asymmetrical voltage sags have different effects on the generator. The other adverse effect of grid voltage fluctuation is overvoltages in the dc-link capacitor of Type 3 and Type 4 WGs. These overvoltages can destroy the converter and impact normal operation of the wind generators. Comparative study shows that asymmetrical voltage sags and swells cause more damage to Type 3 WGs than symmetrical voltage sags and swells. Upon further investigation, it is found that asymmetrical sags are more harmful to Type 3 WGs than asymmetrical swells. A similar comparative study is performed for Type 4 WGs. It is observed that symmetrical voltage sags and swells lead to more damage in Type 4 WGs than asymmetrical voltage sags and swells. When a comparison is done between the damaging effects of symmetrical voltage sags and swells, it is found that symmetrical sags pose a higher risk of damage to Type 4 WGs.

A novel integrated ride-through scheme is designed for Type 3 WGs to maintain normal operation by countering the adverse impact of voltage sags and swells. The scheme comprises two parts, namely a protection system and a reactive power management system. The protection system limits damaging overcurrents in the RSC and keeps the dc-link voltage within a tolerable range during grid voltage fluctuations. Whereas, the reactive power management scheme regulates the flow of reactive power between the grid and the GSC depending on the type of voltage fluctuation. The novel scheme successfully maintains normal operation of Type 3 WG during symmetrical and asymmetrical sags, and symmetrical and asymmetrical swells. Grid voltage stabilization is also performed during these events which further improves grid reliability. This scheme enhances Type 3 WG performance during grid disturbance significantly.

A novel coordinated ride-through strategy is presented for Type 4 WGs to augment their operation during grid voltage fluctuations. This strategy also consists of two parts: a safety scheme and a reactive power regulation scheme. The safety scheme prevents damaging overvoltages in the dc-link capacitor during symmetrical and asymmetrical sags and swells at PCC. Moreover, the reactive power regulation scheme controls the supply or absorption of reactive power to and from the grid depending on the type of grid voltage fluctuation. Efficient operation of Type 4 WG is ensured by the coordinated ride-through strategy and grid voltage is also stabilized. This strategy augments Type 4 WG performance during grid disturbance considerably.

7.2. Future work

The probable future works to further enhance this research are given below:

- Post-sag and post-swell performance should be analysed further and incorporated into the ride-through schemes of both Type 3 and Type 4 WGs. In this research, the performance of the wind generators during the sag or swell event has been studied. However, the wind generator performance when the sag/swell event has subsided should also be monitored to ensure more efficient wind farm operation.
- Both the ride-through schemes involve switching in and out of hardware components. The switching has been considered to be instantaneous in this research. Nevertheless, it would of interest to study the effect(s), if any, of switching on the overall performance of the wind generator operation.

Appendix A

A.1 Type 3 wind farm parameters

Parameter	Symbol	Value	Unit
Turbine Data			
No. of turbines		6	
Nominal mechanical power	P_{mech}	1.5	MW
Turbine inertia constant	H_t	4.32	
Shaft spring constant	K_s	1.11	
Shaft mutual damping	D_m	1.5	
Initial speed	$v_{initial}$	1.2	pu
Initial output torque	$T_{initial}$	0.83	pu
Generator Data			
Nominal electrical power	P_{elec}	1.5/0.9	MW
Stator voltage	$V_{s,l-l}$	575	V
Rotor voltage	$V_{r,l-l}$	1975	V
Frequency	f	50	Hz
Stator resistance	R_s	0.023	pu
Stator leakage inductance	L_{ls}	0.18	pu
Rotor resistance	R_r	0.016	pu
Rotor leakage inductance	L_{lr}	0.16	pu
Magnetizing inductance	L_m	2.9	pu
Generator inertia constant	H_g	0.685	
Friction factor	F	0.01	
Pairs of poles	p	3	
Converter Data			
GSC max. current		0.8	pu
GSC coupling inductor	L_{gsc}	0.3	pu
GSC coupling	R_{gsc}	0.003	pu

resistor			
DC-link nominal voltage	$V_{dc,nom}$	1150	V
DC-link capacitance	C	10000	μF
GSC PWM frequency		2700	Hz
RSC PWM frequency		1620	Hz
Controller Data			
DC voltage controller constants	K_p	8	
	K_i	400	
GSC current controller constants	K_p	0.83	
	K_i	5	
Speed controller constants	K_p	3	
	K_i	0.6	
RSC current controller constants	K_p	0.6	
	K_i	8	
Pitch controller constant	K_p	150	
Pitch compensation constants	K_i	3	
	K_p	30	
Reactive power controller constant	K_{i1}	0.05	
	K_{i2}	20	
Pitch rate change (maximum)	$\frac{d\beta}{dt}$	10	deg/s
Servo time constant	T_d	0.01	s

A.2 Type 4 wind farm parameters

Parameters	Symbol	Value	Unit
Turbine Data			
No. of turbines		5	
Nominal mechanical power	P_{mech}	2	MW
Turbine inertia constant	H_t	4.32	
Shaft spring constant	K_s	0.3	
Shaft mutual damping	D_m	1.5	
Initial speed	$v_{initial}$	1	pu
Initial output torque	$T_{initial}$	1	pu
Generator Data			
Nominal electrical power	P_{elec}	2/0.9	
Stator voltage	V_s	730	V
Frequency	f	50	Hz
Stator resistance	R_s	0.006	pu
Generator inertia constant	H_g	0.62	
Friction factor	F	0.01	
Pairs of poles	p	1	
Converter Data			
GSC nominal voltage		575	V
GSC max. current		1.1	pu
GSC coupling inductor	L_{gsc}	0.15	pu
GSC coupling resistor	R_{gsc}	0.15/50	pu
DC-link nominal voltage	V_{dc}	1100	V
DC-link capacitance	C	90000	μF
Boost converter inductance	L_{boost}	0.0012	pu
Boost converter resistance	R_{boost}	0.005	Ω
Controller Data			

DC voltage controller constants	K_p	1.1	
	K_i	27.5	
GSC reactive power controller constant	K_i	0.05	
GSC voltage regulator constant	K_i	2	
GSC current controller constants	K_p	1	
	K_i	50	
Speed controller constants	K_p	5	
	K_i	1	
Boost inductor current controller constants	K_p	0.025	
	K_i	100	
Pitch controller constant	K_p	15	
Pitch compensation constants	K_p	1.5	
	K_i	6	
Field excitation constants	K_p	10	
	K_i	20	
Pitch angle maximum		27	deg
Maximum pitch angle change	$\frac{d\beta}{dt}$	10	deg/s
Servo time delay	T_d	0.01	s

References

[1] P. Beiter and T. Tian, “2015 Renewable Energy Data Book,” U.S. Department of Energy, 2015.

[2] “WWEA Half-year Report 2016,” The World Wind Energy Association, Bonn, Germany, 2016.

[3] P. S. Georgilakis, “Technical challenges associated with the integration of wind power into power systems,” *Renew. & Sustain. Energy Reviews.,* vol. 12, no. 3, pp. 852-863, Apr. 2008.

[4] M.Tsili and S. Papathanassiou, "A review of grid code technical requirements for wind farms," *IET Renewable Power Generation*, vol. 3, pp. 308-332, 2009.

[5] *Grid Code High and extra high voltage,* E.ON Netz GmbH, Apr. 2006.

[6] H. T. Mokui, M. A. S. Masoum and M. Mohseni, “Review on Australian Grid Codes for Wind Power Integration in Comparison with International Standards,” *in Australasian Universities Power Engineering Conference*., Perth, AU, 2014, pp. 1-6.

[7] *Technical Rules,* Western Power, AU, Dec. 2011.

[8] T. Ackermann, “Generators and Power Electronics for Wind Turbines,” in *Wind Power in Power Systems,* 1st ed. West Sussex, England: John Wiley & Sons, 2005, ch. 4, sec. 4, pp. 53–57.

[9] J. Morren and S. W. H. de Haan, “Ridethrough of Wide Turbines with Doubly-Fed Induction Generator During a Voltage Dip,” *IEEE Trans. Energy Convers.*, vol. 20, no. 2, pp. 435-441, Jun. 2005.

[10] O. G. Bellmunt, A. J. Ferre, A. Sumper and J. B. Jane, “Ride-Through Control of a Doubly Fed Induction Generator Under Unbalanced Voltage Sags,” *IEEE Trans. Energy Convers.*, vol. 23, no. 2, pp. 1036-1045, Dec. 2008.

[11] D. C. Gaona, E. L. M. Goytia and O. A. Lara, “ Fault Ride-Through Improvement of DFIG-WT by Integrating a Two-Degrees-of-Freedom Internal Model Control,” *IEEE Trans. Ind. Electron.,* vol. 60, no. 3, Mar. 2013.

[12] J. Hu and Y. He, "Reinforced Control and Operation of DFIG-Based Wind-Power-Generation System Under Unbalanced Grid Voltage Conditions," *IEEE Trans. Energy Convers.,* vol. 24, no. 4, pp. 905-915, Dec. 2009.

[13] M. Mohseni, S. Islam and M. A. S. Masoum, "Fault ride-through capability enhancement of doubly-fed induction wind generators," *IET Renew. Power Gener.,* vol. 5, no. 5, pp. 368-376, Aug. 2010.

[14] M. Mohseni and S. M. Islam, "Transient Control of DFIG-Based Wind Power Plants in Compliance With the Australian Grid Code," *IEEE Trans. Power Electron.,* vol. 27, no. 6, pp. 2813-2824, Jun. 2012.

[15] J. P. da Costa, H. Pinheiro, T. Degner and G. Arnold, "Robust Controller for DFIGs of Grid-Connected Wind Turbines," *IEEE Trans. Ind. Electron.,* vol. 58, no. 9, pp. 4023-4038, Sept. 2011.

[16] M. J. Hossain, T. K. Saha, N. Mithulananthan and H. R. Pota, "Control Strategies for Augmenting LVRT Capability of DFIGs in Interconnected Power Systems," *IEEE Trans. Ind. Electron.,* vol. 60, no. 6, pp. 2510-2522, Jun. 2013.

[17] J. Liang, D. F. Howard, J. A. Restrepo and R. G. Harley, "Feedforward Transient Compensation Control for DFIG Wind Turbines During Both Balanced and Unbalanced Grid Disturbances," *IEEE Trans. Ind. Appl.,* vol. 49, no. 3, pp. 1452-1463, May/Jun. 2013.

[18] G. Mokryani, P. Siano, A. Piccolo and Z. Chen, "Improving Fault Ride-Through Capability of Variable Speed Wind Turbines in Distribution Networks," *IEEE Syst. J.,* vol. 7, no. 4, pp. 713-722, Dec. 2013.

[19] T. D. Vrionis, X. I. Koutiva and N. A. Vovos, "A Genetic Algorithm-Based Low Voltage Ride-Through Control Strategy for Grid Connected Doubly Fed Induction Wind Generators," *IEEE Trans. Power Syst.,* vol. 29, no. 3, pp. 1325-1334, May 2014.

[20] X. Liu and X. Kong, "Nonlinear Model Predictive Control for DFIG-Based Wind Power Generation," *IEEE Trans. Autom. Sci. Eng.,* vol. 11, no. 4, pp. 1046-1055, Oct. 2014.

[21] V. F. Mendes, C. V. de Sousa, W. Hofmann and S. R. Silva, "Doubly-fed induction generator ride-through fault capability using resonant controllers for asymmetrical voltage sags," *IET Renew. Power Gener.,* vol. 9, no. 7, pp. 783-791, Mar. 2015.

[22] H. Nian, P. Cheng and Z. Q. Zhu, "Independent Operation of DFIG-Based WECS Using Resonant Feedback Compensators Under Unbalanced Grid Voltage Conditions," *IEEE Trans. Power Electron.,*vol. 30, no. 7, pp. 3650-3661, Jul. 2015.

[23] M. A. Chowdhury, A. H. M. Sayem, W. Shen and K. S. Islam, "Robust active disturbance rejection controller design to improve low-voltage ride-through capability of doubly fed induction generator wind farms," *IET Renew. Power Gener.,* vol. 9, no. 8, pp. 961-969, May 2015.

[24] P. Cheng and H. Nian, "Collaborative Control of DFIG System During Network Unbalance Using Reduced-Order Generalized Integrators," *IEEE Trans. Energy Convers.,*vol. 30, no. 2, pp. 453-464, Jun. 2015.

[25] L. Xu and Y. Wang, "Dynamic Modeling and Control of DFIG-Based Wind Turbines Under Unbalanced Network Conditions," *IEEE Trans. Power Syst.,* vol. 22, no. 1, pp. 314-323, Feb. 2007.

[26] L. Xu, "Coordinated Control of DFIG's Rotor and Grid Side Converters During Network Unbalance," *IEEE Trans. Power Electron.,* vol. 23, no. 3, pp. 1041-1049, May 2008.

[27] Y. Zhou, P. Bauer, J. A. Ferreira and J. Pierik, "Operation of Grid-Connected DFIG Under Unbalanced Grid Voltage Condition, *IEEE Trans. Energy Convers.,* vol. 24, no. 1, pp. 240-246, Mar. 2009.

[28] F. K. A. Lima, A. Luna, P. Rodriguez, E. H. Watanabe and F. Blaabjerg, "Rotor Voltage Dynamics in the Doubly Fed Induction Generator During Grid Faults," *IEEE Trans. Power Electron.,* vol. 25, no. 1, pp. 118-130, Jan. 2010.

[29] H. Geng, C. Liu and G. Yang, "LVRT Capability of DFIG-Based WECS Under Asymmetrical Grid Fault Condition," *IEEE Trans. Ind. Electron.,* vol. 60, no. 6, pp. 2495-2509, Jun. 2013.

[30] S. F. Chou, C. T. Lee, H. C. Ko and P. T. Cheng, “A Low-Voltage Ride-Through Method With Transformer Flux Compensation Capability of Renewable Power Grid-Side Converters,” *IEEE Trans. Power Electron.,* vol. 29, no. 4, pp. 1710-1719, Apr. 2014.

[31] M. A. A. Rani, C. Nagamani, G. S. Ilango and A. Karthikeyan, “An Effective Reference Generation Scheme for DFIG With Unbalanced Grid Voltage,” *IEEE Trans. Sustain. Energy.,* vol. 5, no. 3, pp. 1010-1018, Jul. 2014.

[32] D. Xiang, L. Ran, P. J. Tavner and S. Yang “Control of a Doubly Fed Induction Generator in a Wind Turbine During Grid Fault Ride-Through,” *IEEE Trans. Energy Convers.,* vol. 21, no. 3, pp. 652-662, Sept. 2006.

[33] S. Xiao, G. Yang, H. Zhou and H. Geng, “An LVRT Control Strategy Based on Flux Linkage Tracking for DFIG-Based WECs,” *IEEE Trans. Ind. Electron.,* vol. 60, no. 7, pp. 2820-2832, Jul. 2013.

[34] R. Zhu, Z. Chen, X. Wu and F. Deng, “Virtual Damping Flux-Based LVRT Control for DFIG-Based Wind Turbine,” *IEEE Trans. Energy Convers.,* vol. 30, no. 2, pp. 714-725, Jun. 2015.

[35] W. Chen, D. Xu, N. Zhu, M. Chen and F. Blaabjerg, “Control of Doubly-Fed Induction Generator to Ride-Through Recurring Grid Faults,” *IEEE Trans. Power Electron.,* vol. 31, no. 7, pp. 4831-4845, July. 2016.

[36] J. Lopez, E. Gubia, E. Olea, J. Ruiz and L. Marroyo, “Ride Through of Wind Turbines With Doubly Fed Induction Generator Under Symmetrical Voltage Dips,” *IEEE Trans. Ind. Electron.,* vol. 56, no. 10, pp. 4246-4254, Oct. 2009.

[37] S. Hu, X. Lin, Y. Kang and X. Zou, “An Improved Low-Voltage Ride-Through Control Strategy of Doubly Fed Induction Generator During Grid Faults,” *IEEE Trans. Power Electron.,* vol. 26, no. 12, pp. 3653-3665, Dec. 2011.

[38] V. F. Mendes, C. V. Suosa, S. R. Silva, B. C. Rabelo and W. Hofmann, “Modeling and Ride-Through Control of Doubly Fed Induction Generators During Symmetrical Voltage Sags,” *IEEE Trans. Energy Convers.,* vol. 26, no. 4, pp. 1161-1171, Dec. 2011.

[39] L. Zhou, J. Liu and S. Zhou, “Improved Demagnetization Control of a Doubly Fed Induction Generator Under Balanced Grid Fault,” *IEEE Trans. Power Electron.,* vol. 30, no. 12, pp. 6695-6705, Dec. 2015.

[40] J. Liang, W. Qiao and R. G. Harley, “Feed-Forward Transient Current Control for Low-Voltage Ride-Through Enhancement of DFIG Wind Turbines,” *IEEE Trans. Energy Convers.,* vol. 25, no. 3, pp. 836-843, Sept. 2010.

[41] L. Yang, Z. Xu, J. Ostergaard, Z. Y. Dong and K. P. Wong, “Advanced Control Strategy of DFIG Wind Turbines for Power System Fault Ride Through,” *IEEE Trans. Power Syst.,* vol. 27, no. 2, pp. 713-722, May 2012.

[42] D. Xie, Z. Xu, L. Yang, Y. Xue and K. P. Wong, “A Comprehensive LVRT Control Strategy for DFIG Wind Turbines With Enhanced Reactive Power Support,” *IEEE Trans. Power Syst.,* vol. 28, no. 3, pp. 3302-3310, Aug. 2013.

[43] F. Wei, D. M. Vilathgamuwa and C. S. Shing, “Design of mode switching scheme for low-voltage ride-through of doubly fed induction generators,” *IET Renew. Power Gener.,* vol. 9, Iss. 2, pp. 109-119, Jun. 2015.

[44] S. Liu, T. Bi, K. Jia and Q. Yang, “Coordinated fault-ride-through strategy for doubly-fed induction generators with enhanced reactive and active power support,” *IET Renew. Power Gener.,* vol. 10, no. 2, pp. 203-211, Aug 2015.

[45] Q. Huang, X. Zou, D. Zhu and Y. Kang, “Scaled Current Tracking Control for Doubly Fed Induction Generator to Ride-Through Serious Grid Faults,” *IEEE Trans. Power Electron.,* vol. 31, no. 3, pp. 2150-2165, Jun. 2016.

[46] Y. M. Alsmadi, L. Xu, F. Blaabjerg, A. J. P. Ortega, A. Y. Abdelaziz, A. Wang and Z. Albataineh, “Detailed Investigation and Performance Improvement of the Dynamic Behavior of Grid-Connected DFIG- Based Wind Turbines Under LVRT Conditions,” *IEEE Trans. Ind. Appl.,* vol. 54, no. 5, pp. 4795-4812, Sept./Oct. 2018.

[47] J. Yang, J. E. Fletcher and J. O’Reily, “A Series-Dynamic-Resistor-Based Converter Protection Scheme for Doubly-Fed Induction Generator During Various Fault Conditions,” *IEEE Trans. Energy Convers.,* vol. 25, no. 2, pp. 422-432, Jun. 2010.

[48] K. E. Okedu, S. M. Muyeen, R. Takahashi and J. Tamura, "Wind Farms Fault Ride Through Using DFIG With New Protection Scheme," *IEEE Trans. Sustain. Energy.,* vol. 3, no. 2, pp. 242-254, Apr. 2012.

[49] P. H. Huang, M. S. E. Moursi and S. A. Hasen, "Novel Fault Ride-Through Scheme and Control Strategy for Doubly Fed Induction Generator-Based Wind Turbine," *IEEE Trans. Energy Convers.,* vol. 30, no. 2, pp. 635-645, Jun. 2015.

[50] L. Huchel, M. S. E. Moursi and H. H. Zeineldin, "A Parallel Capacitor Control Strategy for Enhanced FRT Capability of DFIG," *IEEE Trans. Sustain. Energy.,* vol. 6, no. 2, pp. 303-312, Apr. 2015.

[51] H. Mohammapour, S. G. Zadeh and S. Tohidi, "Symmetrical and asymmetrical low-voltage ride through of doubly-fed induction generator wind turbines using gate controlled series capacitor," *IET Renew. Power Gener.,* vol. 9, no. 7, pp. 840-846, Apr. 2015.

[52] B. B. Ambati, P. Kanjiya and Vinod Khadkikar, "A Low Component Count Series Voltage Compensation Scheme for DFIG WTs to Enhance Fault Ride-Through Capability," *IEEE Trans. Energy Convers.,* vol. 30, no. 1, pp. 208-217, Mar. 2015.

[53] K. E. Okedu, "Enhancing DFIG wind turbine during three-phase fault using parallel interleaved converters and dynamic resistor," *IET Renew. Power Gener.,* vol. 10, no. 8, pp. 1211-1219, Apr. 2016.

[54] W. Guo, L. Xiao, S. Dai, X. Xu, Y. Li and Y. Wang, "Evaluation of the Performance of BTFCLs for Enhancing LVRT Capability of DFIG," *IEEE Trans. Power Electron.,* vol. 30, no. 7, pp. 3623-3637, Jul. 2015.

[55] W. Guo, L. Xiao, S. Dai, Y. Li, X. Xu, W, Zhou and L. Li, "LVRT Capability Enhancement of DFIG With Switch-Type Fault Current Limiter," *IEEE Trans. Ind. Electron.,* vol. 62, no. 1, pp. 332-342, Jan. 2015.

[56] Z. C. Zou, X. Y. Xiao, Y. F. Liu, Y. Zhang and Y. H. Wang, "Integrated Protection of DFIG-Based Wind Turbine With a Resistive-Type SFCL Under Symmetrical and Asymmetrical Faults," *IEEE Trans. Appl. Supercond.,* vol. 26, no. 7, Oct. 2016.

[57] T. Karaipoom and I. Ngamroo, "Optimal Superconducting Coil Integrated Into DFIG Wind Turbine for Fault Ride Through Capability Enhancement and Output Power Fluctuation Suppression," *IEEE Trans. Sustain. Energy,* vol. 6, no. 1, pp. 28-42, Jan. 2015.

[58] J. Mohammadi, S. Afsharnia, S. V. Zadeh and S. Farhangi, "Improved fault ride through strategy for doubly fed induction generator based wind turbines under both symmetrical and asymmetrical grid faults," *IET Renew. Power Gener.,* vol. 10, no. 8, pp. 1114-1122, Mar. 2016.

[59] Y. W. Shen, D. P. Ke, W. Qiao, Y. Z. Sun, D. S. Kirschen and C. Wei, "Transient Reconfiguration and Coordinated Control for Power Converters to Enhance the LVRT of a DFIG Wind Turbine With an Energy Storage Device," *IEEE Trans. Energy Convers.,* vol. 30, no. 4, pp. 1679-1690, Dec. 2015.

[60] A. Jalilian, S. B. Naderi, M. Negnevitsky, M. T. Hagh and K. M. Muttaqi, "Controllable DC-link fault current limiter augmentation with DC chopper to improve fault ride-through of DFIG," *IET Renew. Power Gener.,* vol. 11, no. 2, pp. 313-324, Jan. 2017.

[61] W. Uddin, K. Zeb, A. Tanoli and A. Haider, "Hardware-based hybrid scheme to improve the fault ride through capability of doubly fed induction generator under symmetrical and asymmetrical fault," *IET Gener. Transm. Distrib..,* vol. 12, no. 1, pp. 200-206, Oct. 2017.

[62] S. E. da Silveria, S. M. Silva and B. J. C. Filho, "Fault ride-through enhancement in DFIG with control of stator flux using minimised series voltage compensator," *IET Renew. Power Gener.,* vol. 12, no. 11, pp. 1234-1240, Jul. 2018.

[63] X. Y. Xiao, R. H. Yang, X. Y. Chen and Z. X. Zheng, "Integrated DFIG Protection With a Modified SMES- FCL Under Symmetrical and Asymmetrical Faults," *IEEE Trans. Appl. Supercond.,* vol. 28, no. 4, Jun. 2018.

[64] M. Firouzi and G. Gharehpetian, "LVRT Performance Enhancement of DFIG-Based Wind Farms by Capacitive Bridge-Type Fault Current Limiter," *IEEE Trans. Sustainable Enery.,* vol. 9, no. 3, pp. 1118-1125, Jul. 2018.

[65] Z. Xie, X. Zhang, S. Yang and L. Wang, “Improved Ride-Through Control of DFIG During Grid Voltage Swell,” *IEEE Trans Ind. Electron.,* vol. 62, no. 6, pp. 3584-3594, Jun. 2015.

[66] D. S. Martin, J. L. R. Amenedo and S. Arnaltes, “Providing Ride-Through Capability to a Doubly Fed Induction Generator Under Unbalanced Voltage Dips,” *IEEE Trans Power Electron.,* vol. 24, no. 7, pp. 1747-1757, Jul. 2009.

[67] A. Mullane, G. Lightbody and R. Yacamini, “Wind-Turbine Fault Ride-Through Enhancement,” *IEEE Trans Power Syst.,* vol. 20, no. 4, pp. 1929-1937, Jul. 2009.

[68] J. Matas, M. Castilla, J. M. Guerrero, L. G. Vicuna and J. Miret, “Feedback Linearization of Direct-Drive Synchronous Wind-Turbines Via a Sliding Mode Approach,” *IEEE Trans Power Electron.,* vol. 23, no. 3, pp. 1093-1103, May 2008.

[69] K. H. Kim, Y. C. Jeung, D. C. Lee and H. G. Kim, “LVRT Scheme of PMSG Wind Power Systems Based on Feedback Linearization,” *IEEE Trans Power Electron.,* vol. 27, no. 5, pp. 2376-2384, May 2012.

[70] F. Valenciaga and R. D. Fernandez, “Multiple-input-multiple-output high-order sliding mode control for a permanent magnet synchronous generator wind-based system with grid support capabilities,” *IET Renew. Power Gener.,* vol. 9, no. 8, pp. 925-934, Apr. 2015.

[71] S. Alepuz, S. B. Monge, J. Bordanau, J. A. M. Velasco, C. A. Silva, J. Pontt and J. Rodriguez, “Control Strategies Based on Symmetrical Components for Grid-Connected Converters Under Voltage Dips,” *IEEE Trans. Ind. Electron.,* vol. 56, no. 6, pp. 2162-2173, Jun. 2009.

[72] H. M. Yassin, H. H. Hanafy and M. M. Hallouda, “Enhancement low-voltage ride through capability of permanent magnet synchronous generator-based wind turbines using interval type-2 fuzzy control,” *IET Renew. Power Gener.,* vol. 10, no. 3, pp. 339-348, Sept. 2015.

[73] M. S. Khan and M. R. Iravani, “Hybrid Control of a Grid-Interactive Wind Energy Conversion System,” *IEEE Trans. Energy Convers.,* vol. 23, no. 3, pp. 895-902, Sept. 2008.

[74] H. M. Hasanien and S. M. Muyeen, “Design Optimization of Controller Parameters Used in Variable Speed Wind Energy Conversion System by Genetic Algorithms,” *IEEE Trans. Sustain. Energy,* vol. 3, no. 2, pp. 200-208, Apr. 2012.

[75] J. Chen, L. Jiang, W. Yao and Q. H. Wu, “Perturbation Estimation Based Nonlinear Adaptive Control of a Full-Rated Converter Wind Turbine for Fault Ride-Through Capability Enhancement,” *IEEE Trans. Power Syst.,* vol. 29, no. 6, pp. 2733-2743, Nov. 2014.

[76] H. N. V. Pico and D. C. Aliprantis, “Voltage Ride-Through Capability Verification of Wind Turbines With Fully-Rated Converters Using Reachability Analysis,” *IEEE Trans. Power Convers.,* vol. 29, no. 2, pp. 392-405, Jun. 2014.

[77] A. C. Prado, S. Alepuz, J. Bordonau, P. Cortes and J. Rodriguez, “Predictive Control of a Back-to-Back NPC Converter-Based Wind Power System,” *IEEE Trans. Ind. Electron.,* vol. 63, no. 7, pp. 4615-4627, Jul. 2016.

[78] V. Yaramasu, B. Wu, S. Alepuz and S. Kouro, “Predictive Control for Low-Voltage Ride-Through Enhancement of Three-Level-Boost and NPC-Converter-Based PMSG Wind Turbine,” *IEEE Trans. Ind. Electron.,* vol. 61, no. 12, pp. 6832-6843, Dec. 2014.

[79] M. H. Qais, H. M. Hasanien and S. Alghuwainem, “A Grey Wolf Optimizer for Optimum Parameters of Multiple PI Controllers of a Grid- Connected PMSG Driven by Variable Speed Wind Turbine,” *IEEE Access.,* vol. 6, pp. 44120-44128, Aug. 2018.

[80] M. F. M. Arani and Y. A. R. I. Mohamed, “Assessment and Enhancement of a Full-Scale PMSG-Based Wind Power Generator Performance Under Faults,” *IEEE Trans. Energy Convers.,* vol. 31, no. 2, pp. 728-739, Jun. 2016.

[81] A. D. Hansen and G. Michalke, “Multi-pole permanent magnet synchronous generator wind turbines’ grid support capability in uninterrupted operation during grid faults,” *IET Renew. Power Gener.,* vol. 3, no. 3, pp. 333-348, Nov. 2008.

[82] J. Dai, D. Xu, B. Wu and N. R. Zargari, "Unified DC-Link Current Control for Low-Voltage Ride-Through in Current-Source-Converter-Based Wind Energy Conversion Systems," *IEEE Trans. Power Electron.,* vol. 26, no. 1, pp. 288-297, Jan. 2011.

[83] H. Geng, G. Yang, D. Xu and B. Wu, "Unified Power Control for PMSG-Based WECS," *IEEE Trans. Energy Convers.,* vol. 26, no. 3, pp. 822-830, Sept. 2011.

[84] S. Alepuz, A. Calle, S. B. Monge, S. Kouro and B. Wu, "Use of Stored Energy in PMSG Rotor Inertia for Low-Voltage Ride-Through in Back-to-Back NPC Converter-Based Wind Power Systems," *IEEE Trans. Ind. Electron.,* vol. 60, no. 5, pp. 1787-1796, May 2013.

[85] T. Neumann, T. Wijnhoven, G. Deconinck and I. Erlich, "Enhanced Dynamic Voltage Control of Type 4 Wind Turbines During Unbalanced Grid Faults," *IEEE Trans. Energy Convers.,* vol. 30, no. 4, pp. 1650-1659, Dec. 2015.

[86] S. M. Muyeen, R. Takahashi, T. Murata and J. Tamura, "A Variable Speed Wind Turbine Control Strategy to Meet Wind Farm Grid Code Requirements," *IEEE Trans. Power Syst.,* vol. 25, no. 1, pp. 331-340, Feb. 2010.

[87] G. Saccomando, J. Svensson and A. Sannino, "Improving Voltage Disturbance Rejection for Variable-Speed Wind Turbines," *IEEE Trans. Energy Convers.,* vol. 17, no. 3, pp. 422-428, Sept. 2002.

[88] G. Ramtharan, A. Arulampalam, J. B. Ekanayake, F. M. Hughes and N. Jenkins, "Fault ride through of fully rated converter wind turbines with AC and DC transmission systems," *IET Renew. Power Gener.,* vol. 3, no. 4, pp. 426-438, Jul. 2008.

[89] C. H. Ng, L. Ran and J. Bumby, "Unbalanced-Grid-Fault Ride-Through Control for a Wind Turbine Inverter," *IEEE Trans. Ind. Appl.,* vol. 44, no. 3, pp. 845-856, Jun. 2008.

[90] M. Nasiri and R. Mohammadi, "Peak Current Limitation for Grid Side Inverter by Limited Active Power in PMSG-Based Wind Turbines During Different Grid Faults," *IEEE Trans. Sustain. Energy,* vol. 8, no. 1, pp. 3-12, Jan. 2017.

[91] A. Moawwad, M. S. E. Moursi and W. Xiao, “A Novel Transient Control Strategy for VSC-HVDC Connecting Offshore Wind Power Plant,” *IEEE Trans. Sustain. Energy,* vol. 5, no. 4, pp. 1056-1069, Oct. 2014.

[92] P. Xing, L. Fu, G. Wang, Y. Wang and Y. Zhang, “A compositive control method of low-voltage ride through for PMSG-based wind turbine generator system,” *IEEE Gener. Transm. Distrib. Energy*, vol. 12, no. 1, pp. 117-125, Oct. 2017.

[93] R. Vijayapriya and M. P. Selvan, “A Modified Active Power Control Scheme for Enhanced Operation of PMSG-Based WGs,” *IEEE Trans. Sustainable Enery*, vol. 9, no. 2, pp. 630-638, Apr. 2018.

[94] M. Nasri and R. Mohammadi, “Peak Current Limitation for Grid Side Inverter by Limited Active Power in PMSG-Based Wind Turbines During Different Grid Faults,” *IEEE Trans. Sustainable Enery*, vol. 8, no. 1, pp. 3-12, Jan. 2017.

[95] T. H. Nguyen and D. C. Lee, “Advanced Fault Ride-Through Technique for PMSG Wind Turbine Systems Using Line-Side Converter as STATCOM,” *IEEE Trans. Ind. Electron., IEEE Trans. Ind. Electron.,* vol. 60, no. 7, pp. 2842-2850, Jul. 2013.

[96] J. F. Conroy and R. Watson, “Low-voltage ride-through of a full converter wind turbine with permanent magnet generator,” *IET Renew. Power Gener.,* vol. 60, no. 7, pp. 2842-2850, Jul. 2013.

[97] V. Akhmatov, “Modelling and Ride-through Capability of Variable Speed Wind Turbines with Permanent Magnet Generators,” *Wind Energy.,* vol. 9, pp. 313-326, Nov. 2005.

[98] M. Popat, B. Wu and N. R. Zargari, “Fault Ride-Through Capability of Cascaded Current-Source Converter-Based Offshore Wind Farm,” *IEEE Trans. Sustain. Energy.,* vol. 4, no. 4, pp. 314-323, Apr. 2013.

[99] L. Chen, H. He, H. Chen, L. Wang, L. Zhu, Z. Shu, F. Tang and J. Yang, “Study of a Modified Flux-Coupling-Type SFCL for Efficient Fault Ride-Through in a PMSG Wind Turbine Under Different Types of Faults,” *Canadian Journal Electr. Comp. Eng.,* vol. 40, no. 3, pp. 189-200, Sept. 2017.

[100] D. M. Yehia, D. E. A. Mansour and W. Yuan, "Fault Ride-Through Enhancement of PMSG Wind Turbines With DC Microgrids Using Resistive-Type SFCL," *IEEE Trans. Appl. Supercond.,* vol. 28, no. 4, Jun. 2018.

[101] A. Perdana, "Dynamic Models of Wind Turbines," Ph.D. dissertation, Dept. Of Energy and Environ., Chalmers Univ. of Tech. Goteborg, Sweden, 2008.

[102] M. A. Chowdhury, "Impact of Wind Energy Systems on Power System Dynamics and Stability," Ph.D. dissertation, Dept. of Engg. and Tech., Swinburne Univ. of Tech., Victoria, Australia, 2013.

[103] R. J. Lee, P. Pillay and R. G. Harley, "D, Q Reference Frames for the simulation of Induction Motors ," *Electric Power Systems Research.,*. vol. 8, no. 1, pp. 15-26, Oct. 1984.

[104] T. Ackermann, "Generators and Power Electronics for Wind Turbines," in *Wind Power in Power Systems,* 1st ed. West Sussex, England: John Wiley & Sons, 2005, ch. 4, sec. 4, pp. 60–61.

[105] I. S. Wander, "Modeling of Synchronous Generator and Full-Scale Converter for Distribution System Load Flow Analysis," M.S. thesis, Dept. of Electrical and Computer Engg., Ryerson University., Toronto, Ontario, Canada, 2011.

[106] E. Tramblay, S. Ayayde and A. Chandra, "Comparative Study of Control Strategies for the Doubly Fed Induction Generator in Wind Energy Conversion Systems: A DSP-Based Implementation Approach," *IEEE Trans. Sustain. Energy*, vol. 2, no. 3, pp. 288-299, Jul. 2011.

[107] E. Valsera-Naranjo, A. Sumper and O. Gomis-Bellmunt, "Pitch control system design to improve frequency response capability of fixed-speed wind turbine systems," *International Trans. Electric. Energy Syst.*, vol. 21, no. 7, pp. 1984-2006, Oct. 2011.

[108] B. R. Karthikeya and R. J. Schutt, "Overview of Wind Park Control Strategies,", *IEEE Trans. Sustain. Energy,* vol. 5, no. 2, pp. 416-422, Apr. 2014.

[109] J. Niiranen, "Voltage dip ride-through of a doubly fed generator equipped with an active crowbar," Nordic Wind Power Conference, Gothenburg, Sweden, Mar. 2004.

[110] J. Morren and S. de Haan, “Short-circuit current of wind turbines with doubly fed induction generator,” *IEEE Trans. Energy Converse,* vol. 22, no. 1, pp. 174 – 180, Mar. 2007.

[111] J. Lopez, E. Gubia, P. Sanchis, X. Roboam and L. Marroyo, “Dynamic Behavior of Doubly Fed Induction Generator During Three-Phase Voltage Dips,” *IEEE Trans. Energy Convers.,* vol. 22, no. 3, pp. 709-717, Sept. 2007.

[112] J. Lopez, E. Gubia, P. Sanchis, X. Roboam and L. Marroyo, “Wind Turbines Based on Doubly Fed Induction Generator Under Asymmetrical Voltage Dips,” *IEEE Trans. Energy Convers.,* vol. 23, no. 1, pp. 321-330, Mar. 2008.

[113] X. Zhang, T. Qu, Z. Xie and R. Cao, “Dynamic analysis of doubly fed induction generator during symmetrical voltage swells,” *2011 Second International Conference on Mechanic Automation and Control Engineering (MACE)*, Hohhot, China, 2011, pp. 1245-1248.

[114] A. Petersson, “Analysis, Modeling and Control of Doubly-Fed Induction Generators for Wind Turbines,” Ph.D. dissertatiaon, Dept. Energy & Envron., Chalmers Univ.,Goteborg, Sweden, 2005.

[115] N. W. Miller, W. W. Price and J. J, Sanchez-Gasca, “Dynamic Modeling of GE 1.5 and 3.6 Wind Turbine-Generators,”,3rd ed., GE Co., New York, USA, 2003, pp. 1.1-7.1.

[116] H. Demuth and M. Beale (2004). *Neural Network Toolbox* [online]. Available: https://au.mathworks.com/help/nnet/